



Max-Planck-Institut für Metallforschung
Stuttgart

Deformation and Fracture Mechanical Properties of Precursor-Derived Si-C-N Ceramics

Narayanan Janakiraman

Dissertation
an der
Universität Stuttgart

Bericht Nr. 196
Februar 2007

Deformation and Fracture Mechanical Properties of Precursor-Derived Si-C-N Ceramics

Dissertation

Von der Fakultät Chemie der Universität Stuttgart
zur Erlangung der Würde eines
Doktors der Naturwissenschaften (Dr. rer. nat)
genehmigte Abhandlung

Vorgelegt von
Narayanan Janakiraman
aus Chennai, Indien

Hauptberichter: Prof. Dr. rer. nat. Fritz Aldinger
Mitberichter: Prof. Dr. rer.nat. Dietrich Munz
Prüfungsvorsitzender: Prof. Dr. Ir. Eric J. Mittemeijer

Tag der mündlichen Prüfung: 28. Februar 2007

Institut für Nichtmetallische Anorganische Materialien der Universität Stuttgart
Max-Planck Institut für Metallforschung, Stuttgart
Pulvermetallurgisches Laboratorium
2007

Dedicated to

Sanjay,

Ananthalakshmi

And

Gomathi

Acknowledgements

I take this occasion to express my sincere gratitude to Prof. Dr. Fritz Aldinger for providing me this excellent opportunity to work at the Max-Planck-Institut für Metallforschung on a stimulating and challenging project. My academic and research career was primarily shaped and developed during the tenure of this Ph.D. work. In addition to his all-time support and guidance for the Ph.D. work, his fatherly attitude, motivation and encouragement meant a lot in the successful completion of this work.

Financial support for this work provided by the Max-Planck-Gesellschaft is gratefully acknowledged.

I am indebted to Prof. Dr. Dietrich Munz for accepting to act as the Mitberichter of my thesis defense. Further, he provided his valuable time and effort to read the manuscript of this thesis thoroughly and offered useful recommendations for its improvement.

I thank Prof. Dr. E. J. Mittemeijer for kindly consenting to become the chairman of my examination committee.

I would like to thank Dr. Andre Zimmermann for initiating me into this Ph.D. work and for his scientific and organizational support during the initial period of this work.

This work greatly benefited from the help in experimental work and scientific collaboration with my co-researchers and friends, Dr. Zaklina Burghard and Dr. Susan Enders. I also acknowledge their help in reading part or whole of this thesis manuscript and for providing useful suggestions.

I am grateful to Prof. Dr. Robert Danzer (Institut für Struktur- und Funktionskeramik, Montanuniversität Leoben) and Dr. Theo Fett (Institut für Materialwissenschaft, Forschungszentrum Karlsruhe) for useful discussion of my results on fracture characterization, and Dr. Elizabeth Bouchaud (Physicist - Head of the Division of Physics and Chemistry of Surfaces and Interfaces, CEA-SACLAY) for providing helpful insight on the fractal analysis of fracture.

I thankfully acknowledge scientific and personal support from many of my co-workers at MPI at various stages of this research work. Specifically, Mr. Peter Gerstel and Mr. Reinhard Mager offered important support in the precursor processing and mechanical characterization respectively. Additionally, Mr. Gerhard Kaiser, Ms. Martina Thomas, Mr. Horst Kummer, Mr. Hartmut Labitzke, Mr. Vogt (MPI-FKF), Mrs. Ulrike Täffner, Mr. Hans Eckstein, Mr. Manfred Binder, Mr. Horst Opielka and Mr. Ewald Bruckner helped with experiments, characterization and technical support. I am also thankful to Dr. Clemens Ulrich (MPI-FKF), Dr. Cai and Dr. Golczewski for carrying out key material characterization experiments for this work. My friendliest thanks are also due to Dr. Sandeep Shah (University of Colorado, Boulder), especially for pioneering the precursor casting route, but also for his advice, guidance and motivation in scientific and personal aspects with an all-time cool attitude.

Mrs. Sabine Paulsen was very helpful in the sphere of administrative matters, official formalities and personal issues, always with a friendly disposition. I deposit my heartiest thanks to her.

I thoroughly enjoyed the warm and positive working atmosphere at MPI and the friendship of colleagues from various nations and cultures. I submit my wholehearted thanks to the MPI family for this wonderful time.

Apart from the scientific career that I earned at MPI is the Love, cheers, support and togetherness of my friends at MPI and Stuttgart,...Goutam, Gokul, Lee, Kailash, Karthik, Koushik, Nachi, Nuri, Pradyot, Praveen, Ravi, Venki, Vinod, Vladimir,...it is not just what they said or did, but they were there all the time in ebb and flow. I express my special thanks to Praveen for his extreme help, support and motivation during the final stages of this work that kept me going.

Finally I deeply acknowledge the Love and support of my wife Sudha, in enduring with me all the trouble, during long and late working hours, missed sleep, care and entertainment. She also practically helped me in many computations in this work, manuscript preparation, proof reading and correction. I also acknowledge the Love and care extended by my brother Rudresh in India and for enduring my long separation away from home.

Contents

ACKNOWLEDGMENTS	1
CONTENTS	3
SYMBOLS AND ABBREVIATIONS.....	6
ABSTRACT.....	11
1. INTRODUCTION	14
2. FABRICATION AND CHARACTERIZATION OF FULLY DENSE SI-C-N CERAMICS FROM A POLY(UREAMETHYLVINYL)SILAZANE PRECURSOR.....	18
2.1. Introduction	18
2.2. Experimental procedure	20
2.3. Results	24
2.3.1. Fabrication of fully dense samples.....	24
2.3.2. Chemical and Structural characterization.....	28
2.3.2.1. Bulk chemical analysis	28
2.3.2.2. FT-IR	29
2.3.2.3. Raman spectroscopy.....	30
2.3.2.4. X-ray diffraction	31
2.3.2.5. High-resolution transmission electron microscopy	32
2.3.3. Physical and chemical characterization	34
2.4. Discussion	35
2.5. Conclusions.....	39
3. FRACTURE TOUGHNESS EVALUATION OF PRECURSOR-DERIVED SI-C-N CERAMICS USING THE CRACK OPENING DISPLACEMENT APPROACH.....	41
3.1. Introduction	41
3.2. Theoretical Background	43

3.3. Experimental procedure	45
3.4. Results	48
3.4.1. COD profiles	48
3.4.2. K_{I0} and G_{I0} estimates	50
3.4.3. Morphology of crack propagation	52
3.4.4. Material contrast imaging	54
3.5. Discussion	57
3.6. Conclusions	62
4. FRACTURE IN PRECURSOR-DERIVED SI-C-N CERAMICS – ANALYSIS OF CRACK ROUGHNESS AND DAMAGE MECHANISMS	63
4.1. Introduction	63
4.2. Theoretical Back ground	66
4.3. Materials and Methods	68
4.4. Results	69
4.5. Discussion	74
4.6. Conclusions	78
5. NANOINDENTATION ANALYSIS OF ELATIC AND PLASTIC DEFORMATION IN PRECURSOR-DERIVED SI-C-N CERAMICS	79
5.1. Introduction	79
5.2. Experimental procedure	81
5.2.1. Materials	81
5.2.2. Indentation	82
5.3. Results	83
5.3.1. Analysis of Berkovich loading curves and tip imperfection	83
5.3.2. Oliver-Pharr analysis – Berkovich indentation	84
5.3.3. Oliver-Pharr analysis – spherical indentation	87
5.3.4. Analysis of the load-unload cycle	88
5.3.5. Load / size effect on hardness	93
5.3.6. Reverse analysis of $P-h$ curves	95
5.3.7. Analysis of indentation creep deformation at constant loading	102

5.3.8. Pile-up and sink-in behavior	108
5.4. Discussion	110
5.5. Conclusions	116
6. SUMMARY AND CONCLUSIONS	118
REFERENCES	124
ZUSAMMENFASSUNG UND AUSBLICK	132

Symbols and abbreviations

A	fitting coefficient
A_c	true contact area
A_0	free-air amplitude (tapping mode AFM)
A_{sp}	set-point amplitude (tapping mode AFM)
a	crack length
a_c	contact radius
B	fitting coefficient
b	coefficient in flow equation
c_0, c_1, c_2	quadratic polynomial coefficients for fitting loading curve
D	fractal dimension
D^*	fractal dimensional increment
D_B	box dimension (Box fractal dimension)
d	half indentation diagonal
E	plane stress elastic modulus (Young's modulus)
E', E^*	plane strain elastic modulus
E_r	reduced modulus
E_i	elastic modulus of diamond indenter
f	inverse of wavelength
H	nanoindentation hardness
H_M	Meyer hardness
H_{pl}	plastic hardness
h	time in hours
\dot{h}	indenter displacement rate
h_c	true contact depth
h_0	depth parameter in Doerner-Nix relation
h_{i0}	hold-time displacement at $t = 0$
$h(a', x)$	weight function
$h(x)$	fracture profile height function

h, h_{max}	Indenter displacement, maximum indenter displacement
h_{res}	residual depth
$I(D), I(G)$	relative intensity, Raman peaks
K	Kelvin unit of temperature
K	coefficient in power law equation
K_I	mode-I stress intensity factor
K_{I0}	mode-I crack-tip fracture toughness
K_{IC}	mode-I fracture toughness
K_{Tip}	crack-tip fracture toughness
k	stress coefficient
m	strain rate sensitivity
N	number count
n	strain hardening exponent
P, P_{max}	Indentation load, maximum indentation load
P_{hold}	load during nanoindentation hold period
$p(f)$	power spectral density function
p_m	mean contact pressure
q	fitting parameter for hold time creep displacement
R_{Berk}	tip-radius of Berkovich indenter
R_{max}	Maximum amplitude of crack deflection
R_q	root mean square roughness
R_{sph}	radius of spherical indenter
r, θ	radial coordinates
r	horizontal distance between two points on the fracture profile
S	contact stiffness or unloading slope
$S(r)$	Structure function
s	Seconds
s	stress exponent
T	temperature

T_P	pyrolysis temperature
t	time
t_{hold}	hold time in nanoindentation
U	crack energy
$u_{near-tip}$	half crack opening displacement in y-direction in the near tip region
u_{total}	overall half crack opening displacement in y-direction
u_y	displacement at any point P in y-direction (mode I loading)
W_{el}, W_{pb}, W_{tot}	elastic, plastic and total work of indentation deformation, derived from nanoindentation load-unload cycle
w	specimen thickness
X	polynomial variable
X	crack interface coordinate
x, y, z	Cartesian spatial coordinates
x', y', z'	transformed coordinates
x	coordinate location along the crack where u_y is measured
x_f	Fitting exponent
x_l	nanoindentation loading curve exponent
x_{ul}	nanoindentation unloading curve exponent
z	fracture profile height
z_{max}, z_{min}	maximum and minimum of fracture profile height
α	ratio of true to projected fracture surface area
α_1, α_2	fitting parameters for hold time creep displacement
β	constant
χ	geometric parameter
Δ	diameter
ε_0	representative strain

$\dot{\varepsilon}$	indentation strain rate
ε_u	representative strain of 0.29
ϕ	weight factor in empirical relation of unloading curve
κ	constant ($\kappa = 3-4\nu$)
λ	scaling factor
ν	Poisson's ratio
ν_i	Poisson's ratio of diamond indenter
ρ	crack-tip radius
σ	indentation flow stress
σ_0	uniaxial flow stress
σ_u	flow stress at representative strain of 0.29
σ_y	yield stress
v	crack velocity
ξ	fractal correlation length
ξ_c	cross-over length of two fractal regimes
ψ	half included angle of indenter
ζ	roughness exponent
G, G_0	strain energy release rate, crack-tip strain energy release rate
AFM	atomic force microscope
COD	crack opening displacement
CT	compact tension
DI	<i>Digital Instruments Inc</i>
DMT	<i>Derjagin-Muller-Toropov</i> contact model
FT-IR	Fourier-transform infrared spectroscopy
FWHM	full width at half maximum
ICL	indentation crack length
ISE	indentation size effect
JKR	<i>Johnson-Kendall-Roberts</i> contact model
MEM	micro-electromechanical device

OFC	one-fold coordinated
PDC	precursor-derived ceramics
PSD	power spectral density
PTFE	polytetrafluoroethylene
PUMVS	poly(ureamethylvinyl)silazane
RMS	root-mean-square
RT	room temperature
SAED	selected area electron diffraction
SENB	single edge notched beam
SEM, FESEM, HRSEM	scanning electron microscopy, Field-emission scanning electron microscopy, High-resolution scanning electron microscopy
SIA	slit island analysis
TG	turbostratic graphite
TGA	thermogravimetric analysis
TMA	thermomechanical analysis
TEM, HRTEM	transmission electron microscopy, High-resolution transmission electron microscopy
UHV-AFM	ultra-high vacuum atomic force microscopy
XRD	x-ray diffraction

Abstract

This dissertation deals with the investigation of the deformation and fracture mechanical properties of precursor-derived (PDC) Si-C-N ceramics. The materials were synthesized from a liquid poly(ureamethylvinyl)silazane precursor. In order to access the intrinsic mechanical behavior of the materials, fully dense defect-free PDC specimens devoid of process induced features were fabricated using a special casting process and controlled thermolysis procedures. The investigations were performed on a range of Si-C-N-(H) PDC with progressively varying material structures from hydrogenated amorphous to phase separated nanocrystalline microstructures, from which the influence of material structure on the mechanical behavior was analyzed.

The crack-tip fracture toughness (K_{I0}) of the materials were evaluated using the novel crack opening displacement (COD) method from 'long cracks' realized from mode-I loading of rectangular shaped specimens using a specially made fixture, and in selected cases from radial cracks realized from Vickers indentation. The estimated K_{I0} values ranged from 0.6 to 1.2 MPa m^{1/2}. The variation in K_{I0} was well correlated with the structural evolution in the materials, effected by the progressive stripping of the one-fold coordinated hydrogen in the amorphous materials leading to increased network connectivity, and the nucleation and growth of turbostratic graphite (TG) and nanocrystalline SiC in the phase separated materials. Crack deflection observed even in the amorphous materials revealed the presence of structural and compositional inhomogeneities. In order to examine possible correlations of the geometrical contributions to toughening on the estimated K_{I0} values, and to probe the damage mechanisms operative at the propagating crack tip that manifest on the crack face morphology, roughness analysis of fracture surfaces was carried out. The fracture surface roughness was recorded by AFM topographic imaging, and was analyzed based on RMS roughness (R_q) and second order height-height correlation functions using the fractal approach. The evolution of R_q was well correlated with the

microstructural evolution responsible for crack deflection. Fractal analysis of the fracture surface roughness revealed self-affine scaling up to a correlation length of around 50 nm and a self-affine roughness exponent (ζ) of 0.8 ± 0.1 in all the materials, the latter in agreement with the universal roughness exponent conjectured in literature. However, no correlation was observed between the observed roughness exponents and the fracture toughness of the corresponding materials. The observed fractal correlation lengths were similar to that of silicate glasses, indicative of the length scales of the damage zones in the respective materials. Examination of the crack opening near the crack tip by high resolution AFM imaging revealed no persistent damage cavities along the crack, concluding that the fracture in the investigated Si-C-N ceramics proceeded in a brittle manner in the resolvable length scales, at crack velocities employed in the present experiments.

The deformation behavior of the present Si-C-N ceramics under contact loading conditions was investigated using blunt (spherical) as well as sharp (Vickers and Berkovich) indentation experiments. The elastic moduli and nanoindentation hardness evaluated from the analysis of the nanoindentation load-displacement curves correlated well with the evolution of material resistance to elastic and plastic deformation, commensurate with the structural and microstructural evolution in the materials. Analysis of the elastic and plastic deformation work quantities derived from the load-unload cycle in the Berkovich nanoindentation enabled the discrimination of the different plastic deformation characteristics of the amorphous and phase segregated materials. The plastic deformation of the amorphous Si-C-N materials displayed strong anomalous character identical to vitreous silica and induced appreciable strain hardening under progressive densification. This was manifested in the load dependant increase in hardness, to a measurable extent in the nanoindentation load regime and to an appreciable extent in the microindentation load regime. A semi-quantitative estimation of the yielding and strain hardening behavior was achieved using nanoindentation reverse analyses procedures that reasonably captured the evolution of material

resistance to plastic deformation in the materials. The anomalous densification behavior in amorphous Si-C-N materials also led to a load dependence of the strain rate sensitivity (m), also observed in vitreous silica, and controlled the evolution of indentation size effect (ISE). The evolution of strain rate sensitivity in the range of investigated materials showed good agreement with the cluster model, which relates the increase in the number density of isolated regions in the microstructure to a corresponding increase in m . Phase separation in the materials promoted the non-densifying mode of plastic deformation and led to a decrease in the strain hardening capability, increase in m and increased vulnerability to ISE.

1. Introduction

Precursor- derived ceramics (PDC) are materials synthesized by the pyrolysis of organometallic precursors of monomeric or polymeric structure with tailor-made chemical composition, in temperature and atmosphere controlled conditions. Due to the special nature of the synthetic process in use, the derived materials display drastic differences in terms of structure, chemical constitution and thermodynamic state compared to conventionally synthesized ceramics and as such represent a new class of materials. The above distinction also reflects in their physical and mechanical properties. The important attractions of PDC as structural materials are their low density, high hardness and elastic modulus, high stability and creep resistance at elevated temperatures and the high degree of attainable surface finish. Capitalizing on the versatility of chemical and polymer processing of precursors, PDC are applied in the form of composites, fibers, coatings and mini/micro- dimensional device components.

Obviously, structural applications of PDC are dependent on their deformation and fracture behavior, especially for room temperature service. These behaviors are grossly determined by their material structure and chemical bonding. As non-oxide PDC are predominantly covalently bonded and possess either an amorphous or nanocrystalline microstructure, their mechanical response under remote loading falls under linear elastic brittle fracture mechanics (LEFM) behavior, with practically insignificant contributions of toughening from their microstructure. While this necessitates incorporation of extrinsic toughening via microstructural engineering using second phase e.g., fiber, nanotube or particulate reinforcements, knowledge of the intrinsic fracture mechanical properties of the basic material is required for structural design. Apart from this application perspective, PDC being a distinct class of materials also offer scope for the study of their deformation and fracture behavior from a scientific perspective. The latter is facilitated by the possibility of controlling their final material structure by varying the extent of precursor-to-ceramic transformation by appropriate processing. Two possible scientific aspects of study with respect to

fracture behavior are (i) the study of the crack-tip toughness (K_{I0}) as a function of material structure and (ii) the study of damage mechanisms during fracture from micro- to atomic length scales. In contrast to the mechanical response under remote loading, PDC display significant plastic behavior at contact loading conditions, e.g., by sharp indentation. While the latter behavior is also observed in the mechanical response of ceramic materials and is realized due to the special nature of the contact stress field, the elastic and plastic deformation during sharp indentation of PDC are both qualitatively and quantitatively different from the general class of ceramics. This difference is characterized by a significant degree of material densification under the indenter, followed by a pronounced elastic recovery. This contrasting contact deformation behavior also merits investigation from both scientific and application point of views, as it has implications on the damage mechanisms under contact loading which is prevalent in tribological applications.

Investigations of the intrinsic deformation and fracture behavior of PDC strongly rely on the availability of suitable test specimens that truly reflect the material behavior, with sufficient dimensions amenable to experimental procedures. However, the pronounced volumetric shrinkage and the evolution of gaseous by-products during the synthesis and fabrication of PDC leads to considerable transformation stress gradients and poses a great challenge in obtaining fully dense defect-free bulk test specimens. This necessitates appropriate control of the fabrication procedure in minimizing or eliminating the above effects in order to obtain test specimens of reasonable dimensions and structural homogeneity on one hand, and the choice of suitable test methods that accommodate the limitations of the achievable test specimens on the other.

The objective of the present work is to characterize the intrinsic room temperature deformation and fracture mechanical behavior of precursor-derived ternary silicon carbonitride ceramics synthesized. The choice of this material system stems from the following two reasons: (i) the commercially available Si-C-N polymeric precursor poly(ureamethylvinyl)silazane (PUMVS) possesses

advantageous processing characteristics that allow the fabrication of fully dense representative test specimens (ii) Si-C-N PDC are finding widespread commercial applications in various forms. Although this study focuses on the silicon carbonitride PDC, the developed understanding is expected to be qualitatively applicable to all the silicon based PDC (*viz.*, Si-C, Si-C-O, Si-N, Si-C-N and Si-B-C-N.) due to the gross similarity of their structures and phase evolution, which is now well documented.

The results of the investigations are presented and discussed in four chapters, with each one focusing on the individual aspects as identified above. The chapters are formulated in the style suitable for publication in peer-reviewed journals. While each chapter is written in a self contained manner to the extent possible, some information with respect to material preparation and structural characterization are either repeated or cross-referenced to enable continuity of discussion and easy understanding.

Chapter 2 describes the fabrication of fully dense Si-C-N ceramic test specimens using a casting method, where the factors affecting the fabrication of dense monoliths are identified and the strategies in controlling these factors are discussed. A detailed characterization of the structural evolution in the resultant materials, realized from controlling the degree of ceramization is presented using infrared and Raman spectroscopy, X-ray diffraction and high-resolution transmission electron microscopy. A preliminary evaluation of the physical and mechanical properties is also included.

Chapter 3 presents the characterization of the intrinsic crack-tip fracture toughness (K_{I0}) of the above Si-C-N-(H) materials using a novel crack opening displacement (COD) method. The variation of K_{I0} in the materials is correlated and discussed in terms of the material structure, phase evolution and microstructure. The variations are also examined in the light of fractographic analysis using AFM towards understanding the toughening contributions from a microstructural aspect.

In Chapter 4, possible correlations of the fractal scaling of fracture surface roughness (characterized by the fractal dimension (D) or roughness exponent (ζ) of the fracture surface), with respect to fracture properties and fracture damage mechanisms are examined. Fractal analysis of fracture surfaces is still in the stage of evolution. In the literature, this approach has been applied towards (i) the qualitative and quantitative correlation of fracture toughness variations with fractal dimension D and (ii) the understanding of the physical process of fracture and damage mechanisms. Prominent among the latter approach is the identification of a change in damage mechanism at different length scales, according to the cross-over between different fractal regimes. In this work, roughness evolutions in the fracture surfaces of present materials are evaluated in light of both the above approaches. According to the latter approach, formation of damage cavities preceding fracture has been postulated to occur in amorphous ceramics in a similar manner to metals, with supporting experimental observations in silicate glasses. This possibility is also examined with respect to the fracture in the present amorphous Si-C-N materials, using high-resolution AFM imaging.

The elastic and plastic deformation behavior of Si-C-N PDC under contact loading is analyzed in Chapter 5, using depth sensing nanoindentation experiments. The nanoindentation elastic moduli and hardness of the amorphous and phase separated Si-C-N materials is evaluated and correlated with their structural evolution. Distinction in the plastic deformation character of amorphous and phase separated materials is identified. The evolution of material resistance to plastic flow is discussed in terms of the yielding and strain hardening behavior. The indentation size effect in the range of materials is examined in light of the work hardening behavior and the influence of strain rate. The variations in the strain rate sensitivity of materials and its load dependence is investigated using nanoindentation creep analysis and discussed according to the cluster model of material flow and the evolution of strain hardening.

2. Fabrication and characterization of fully dense Si-C-N ceramics from a poly(ureamethylvinyl)silazane precursor

2.1. Introduction

Polymer derived Silicon carbonitride (Si-C-N) ceramics are candidate materials for high temperature structural and functional applications in the form of fibers [87Leg, 88Cha, 00Mot], protective coatings [02Mot, 95Hei, 02Wag], fiber and particulate reinforced composites [04Lee] and more recently as components for micro-electro-mechanical devices (MEM) [01Lie]. The synthesis of these materials involves crosslinking and / or pyrolysis of suitable organo-silicon precursor polymers in an inert atmosphere, leading to ceramics with high purity, controlled structure and chemical composition [95Bil, 00Kro]. Depending upon the chemistry of the starting precursor and pyrolysis conditions, a range of material structures from fully amorphous to nano-crystalline ceramics can be produced, with associated influence on the material properties. Knowledge of their intrinsic physical and mechanical properties is of interest amongst others, both from scientific and application perspectives.

Experimental evaluation of these properties however, strongly relies on the availability of suitable samples that truly reflect the material behavior. Physical and mechanical characterization of these materials until now has been widely carried out [98Nis, 01Gal, 01Bau] using monolithic samples fabricated through a powder consolidation route [96Sei, 99Kon]. In this method, the crosslinked precursor powder with sufficient formability is warm-pressed under an optimized temperature-pressure program, yielding a green body with controlled porosity. The green body is in turn pyrolyzed at elevated temperatures to obtain a monolithic ceramic body albeit with residual porosity, invariably introduced to enable the escape of gaseous pyrolysis by-products. Also, the original particle boundaries of the starting powder can be still retained to varying extents depending on the conditions of warm pressing and / or reactivity of the powder,

leading to a pseudo-microstructure in an otherwise amorphous sample. Such features can adversely affect the evaluation of properties relating to fracture (through crack deflection along boundaries, arrest at pores etc.), and can significantly modify other properties, depending upon the extent, shape and distribution of such features and their interaction with the experimental conditions. Several hybrid methods have been described in literature to improve the bulk density of the powder derived ceramic bodies with varying success or applicability [98Gal, 00Wan, 02Ish]. However, for the characterization of the intrinsic mechanical properties of PDC, fully dense bulk specimens of sufficient size, and free of processing- generated pseudo-microstructure are necessary. A promising strategy is to fabricate fully dense monolithic infusible green bodies free of processing generated microstructure from suitable precursors, and a direct polymer to ceramic transformation of the green bodies using controlled pyrolysis. Depending upon the rheology, melting and crosslinking characteristics of the candidate precursor, the first step can be realized using either a warm consolidation – crosslinking or a casting – crosslinking procedure [96Fre, 02Sha]. The latter route is ideally suitable for crosslinkable liquid precursors.

The major difficulties with the fabrication of fully dense monolithic ceramics from liquid precursors are [96Mal, 00Li, 00Wan]

- (i) Bubble formation / foaming during thermal crosslinking
- (ii) Restriction of degassing during pyrolysis
- (iii) Material shrinkage

Bubble formation can occur due to the evaporation of the liquid precursor, the extent of which is determined by crosslinking temperature, heating rate, ambient pressure and polymer viscosity. A coupled increase of bulk density and the volume to surface ratio of the crosslinked green body restricts the removal of gaseous by-products released during pyrolysis reactions. This increases the pressure within the bulk of the body resulting in bloating / cracking. The above,

as well as any possible temperature gradient across the bulk can lead to a differential rate of polymer to ceramic transformation from surface to the core of the specimen, thereby, a differential shrinkage. This eventually results in cracking or complete disintegration of the pyrolyzed body. Considerable research has been carried out in the mathematical handling of the above problems [90Yao, 87Kay, 01Lew]. However, reports on the successful fabrication of dense monolithic ceramics from polymer precursors are limited. Freimuth *et al.* have reported the fabrication of miniaturized ceramic structures through the pyrolysis of green forms obtained using a solution casting process [96Fre]. The polymer forms were chemically crosslinked in air and the pyrolysis was conducted using extremely low heating rates (≤ 10 K/h) to realize crack-free structures with a thickness of the order of several micrometers. Shah *et al.* have recently developed a pressure casting technique [02Sha] that enables fabrication of amorphous Si-C-N ceramic specimens with a thickness of ≤ 0.5 mm.

This chapter describes an improved method for the fabrication of fully dense defect free ceramic bodies from a liquid poly(ureamethylvinyl)silazane (PUMVS) precursor, that are suitable for a range of physical and mechanical characterization experiments. While the methodology closely follows the work of Shah *et al.* [02Sha], capabilities with respect to the obtainable specimen thickness and material structures have been enhanced, and the need for employing a pressure vessel is eliminated. Additionally, the structural, physical and mechanical characterization of these specimens covering partly organic to nano-crystalline Si-C-N ceramics are presented.

2.2. Experimental procedure

The liquid precursor PUMVS, commercially known as *Ceraset*,[®] (KiON Corporation, Columbus, OH) was cast into a PTFE mold, hermetically sealed in a steel die and thermally crosslinked at 260°C for 5 h to form fully dense, transparent infusible green bodies. A schematic diagram of the mold-die

construction is shown in Fig. 2.1. The PTFE mold was made out of three circular PTFE discs of 1 mm thickness, the middle disc having a circular recess. The bottom and middle discs were glued together to form the mold cavity, using a thin layer of two-component epoxy glue. The liquid precursor was filled into the mold cavity, closed with the third disc, sandwiched together between the two halves of the steel die and tightened with screws. PTFE was chosen as mold material due to its easy formability and mold releasing characteristics. The die was placed in a quartz glass with Schlenk construction, which was

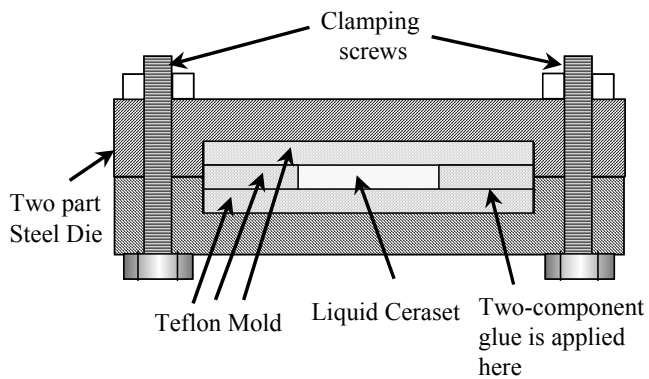


Fig. 2.1. Schematic diagram of the mold-die construction.

evacuated and back-filled with nitrogen. The entire assembly was then placed in a furnace and heated to 360°C using a programmable furnace controller. A higher furnace temperature was necessary to realize the actual crosslinking temperature of 260°C at the crosslinking die, which was monitored using a second thermocouple. The crosslinked green bodies were disc shaped, with a diameter of 19 mm and 1 mm thickness.

The mass loss and shrinkage behavior of the green bodies during pyrolysis were determined by thermo-gravimetric (TGA) and thermo-mechanical (TMA) analyses respectively ($RT \leq T_p \leq 1000^\circ\text{C}$; heating rate: 5 K/min; atmosphere: flowing argon). A crosslinked sample with a thickness of 1 mm was used for the TMA. The analyses were performed using a simultaneous thermal analyzer (model STA-409 Netsch) for TG and a thermo-mechanical analyzer (model TMA2000, Bähr thermoanalyse, Hillhorst, Germany) for TMA.

Several batches of green bodies were pyrolyzed in a flowing inert gas atmosphere using Schlenk tubes to various final temperatures (T_p) from 800°C to 1500°C in steps of 100°C to obtain ceramic samples with a range of material structures. For samples pyrolyzed up to 1000°C, a single stage pyrolysis schedule was employed (800°C $\leq T_p \leq$ 1000°C; heating rate: 100 K/h; hold time at T_p : 1 h; cooling rate: 300 K/h; atmosphere: flowing argon; Schlenk tube: quartz;). An additional heating ramp was included in the heating schedule for samples pyrolyzed at 1100°C, at 10 K/h from 1000°C to 1100°C. In order to control the temperature distribution and thereby the heat transfer to the green bodies during pyrolysis, several trials were carried out by changing the heat transfer media and sample placement. These methods are schematically illustrated in Fig. 2.2 and included (i) sandwiching the green bodies between or simply placing them on monolithic graphite blocks (ii) powder bed method, where the green bodies were packed in loose Si₃N₄, BN or graphite powder (iii) packing the green bodies within silica wool and (iv) sandwiching between porous graphite felt. The green samples along with the heat transfer media were packed within an alumina crucible, which was then placed in the Schlenk tube. As will be described in section 2.3.1, the arrangement with graphite felt was successfully used for the preparation of Si-C-N ceramics up to a pyrolysis temperature of 1100°C. A

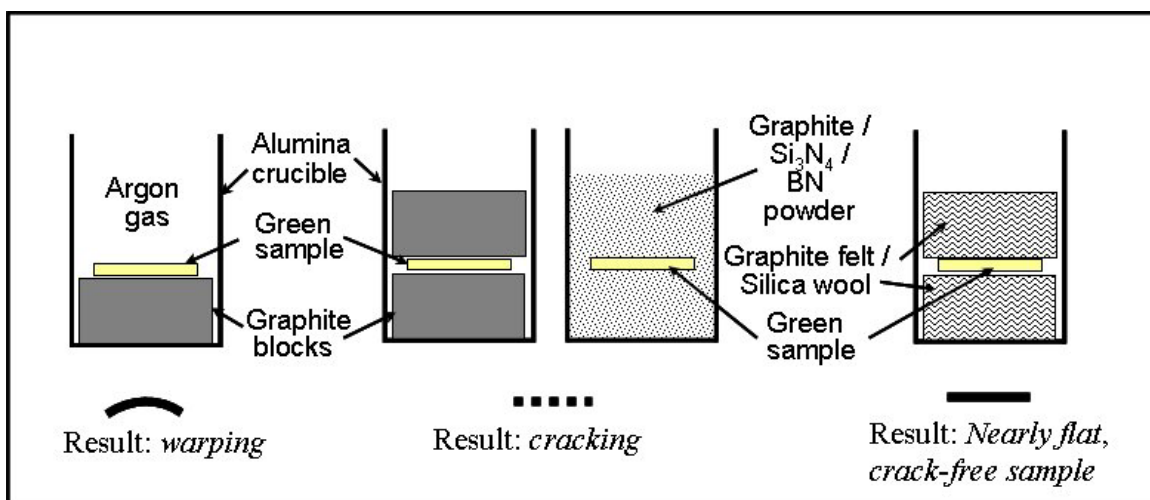


Fig. 2.2. Schematic illustration of the methods experimented using different heat transfer media and sample placement during pyrolysis for realizing crack-free dense Si-C-N ceramic specimens.

two-stage pyrolysis-annealing schedule was used for samples above 1100°C. In this case, Si-C-N ceramic samples were prepared at $T_p = 1000^\circ\text{C}$ in the first stage using the above method. In the second stage, these samples were mechanically ground and polished to remove surface defects, packed in boron nitride (BN) powder inside an alumina crucible and subjected to a second annealing treatment (heating rate: 100 K/h for $\text{RT} < T < 1000^\circ\text{C}$; 10 K/h for $1000^\circ\text{C} < T_p \leq 1500^\circ\text{C}$; holding time at T_p : 12 h; cooling rate: 300 K/h; atmosphere: flowing nitrogen; Schlenk tube: alumina;). In the following text, the samples will be referred according to their thermal treatment, e.g., SiCN-080001, SiCN-090001, SiCN-100001, SiCN-110001, SiCN-120012, SiCN-130012 and SiCN-150012, the first four digits denoting the temperature and the last two digits, the holding time of the pyrolysis or annealing treatment in hours.

Structural characterization of the samples was performed using FT-IR, Raman spectroscopy, X-ray diffraction (XRD) and high-resolution transmission electron microscopy (HRTEM). Infrared spectra were collected in transmission using KBr pellets (Nicolet spectrometer, Model Magna 560) in the wave number range 4000 cm^{-1} – 450 cm^{-1} and a spectral resolution of 4 cm^{-1} . Raman spectroscopy was carried out using a Jobin Yvon spectrometer (excitation source: He-Ne laser, $\lambda = 632.8\text{ nm}$; laser power: 0.004 – 0.4 mW; sample objective: 20X / 50X; spectral resolution: 4 cm^{-1}). For XRD analysis, a Siemens diffractometer (Model D5000 Kristalloflex; Cu- $K\alpha$ radiation, $\lambda=1.5406\text{ \AA}$) was employed. High-resolution transmission electron microscopy (HRTEM) was performed using a Philips CM200 (Philips Eindhoven, Netherlands) instrument. TEM samples were prepared according to the standard procedure, involving drilling, grinding, dimpling and finally ion-milling. In addition, light microscopy and scanning electron microscopy (SEM, model S200 – Cambridge instruments as well as FESEM, models DSM 982 Gemini and JEOL JSM 6300F) were utilized to examine polished as well as fracture surfaces of samples. Bulk chemical analyses were performed by atomic emission spectroscopy with inductively

coupled plasma excitation (for silicon), combustion (for carbon and hydrogen) and carrier gas hot extraction (for nitrogen and oxygen).

Density of the samples was measured by Archimedes method in water for monolithic samples, as well as by helium pycnometry (Micromeritics, Model Accupyc1330) for powdered samples. Young's modulus and Poisson's ratio were determined by the resonance frequency analysis method (RFDA, IMCE n.v., Dipenbeek, Belgium) using circular disc specimens with a diameter of 12 mm and a nominal thickness of 300 μm . The method involves the analysis of the resonance frequencies generated from the mechanical excitation of the specimen, which is then related to the specimen geometry, density and elastic modulus. Hardness of the samples was evaluated using Vickers diamond pyramid indentation under various loads viz., 0.245, 0.490, 0.981, 1.962, 4.905, 9.81, 19.62 and 49.05 N. Thermal diffusivity of the samples was determined by the laser flash method, using circular disc specimens as above.

2.3. Results

2.3.1. Fabrication of fully dense samples

A temperature-time combination of 260°C – 5 h was found to be optimum for the crosslinking of the liquid PUMVS precursor to yield hard, fully dense and transparent green bodies. While the use of higher temperatures initiated the deformation of PTFE mold, use of lower temperatures or holding times resulted in insufficient crosslinking, producing rubber-like bodies.

The pyrolysis of green bodies was found to be the critical step in the fabrication of dense ceramic specimens. Pyrolysis of dense green bodies with thickness higher than 2 mm always resulted in bloating (Fig. 2.3) accompanied by severe cracking. Samples with thickness ≤ 1 mm did not show bloating; however, mild to extensive cracking was observed. Light microscopy of cross sections of the fragments themselves confirmed the absence of bloating, gas bubbles or

porosity, within the resolution of the technique. Severity of cracking appeared to be reduced by reducing sample thickness below 1 mm, but was not eliminated. Up to a pyrolysis temperature of 1000°C, cracking was not affected by surface finish or any other stress raising features in the green bodies. Also, in the same temperature range, heating rate did not have a significant influence on the above results. To elaborate, cracking occurred even with a heating rate as low as 5 K/h.

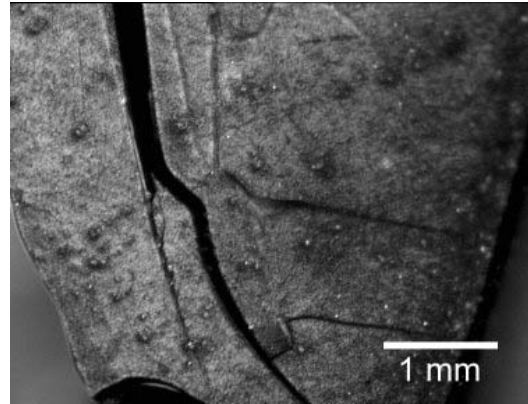


Fig. 2.3. Light micrograph of a sample pyrolyzed at 1000°C – 1h, from a fully dense green body with a starting thickness of 2 mm; blisters due to bloating and severe cracking are evident.

In order to control the heat transfer to the samples during pyrolysis, different arrangements with respect to the sample placement were tried (Fig 2.2). When placed on a flat graphite block with the top surface open to the atmosphere, samples showed warping into a dish shape, concave downwards, with little or no cracking. Thinner samples favored warping to cracking than thicker samples, where warping and cracking were inversely related. Pyrolysis of samples sandwiched between two graphite blocks always led to complete cracking. Use of powder bed techniques with graphite, Si₃N₄ or BN powders also could not avert cracking during the pyrolysis of green bodies. However, interestingly, when wrapped in silica wool, they could be pyrolyzed free of cracks with only mild warping, which was concentrated in regions where packing density of silica wool was high. Taking lead from this, the dense green bodies were pyrolyzed as sandwiched between two porous graphite felts. This yielded dense ceramic bodies free of cracks and with minimal warping up to 1000°C, in spite of the relatively high heating rate of 100 K/h employed. Note that this heating rate is higher by a factor of 4 to 10 times than those employed by Shah *et al.* and Freimuth *et al.* [96Fre, 02Sha]. For samples pyrolyzed at 1100°C, a reduction of

heating rate to 10 K/h was necessary above 1000°C to avert cracking. A photograph of typical samples before and after pyrolysis is given in Fig. 2.4. SEM micrographs (Fig. 2.5) of the SiCN-110001 sample at various magnifications substantiate the dense structure of the material.

For the preparation of homogeneous Si-C-N ceramic samples subjected to thermal treatment above 1100°C, use of graphite felt as heat transfer medium was found unsuitable. This was due to the chemical interaction between Si-C-N sample and graphite felt in contact resulting in accelerated crystallization at and near the sample surface, producing a layered microstructure across the sample thickness. Cracks initiated and propagated from stress raising features (such as surface and edge roughness), particularly favored by the accumulated residual stresses during pyrolysis. To counter the above, two modifications were applied for samples prepared at T_p above 1000°C. A two stage pyrolysis-annealing sequence was adopted as described in

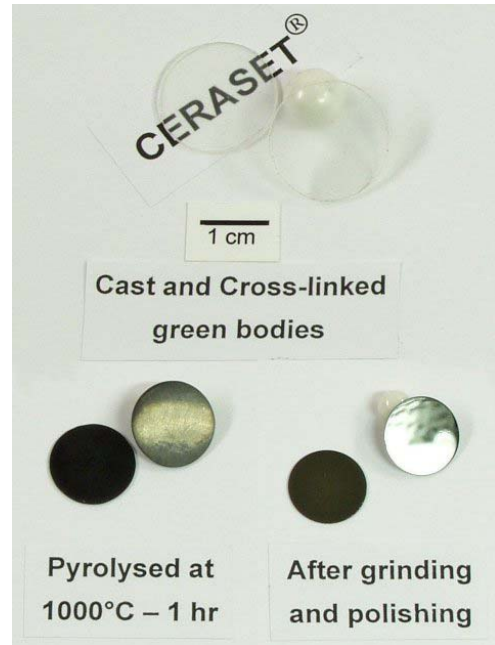


Fig. 2.4. Typical fully dense samples at various processing conditions.

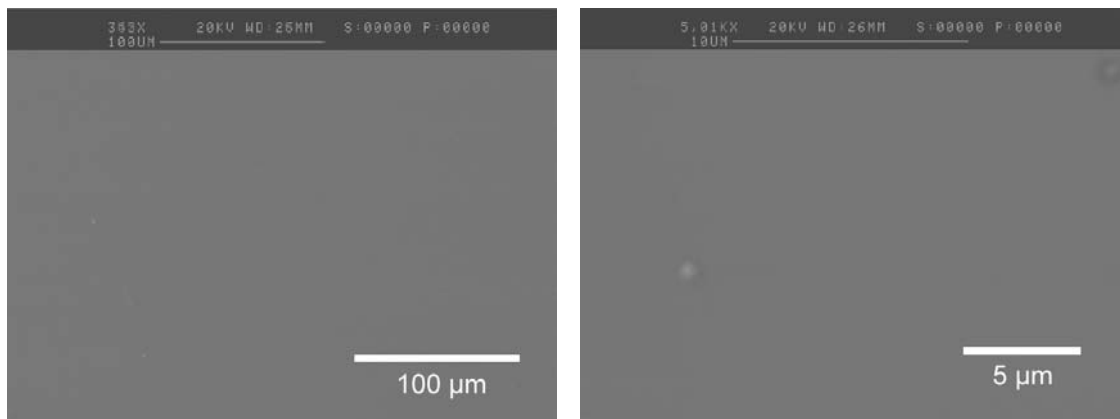


Fig. 2.5. SEM micrographs at two magnifications from the polished surface of the SiCN-110001 sample corroborating the dense pore free structure.

section 2.2, with an intermediate grinding and polishing procedure applied to relieve the accumulated residual stresses and to remove the surface defects. The active chemical reactions with the pyrolysis environment such as the above were obviated by the use of a BN powder bed (which is chemically inert to Si-C-N ceramics at the employed temperatures) and a flowing nitrogen gas atmosphere. This procedure yielded fully dense crack-free samples with an acceptable homogeneous microstructure up to an annealing treatment at 1300°C /12h, where the affected layer thickness was 50 to 100 μm from the sample surface (Fig. 2.6). Heterogeneous features appeared across the sample cross section at annealing temperatures above 1400°C, and are evident from the fractured as well as polished cross sections of SiCN-150012 sample (Fig. 2.7). A

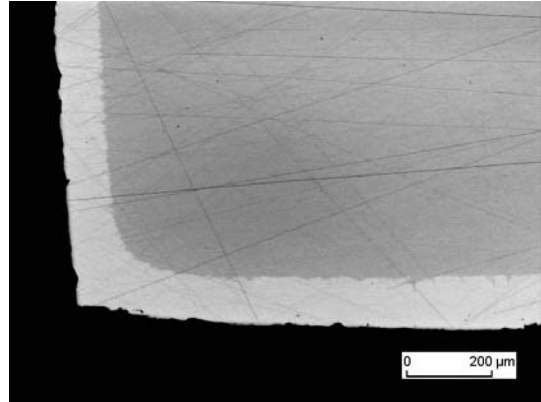


Fig. 2.6. Polished cross-section of the SiCN-130012 sample.

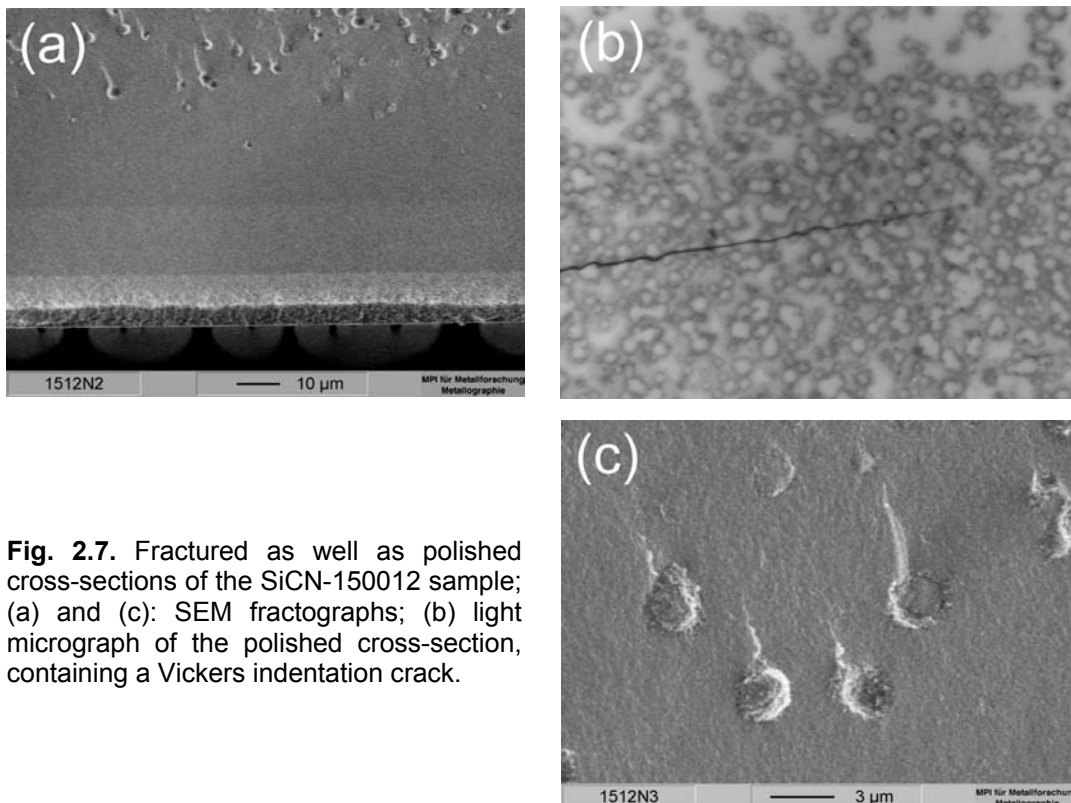


Fig. 2.7. Fractured as well as polished cross-sections of the SiCN-150012 sample; (a) and (c): SEM fractographs; (b) light micrograph of the polished cross-section, containing a Vickers indentation crack.

layered microstructure near the surfaces, accompanied by globular features spreading along the middle plane of the sample thickness is observed (Fig. 2.7(a)). A crack introduced in this region through Vickers indentation propagated across as well as around these globular features (light micrograph, Fig. 2.7(b)). That the fracture occurred through as well as around the globules is discerned from the SEM fractograph at higher magnification (Fig. 2.7(c)), where the globular features appear as flat, concave as well as convex surfaces, suggesting that these features were not closed pores, but dense material separated from the matrix along a weak interface. Although free from porosity, these samples cannot be used for physical and mechanical characterization, as the microstructure is not homogeneous across the cross section.

2.3.2. Chemical and structural characterization

2.3.2.1. Bulk chemical analysis

The elemental compositions and the empirical formulas of the thermolyzed samples at different temperatures from 800°C to 1300°C are given in Table 2.1. Interestingly, the analyses showed almost no variation in silicon, carbon and nitrogen content. However, the samples pyrolyzed at lower temperatures contained appreciable quantities of hydrogen. Hydrogen content decreased continuously with increasing thermal treatment, falling below the detection limits in SiCN-120012 and SiCN-130012. Considerable oxygen contamination was also

Table 2.1. Elemental composition of the specimens as a function of pyrolysis temperature, determined from bulk chemical analysis.

Sample	Elemental composition										Empirical formula
	Si		C		N		H		O		
	(Wt%)	(At%)	(Wt%)	(At%)	(Wt%)	(At%)	(Wt%)	(At%)	(Wt%)	(At%)	
SiCN-080001	52.6	25.86	22.4	25.75	20.6	20.3	1.9	26.02	2.4	2.07	SiCN _{0.78} O _{0.08} H
SiCN-090001	52.7	27.33	22.2	26.92	22.2	23.09	1.48	21.39	1.4	1.27	SiC _{0.98} N _{0.84} O _{0.05} H _{0.78}
SiCN-100001	53	29.56	22.7	29.6	21.2	23.71	0.97	15.07	2.1	2.06	SiCN _{0.80} O _{0.07} H _{0.51}
SiCN-110001	54	31.31	22.1	29.96	21.5	24.99	0.75	12.12	1.6	1.63	SiC _{0.98} N _{0.80} O _{0.05} H _{0.39}
SiCN-120012	52.5	33.85	21.4	32.26	20.1	25.98	< 0.1	< 1.8	5.4	6.11	SiC _{0.95} N _{0.77} O _{0.18}
SiCN-130012	54.7	35.45	21.1	31.98	20.6	26.77	< 0.1	< 1.8	4.3	4.89	SiC _{0.90} N _{0.76} O _{0.14}

present in the samples, resulting from the handling of green bodies in air. Assuming that the silicon atoms bond to oxygen, nitrogen and carbon atoms corresponding to equivalent stoichiometric quantities of SiO_2 , Si_3N_4 and SiC , the amount of ‘free carbon’ in the material can be calculated for SiCN-120012 and SiCN-130012 from their empirical formulas and are given as $\text{SiC}_{0.33}\text{N}_{0.77}\text{O}_{0.18} + 0.62 \text{C}_{\text{free}}$ and $\text{SiC}_{0.36}\text{N}_{0.76}\text{O}_{0.14} + 0.54 \text{C}_{\text{free}}$ respectively.

2.3.2.2. FT-IR

The transmission FT-IR spectra (Fig. 2.8) depict the structural changes in the samples with increasing thermal treatment. The spectrum from SiCN-080001 sample shows a broad composite absorption band of higher relative intensity in the range $800 - 1100 \text{ cm}^{-1}$ as well as lower intensity bands at 2129 , 1403 , and 1255 cm^{-1} (as a shoulder). The composite band comprises of superposed Si-N (910 , 985 , and 1040 cm^{-1}) [81Wad] and Si-C (780 and 900 cm^{-1}) [02Jan] bond vibrations, while the low intensity bands arise from Si-H, C-H, and Si-CH₃ vibrations respectively [00Kro]. With increasing pyrolysis temperature, the Si-H, C-H, and Si-CH₃ bands decreased in intensity further, and were undetectable in the SiCN-110001 sample. A simultaneous increase in the intensity of the Si-C bands relative to the Si-N bands was observed, evident from the change of shape of the composite peak. The features located around 1610 cm^{-1} are attributable to the oxygen or moisture contamination during handling of the samples in air.

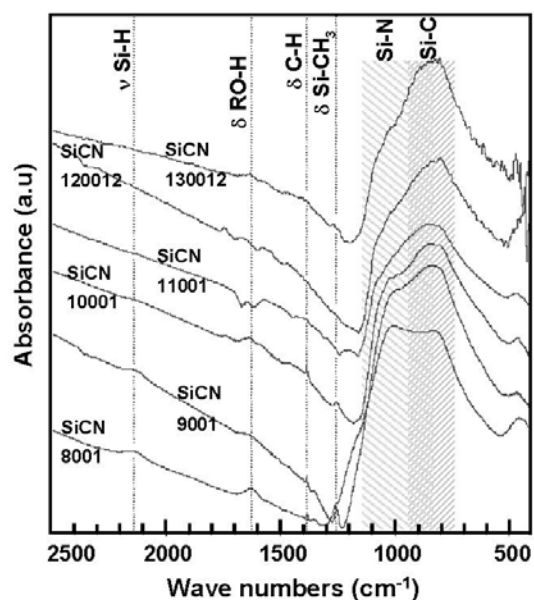


Fig. 2.8. Transmission FT-IR spectra of Si-C-N samples pyrolyzed or annealed at various temperatures between 800 and 1300°C .

2.3.2.3. Raman spectroscopy

Fig. 2.9(a) shows the Raman spectra recorded from the samples pyrolyzed at different temperatures. The overall relative intensities of the spectra progressively decreased with increasing pyrolysis temperature. The presented spectra are therefore suitably rescaled for better clarity. The spectrum from the SiCN-080001 sample displayed no phonon modes but only a large background signal. While the background intensity was still appreciable in the spectrum of the SiCN-090001 sample, two peaks centered around 1320 cm^{-1} and 1600 cm^{-1} were discernable, that correspond to the D and G peaks observed in disordered carbons [70Tui, 01Fer]. The G peak arises from the stretching mode (E_{2g}) of the sp^2 C-C bonds, whereas the D peak originates from the breathing mode (A_{1g}) of the sp^2 rings [01Fer]. The background signal in these spectra is due to the strong photoluminescence, which characterizes the polymeric nature of these samples containing appreciable quantities of hydrogen [01Fer, 00Fer]. In the spectra of samples from higher thermal treatment, the D and G peaks were better resolved against a lower background. Additionally, new peaks appeared centered at around 2620 cm^{-1} , 2920 cm^{-1} and 3230 cm^{-1} and are attributed to the overtones or combinations of the above mentioned first order phonon modes [79Nem, 90Wan]. In order to appreciate the structural changes in the samples with increasing thermal treatment, a multiple peak curve fitting procedure using four

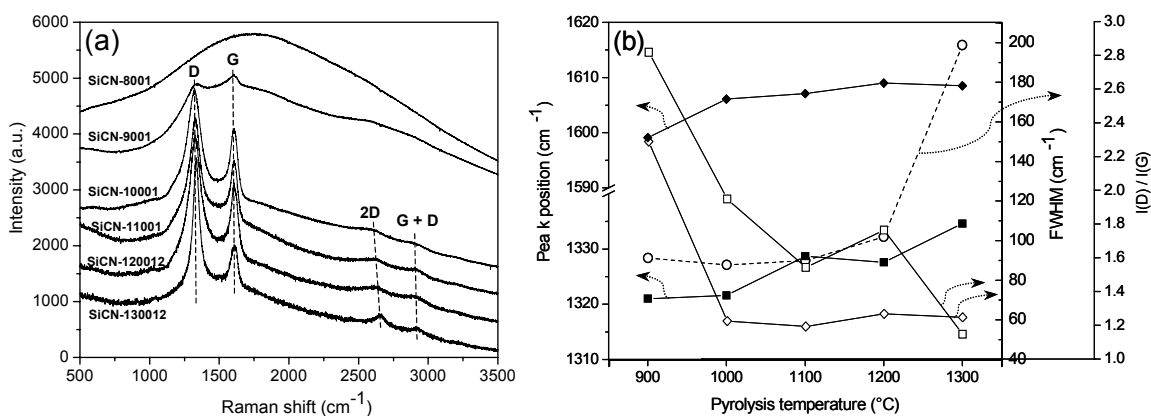


Fig. 2.9. Raman analysis of Si-C-N samples pyrolyzed or annealed at various temperatures between 900 – 1300°C; (a) Raman spectra showing the evolution of D and G peaks (b) Variation of D and G peak positions, FWHM and the intensity ratio $I(D) / I(G)$ with thermal treatment.

Lorentzians (one each for the D and G peaks and the remaining two to account for the features around $\sim 1200\text{ cm}^{-1}$ and $\sim 1500\text{ cm}^{-1}$) was applied to the spectra to extract information *viz.*, peak position, peak width (Full Width at Half Maximum, FWHM), and relative intensity. The data are plotted in [Fig. 2.9\(b\)](#). With increasing pyrolysis temperature the D peak showed a small but continuous upward shift in position and a steady decrease of its peak width (FWHM_D). Also, a simultaneous increase of its relative intensity $I(D)$ compared with that of the G peak ($I(G)$) was observed, quantified as the net increase in the intensity ratio $I(D)/I(G)$. In contrast, the G peak position and width (FWHM_G) stabilized at 1000°C and showed negligible variation above this temperature.

The population of all C-C bonds and the distribution of the C-C bond angle determine the intensity and the width of the G peak respectively. The presence of G peak in the spectrum from SiCN-090001 signifies the early inception of disordered sp^2 carbon clusters in the material. This combined with the presence of D peak indicates that at least a significant fraction of carbon atoms are bonded as ring-like configurations. The D peak shift, peak width and intensity are correlated to the distribution of cluster size and order of carbon atoms. An increase in the number of ordered six-fold aromatic rings shifts the D peak upwards and increases its intensity, while the presence of *non-aromatic* disordered ring-like configurations increases the peak width at the cost of intensity [[00Fer](#)]. The increase of the intensity ratio $I(D)/I(G)$ and the decrease of the D peak width thus correspond to the increase in the ordering of the clusters into aromatic graphene layers. The above results in total indicate the segregation, ordering and growth of carbon clusters towards the formation of nano-crystalline graphitic regions, in samples from higher thermal treatment.

2.3.2.4. X-ray diffraction

The results of the XRD measurements are compiled in [Fig. 2.10](#). XRD patterns of the samples pyrolyzed up to 1100°C showed no diffraction lines, but only broad

diffraction humps, typical of amorphous materials. XRD pattern from SiCN-120012 sample showed a single broad peak centered at $2\theta = 36^\circ$. The intensity and sharpness of this peak increased in the SiCN-130012 sample, along with the appearance of two broad peaks centered at $2\theta \approx 61^\circ$ and 72° respectively. Together, these three peaks indicate the nucleation of α/β -SiC. Additionally, a broad feature in the 2θ range between 21° – 30° was observed. Referring to the phase analysis of similar precursor derived ceramics [02Jan, 02Hau], this can be attributed to the formation of the turbostratic carbon phase ($2\theta_{(200)\text{-Graphite}} = 26.592^\circ$). Strong diffraction peaks corresponding to α -Si₃N₄ and α -SiC were observed in the SiCN-150012 sample, indicating appreciable crystallization at this annealing temperature.

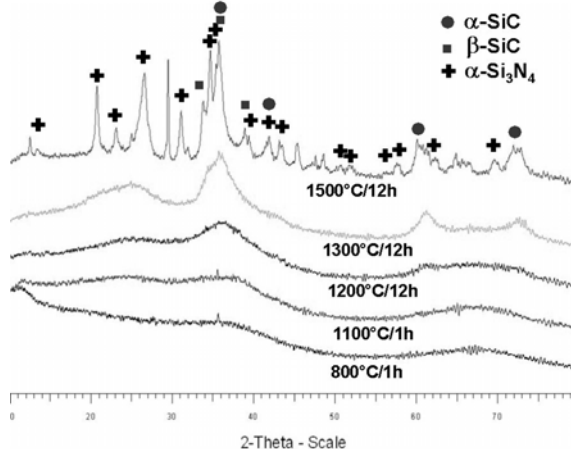


Fig. 2.10. X-ray diffraction patterns of Si-C-N samples pyrolyzed or annealed at various temperatures between 800°C to 1300°C .

2.3.2.5. High-resolution transmission electron microscopy

Microstructural evolution in samples treated at higher temperatures were analyzed using transmission electron microscopy under high-resolution. Accordingly, the high-resolution images along with the selected area electron diffraction (SAED) patterns from SiCN-110001, SiCN-120012 and SiCN-130012 samples were obtained and are presented in Fig. 2.11. The SAED patterns from SiCN-110001 and SiCN-120012 showed only diffuse halos typical of amorphous materials. TEM examination of the samples pyrolyzed below 1100°C (e.g., SiCN-100001) using SAED and high resolution imaging revealed no structural features resolvable by electron diffraction and as such these materials can be classified as ‘electron-amorphous’ [96Mon]. However, the high-resolution image

from the SiCN-110001 sample contained regions of tiny layer-like curved features. The insets within the main image depict enlarged views of the regions of interest for clarity (Fig. 2.11(a)). While the morphology of these features is not readily discriminable from the surrounding matrix, comparison of similar features in higher temperature treated samples indicates that these are indeed precursors to the nano-scale clustering of the turbostratic graphite phase [96Mon, 05Gre, 01Tur]. This is evidenced from the HR image of the SiCN-120012 sample (Fig. 2.11(b)). The turbostratic phase (marked *B* in the insets) in the latter sample displayed improved ordering than the former, with the size ranging between 5 to 10 nm along the layers. The organization and size further improved in the SiCN-130012 sample in directions along as well as perpendicular to the graphitic planes by stacking of several layers. The typical dimensions of the layers ranged from 15 to 30 nm along

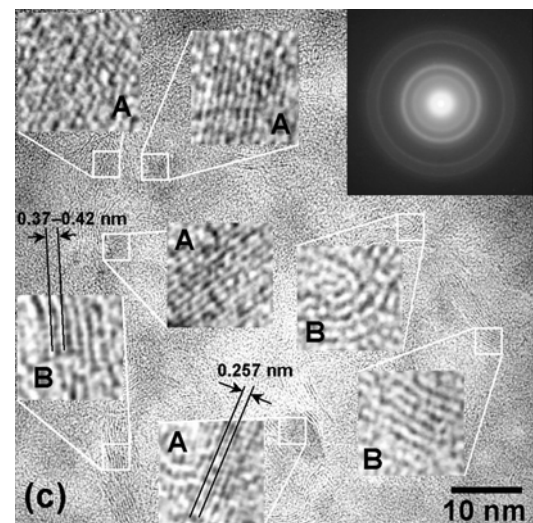
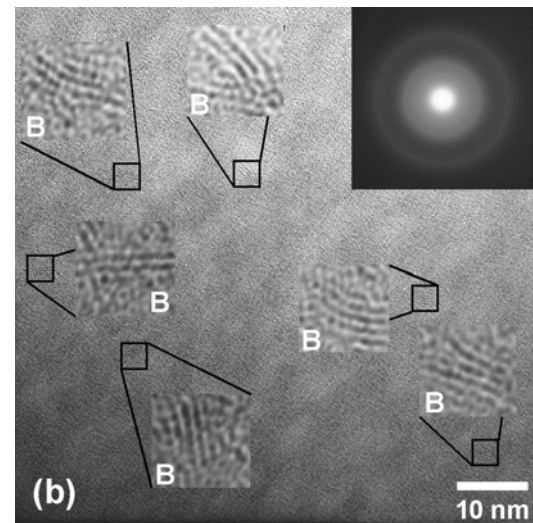
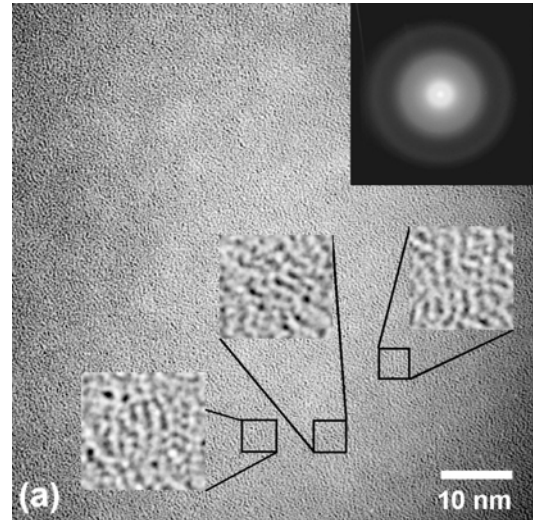


Fig. 2.11. HRTEM analysis of samples subjected to higher thermal treatment: (a) SiCN-110001 (b) SiCN-120012 (c) SiCN-130012; The SAED patterns of the representative regions are also included as insets. Additional insets show enlarged views of the details of interest: A – SiC nano-crystals; B – turbostratic graphitic clusters.

the layers consisting of seven to eight layers in a stack [96Mon]. The inter-layer spacing however was appreciably different from that of crystalline graphite, and varies between 0.37 to 0.42 nm. Concurrent to the growth and ordering of the turbostratic graphitic phase, nucleation of nano-crystalline silicon carbide was observed in the SiCN-130012 sample [96Mon]. The SAED pattern from this sample (Fig. 2.11(c)) showed three high relative intensity diffraction rings at $\sim 4 \text{ nm}^{-1}$, $\sim 6.5 \text{ nm}^{-1}$ and $\sim 7.5 \text{ nm}^{-1}$ corresponding to the $(111)_{\beta\text{-SiC}}$, $(220)_{\beta\text{-SiC}}$ and $(311)_{\beta\text{-SiC}}$ planes. The insets show high-resolution images of typical nano-crystallites (marked A). The inter-planar spacing was measured to be 0.257 nm, which corresponds to the d -spacing of the $(111)_{\text{SiC}}$ planes.

2.3.3. Physical and mechanical characterization

The density, hardness and elastic constants of the investigated materials are summarized in Table 2.2. The density of the fully dense green bodies was 1.1 g/cm^3 . With increasing pyrolysis treatment, the density monotonically increased from 1.85 g/cm^3 for SiCN-080001 sample to 2.15 g/cm^3 for the SiCN-120012 and SiCN-130012 sample, indicating the densification of the material structure. The Young's modulus determined from the resonance frequency method increased with thermal treatment to a maximum of 140 GPa in SiCN-120012 sample, above which it dropped to 117 GPa in SiCN-130012 sample. In contrast, Vickers hardness found a maximum in SiCN-100001 sample at 11.3 GPa. This variation in the elastic and plastic response of the material is further discussed in section 2.4.

Table 2.2. Physical and mechanical properties of the pyrolyzed specimens as a function of the temperature of pyrolysis.

Sample	Density (g/cm^3)	Youngs modulus (GPa)	Poisons ratio	Hardness (GPa)	Thermal diffusivity $\times 10^{-7} \text{ (m}^2/\text{s)}$
SiCN-080001	1.85 ± 0.02	82 ± 1	0.245 ± 0.015	8.3 ± 0.1	5.07 ± 0.31
SiCN-090001	1.90 ± 0.02	106 ± 1	0.24 ± 0.005	9.5 ± 0.3	4.95 ± 0.07
SiCN-100001	2.00 ± 0.02	117 ± 1	0.22 ± 0.003	11.3 ± 0.4	4.14 ± 0.24
SiCN-110001	2.10 ± 0.02	127 ± 1	0.21 ± 0.005	9.7 ± 0.4	3.99 ± 0.23
SiCN-120012	2.16 ± 0.02	140 ± 4	0.22 ± 0.01	9.6 ± 0.3	5.50 ± 0.27
SiCN-130012	2.15 ± 0.02	117 ± 4	0.23 ± 0.01	7.9 ± 0.2	8.08 ± 0.16

2.4. Discussion

Cross linking of the liquid precursor by heating without pressure leads to the formation of gas bubbles in the green body due the evaporation of low molecular weight oligomers, dissolved gases and / or dissociation of weakly attached end groups. This is obviated in the present method by heating the precursor confined in a steel die, where the generated internal isostatic pressure eliminates bubble formation and yields fully dense glassy green bodies. Extensive gas evolution [01Li] and coupled mass loss occurs during pyrolysis of green bodies in the temperature window of 400 – 800°C (Fig. 2.12). Restriction of the gas evolution in thicker samples (> 1.5 mm) leads to bloating near the free surface and pressure build up in the sample core. Extensive bloating has been observed previously in the pyrolysis of powder-derived green bodies containing a higher fraction of closed pores, resulting from the higher warm pressing temperatures employed [02Bau]. The relatively softer material at the initial stage of pyrolysis accommodates the stresses by deformation [99Kon, 01Wan]. However, the progressing ceramization at higher pyrolysis temperatures renders the material stiff, leading to the cracking of the bodies. Limiting the green body thickness to 1 mm eliminates the gas pressure induced stresses. In this case, the diffusion through the relatively open structure of the green body sufficiently allows the escape of gaseous pyrolytic products. A more critical problem is the differential rate of polymer to ceramic transformation across the sample thickness, mainly arising from the differential heat transfer at the surface and the core regions. In the experiments, samples pyrolyzed as sandwiched

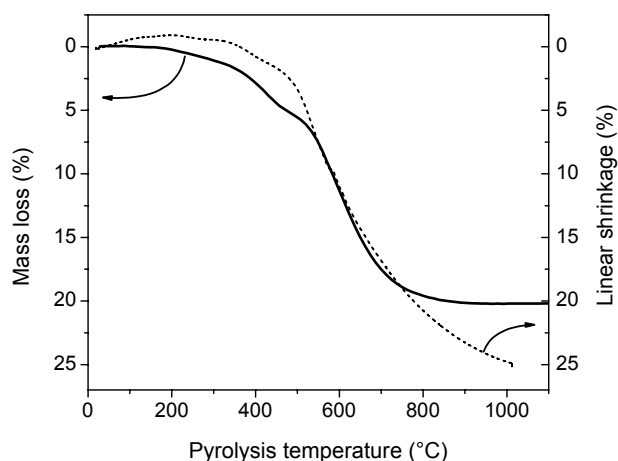


Fig. 2.12. Mass loss and linear shrinkage behavior during the pyrolysis of the cross-linked Si-C-N green bodies, recorded from TG and TMA analyses respectively.

between graphite blocks or packed in a powder bed were always cracked, whereas those pyrolyzed as simply supported on a single graphite block were warped. The relatively higher thermal conductivity of these heat transfer media in contact with the sample, in combination with the poor thermal conductivity of the sample, induces significant thermal gradients across the sample thickness. The consequent differential ceramization and the differential pyrolytic shrinkage produce transformation stresses, leading to cracking or warping of the samples. The porous graphite felt used as sample support and heat transfer medium in the present work possesses a low thermal conductivity, and thus effectively moderates the conductive heat transfer to the samples, reducing the thermal gradients to tolerable levels, while the porosity facilitates the escape of pyrolytic gases. The resulting ceramic bodies are dense and crack-free up to a pyrolysis temperature of 1100°C, albeit containing considerable residual stresses. The intermediate machining of the amorphous samples in addition to the removal of surface defects and chemical contamination, serves to relieve these stresses, enabling the successful fabrication of phase segregated samples through the second stage annealing treatment. Removal of residual stresses is also a prerequisite for the meaningful mechanical characterization of these materials.

A detailed account of the polymer to ceramic transformation of the PUMVS precursor has been described by Kroke *et al.* [01Li]. The chemical and structural characterization presented here highlights the change in the material structure of the fully dense Si-C-N-(H) ceramic specimens thermolyzed from the above precursor to varying degrees of conversion, such that a correlation to the physical and mechanical behavior can be examined. The chemical composition of the all the thermolyzed specimens remains nearly invariant, barring hydrogen content. This is due to the completion of the majority of the pyrolytic reactions by 800°C, as revealed by the TG (Fig. 2.12) and TG coupled mass spectrometry [01Li]. The materials from thermolysis treatments up to 1000°C display partly organic character, with an open network structure of mixed $\text{SiC}_x\text{N}_{(4-x)}$ tetrahedra [01Li] containing methyl and / or hydrogen terminations. The reduction of hydrogen

content from 26 at.% in SiCN-080001 to less than 2.8 at.% in SiCN-120012 is mainly responsible for the pyrolysis shrinkage still observed beyond 800°C (Fig. 2.12). While the IR spectra register the decrease in Si-H, Si-CH₃ and C-H band intensities, quantitative information regarding the fractions of the total hydrogen content removed from Si-H and C-H terminations is lacking. However, aggregation of *sp*²- carbon into graphitic clusters is detected by Raman analysis in samples thermolyzed above 800°C. Using simple charge balance considerations, the amount of excess free carbon is estimated from the elemental analysis data, in the hydrogen free SiCN-120012 and SiCN-130012 samples. Reckoning the invariance of the C/Si and N/Si molar ratios, an equivalent quantity of excess carbon can be expected also in the lower temperature thermolyzed samples, although its organization will depend upon the amount of hydrogen bonded to them. The role of hydrogen depletion in the organization of the polyaromatic carbon in PDC has been reported previously [96Mon, 05Gre]. Accordingly, the growth of the graphitic phase proceeds through the stripping of peripheral hydrogen from the H-terminated graphene layers and their subsequent edge-wise association. Recalling the simultaneous increase in the Si-C bond population inferred from IR spectra, it can be concluded that the progressive hydrogen depletion leads to an increase in the structural density of the thermolyzed materials, through the increased network connectivity of SiC_xN_(4-x) units as well as the organization of the graphitic phase. Although the latter process starts as early as by 800°C pyrolysis, the size of the graphitic domains remain below the critical level in order to be identified as separate phase, up to 1100°C. Thus, all the samples thermolyzed up to this temperature are amorphous as confirmed by XRD as well as by HRTEM. The phase separation in the material occurs at 1200°C, beginning with the formation of turbostratic graphite and the nucleation of nano-crystalline SiC at 1300°C thermolysis.

The effect of the above structural changes is reflected in the physical and mechanical properties of the materials. The increase in the density, elastic modulus and hardness of the materials thermolyzed up to 1000°C is easily

explained in terms of the increased network connectivity realized from the stripping of hydrogen. The change in the elastic and plastic response beyond 1000°C thermolysis stems from the difference in the nanostructure of the materials. Above this temperature, the size of the graphitic nano-domains reaches a sufficiently high value such that shear deformation is promoted, decreasing the hardness. The growing domains do not immediately degrade the material stiffness, as they remain dispersed as isolated regions in the amorphous network. Interestingly, a recent DFT study of the free carbon in a:Si-C-O materials suggests that the graphitic precipitate bonded to the amorphous network stiffens the structure by decreasing the amount of floppy modes in the structure [05Kro]. In the present case, the increasing modulus of the specimens up to 1200°C thermolysis coincides with the elimination of hydrogen. At still higher thermolysis temperatures, the growth of the turbostratic graphite phase leads to significant impingement of the layers, as can be partly appreciated from the HRTEM images of the SiCN-130012 sample (Fig. 2.11). The decrease in the elastic modulus of the SiCN-130012 specimen is thus attributed to the direct interaction of graphitic precipitates. This is supported by the measured thermal diffusivities of the samples, which show a drastic increase in the SiCN-130012 sample. Electrical conductivity measurements on similar Si-C-N ceramics have displayed an appreciable increase in conductivity, when the growth of turbostratic graphite reached the percolation limit [03Tra].

From the above discussion, it is evident that the fully dense Si-C-N PDC specimens prepared in this work are suitable for the characterization of their intrinsic mechanical behavior. However, it is to be noted that the structure of the synthesized ceramics are strongly dependant on the processing parameters *viz.*, crosslinking and pyrolysis temperatures, heating rate, holding time and atmosphere employed. Obviously, the properties of Si-C-N ceramics prepared using different processing parameters can be different. This is also true even for materials which are nominally amorphous as the network density and connectivity of these materials can be different. This effect is illustrated from the

comparison of elastic modulus and indentation hardness values of the present materials with those reported by Shah *et al.* for a fully dense amorphous Si-C-N ceramic prepared from the PUMVS precursor using a pressure casting route ($E \approx 156$ GPa; $H \approx 26$ GPa; $T_p = 1000^\circ\text{C}$; heating rate: 25 K/h; holding time: 9 h;) [02Sha]. Nevertheless, investigations using the present materials facilitate to understand the structure-property correlations of typical Si-C-N PDC with respect to their mechanical behavior. A more detailed mechanical characterization of the above materials covering the elastic-plastic deformation and fracture behavior will be presented in the subsequent chapters.

2.5. Conclusions

- (i) Fully dense precursor derived Si-C-N ceramic specimens were fabricated by thermal crosslinking and controlled thermolysis of the PUMVS precursor. Three critical problems were identified and addressed: (a) bubble formation during crosslinking (b) internal gas pressure induced stress leading to bloating and cracking and (c) stresses from differential transformation due to thermal gradients in the sample. Hydrostatic confinement of the liquid precursor during crosslinking yielded bubble-free glassy green bodies. Pyrolytic stresses were minimized by limiting the green body thickness to 1 mm and by moderating the conductive heat transfer to the sample during thermolysis through a proper choice of the heat transfer media, to produce defect-free dense ceramic bodies.
- (ii) The range of selected thermolysis treatments enabled the synthesis of ceramic specimens covering material structures from partly organic amorphous to inorganic nano-crystalline states. Structural variation in the amorphous specimens was realized through the stripping of hydrogen with increasing thermal treatment, leading to materials with progressively densified network structures. Phase separated ceramic

specimens were obtained from still higher thermolysis treatments. The elimination of hydrogen ensued phase segregation in the material, via the organization of the excess free carbon into a turbostratic graphite phase at 1200°C and the nucleation of nano-crystalline SiC at 1300°C thermolysis treatment.

The measured physical and mechanical properties displayed dependency on the material structure. Elastic properties and hardness improved along with the increase in the network density until the onset of phase segregation, where plastic deformation was promoted by the turbostratic graphite phase. Thus, the synthesized specimens are suitable for a detailed mechanical characterization of typical precursor-derived Si-C-N ceramics.

3. Fracture toughness evaluation of precursor derived Si-C-N ceramics using the crack opening displacement approach

3.1. Introduction

Despite the versatile processing capabilities and interesting material properties, the application of precursor-derived silicon based non-oxide ceramics (PDC) as structural materials is limited by their inherent brittleness and flaw-sensitivity. This arises by virtue of their material structure consisting of a predominantly covalent bonded network, which is “non-forgiving” under critical mechanical loading, as compared to the metallic bonded materials. This limitation is however effectively handled by the elimination of the stress raising flaws by controlling surface and microstructure (e.g., in Si-C [78Yaj] and Si-B-C-N [99Bal] fibers) and by suitable microstructural design, employing reinforcing elements (e.g., fiber, particulate and more recently, carbon nanotube reinforced PDC matrix composites [04Lee, 06Kat]). The latter additionally enables the fabrication of sufficiently large structural components for practical applications, from the processing standpoint. In either case, the requirement for an accurate and reliable evaluation of the fracture mechanical properties of the PDC *per se* is obvious. The critical stress intensity factor under mode-I loading (K_{IC}) commonly known as fracture toughness, is the key material property in this regard that characterizes the fracture mechanical behavior and hence, its determination is pivotal in such an evaluation.

Several methods are available for accessing the fracture toughness of materials. They all in general involve the application of a mechanical load to a test specimen of suitable geometry and containing a starter flaw, while monitoring the dimensions of the crack that initiates and propagates from this flaw. The characteristic parameters that are measured in any typical fracture toughness testing method are the applied load (P), the crack length (a) and the displacement (e.g., load point displacement; crack mouth opening displacement, CMOD; crack

tip opening displacement, CTOD or simply COD;). The toughness in principle can be determined from the simultaneous measurement of any two of the above three parameters, combined with the knowledge of the loading configuration and specimen geometry. In practice however, many of the available techniques are either unsuitable or difficult to apply for the characterization of the intrinsic fracture mechanical properties of PDC, mainly due to the limitations in the fabrication of suitable test specimens with respect to size and geometry and / or difficulties in the measurement of the above parameters, particularly for small specimens. Consequently, the literature reports on the toughness evaluation of PDC are scarce and include the work of Nishimura *et al.* (Si-C-N ceramics from powder route; Indentation crack length method) [98Nis], Gonon *et al.* (Si-C-N ceramics from powder route; SENB method) [95Gon], Moraes and Interrante (Si-C ceramics from powder route; SENB method) [03Mor] and Rouxel *et al.* (Si-O-C ceramics from gel casting; SENB method) [01Rou]. Toughness estimates from powder-derived samples represent the engineering toughness values of the respective materials, and are dominated by the effect of the pseudo- microstructure arising from the processing, overshadowing the intrinsic toughness of the basic material. Also, it is now realized that the precursor-derived amorphous ceramics display anomalous character with respect to the deformation behavior beneath the indenter [02Wal, 04Bur]. The non-volume conserving densification mode of plastic deformation in these materials leads to a relatively lower magnitude of residual stresses than that expected from a volume conserving shear deformation [04Bur]. This residual stress field constitutes the principal driving force for the formation of radial and median cracks during the indentation unloading. Thus, the routinely used indentation crack length (ICL) method cannot be readily applied for PDC, due to the unavailability of the appropriate calibration parameters that truly quantify the attendant residual stress field.

In this work the above problems are addressed in two folds: (i) fully dense PDC devoid of any process-introduced microstructural features are used in the

investigations such that the propagating crack does not “see” any microstructural feature uncharacteristic of the basic material (ii) the crack opening displacement (COD) approach is employed for the evaluation of the fracture toughness, which obviates the requirement of any calibration parameter. This method, originally introduced by Rödél [90Röd, 97Sei] offers a simple yet reliable means to evaluate the fracture toughness of the subject materials. In its simplest form, the method involves the measurement of the COD profile of a mode-I crack that is in equilibrium with the applied load, and relating this displacement profile to the mode-I stress intensity factor acting on the crack. The atomic force microscopy (AFM) is employed for measuring the COD in this work, which offers practical advantages as compared to the other competent experimental tools e.g., SEM in terms of sample preparation, handling, measurement accuracy and resolution. Accordingly, this paper describes the evaluation of the fracture toughness of precursor derived Si-C-N ceramics with material structures ranging from fully amorphous to nano-crystalline microstructure, using the above approach.

3.2. Theoretical background

A schematic of the Irwin slit crack and the associated stress field is depicted in Fig. 3.1. From the Irwin near-tip solutions [58lrw] for mode-I loading, the equation for displacement along the loading direction at any point **P** in radial coordinates $\mathbf{P}(r, \theta)$ reads as:

$$u_y = \frac{K_I}{2E} \left\{ \frac{r}{2\pi} \right\}^{1/2} (1 + \nu) [(2\kappa + 1)\sin(\theta/2) - \sin(3\theta/2)] \quad (3.1)$$

where $\kappa = (3 - 4\nu)$ for plane strain conditions; K_I is the mode-I stress intensity factor, E is the Young's modulus, ν is the Poisson's ratio and u_y is the displacement at point **P** in the loading direction. The equation for the mode-I near-tip half crack opening displacement ($u_{near-tip}$) is derived from Eq. 3.1 by setting $\theta = \pm 180^\circ$, $r = X$, yielding the parabolic relationship [58lrw, 93Law]:

$$u_{near-tip} = \frac{K_I}{E'} \sqrt{\frac{8X}{\pi}} \quad (3.2)$$

in the limit ($X \ll a$) where $X = a - x$ is the crack interface coordinate (in other words, the distance from the crack tip); a is the crack length; x is the coordinate location where the displacement is measured; $E' = E / (1 - \nu^2)$ is the plane strain Young's modulus. By measuring the near-tip COD profile of a critically loaded crack (see section 3.3), the crack tip fracture toughness K_{I0} can be estimated using the above equation as $K_{I0} = K_I$, regardless of the crack and specimen geometry.

However, the condition ($X \ll a$) limits [02Fet, 03Kou] the range of COD data that can be used for the estimation of the K_{I0} , as the influence of the crack and specimen

geometry, possible shielding and residual stresses in modifying the COD profile become more pronounced at large X . An improved procedure for the evaluation of the overall COD profile for K_{I0} estimation, that takes into account the above factors has been recently reported by Kounga *et al.* [03Kou, 04Kou] and Fett *et al.* [05Fet], which is based on the COD relation of Rice [72Ric] in integral form:

$$\begin{aligned} u_{total}(x) &= \frac{1}{E'} \int_x^a K_{tip}(a') h(a', x) da' = \frac{K_{I0}}{E'} \int_x^a h(a', x) da' + \sum_{n=1}^{\infty} \frac{A_n}{E'} \int_x^a (a - a')^n h(a', x) da' \\ &\cong \frac{K_{I0}}{E'} \int_x^a h(a', x) da', \quad a - x \rightarrow 0 \end{aligned} \quad (3.3)$$

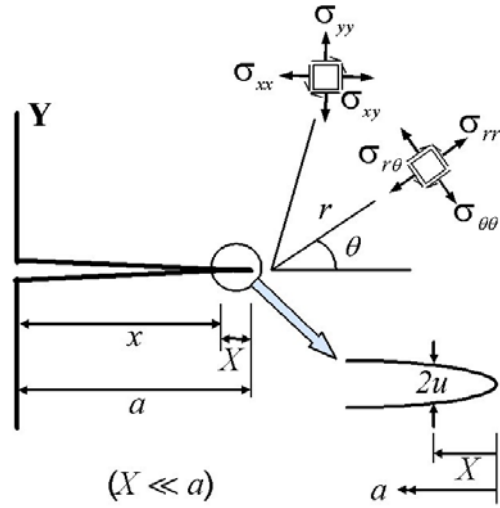


Fig. 3.1. Near-tip stress field for an Irwin slit crack. The geometrical parameters of the mode-I loaded crack-tip are also indicated.

The exhaustive application of this procedure requires the choice of a standard crack and specimen geometries, which in combination decide the appropriate weight function $h(a', x)$. It has been shown [04Kou] that the first term of the above equation coincides with the Irwin parabolic relation for $(X \rightarrow 0)$, although being an approximation. A better approximation of the near-tip behavior is obtained by considering additional terms of the weight function, which results in the general description of the COD profile as:

$$u_{total}(x) \cong \frac{K_{I0}}{E'} \sqrt{\frac{8X}{\pi}} + B_1 X^{3/2} + B_2 X^{5/2} + \dots \quad (3.4)$$

A phenomenological fitting of the measured COD data from radial indentation cracks has been applied using the above equation to estimate the crack-tip fracture toughness (K_{I0}) of soda lime and borosilicate glasses [04Bura]. In such cases, the utility particularly lies in obviating the difficulty of choosing the data range amenable to the Irwin parabolic relation.

3.3. Experimental procedure

Fully dense monolithic Si-C-N ceramics were prepared from the liquid poly(ureamethylvinyl)silazane precursor through a casting route. Details of the materials processing are described in Chapter 2 [07Jan]. In brief, The process involves the thermal crosslinking of the liquid precursor cast and sealed in PTFE molds, followed by pyrolysis of the obtained pore-free transparent green bodies in flowing argon atmosphere between 800 and 1300°C. Above 1100°C, samples were prepared using a two stage pyrolysis-annealing procedure. The samples are denoted here, code-named according to their thermal treatment, e.g., SiCN-080001, SiCN-090001, SiCN-100001, SiCN-110001, SiCN-120012 and SiCN-130012, the first four digits denoting the temperature and the last two digits, the holding time of the pyrolysis / annealing treatment. The resultant ceramic bodies were subsequently ground and polished in the form of thin ($200 \leq w \leq 400 \mu\text{m}$, w = specimen thickness) rectangular plates with dimensions

8×4 mm, with the final surface finishing performed with a 0.25 μm diamond suspension.

Pre-cracking of the samples was achieved using Knoop indentation, located at the mid-point of the long edge on the polished side of the samples (Fig. 3.2). Applied indentation loads varied between 19.62 N for SiCN-080001 to around 58.86 N for the SiCN-120012 and SiCN-130012 samples. A through-thickness crack was subsequently grown from the starter crack by applying a mode-I displacement across the same using a specially made fixture (Fig. 3.3). Towards this, the sample was slide-fitted and glued into the slot provided in the fixture, with the starter crack located on the mid-line between the fixture arms. Loading

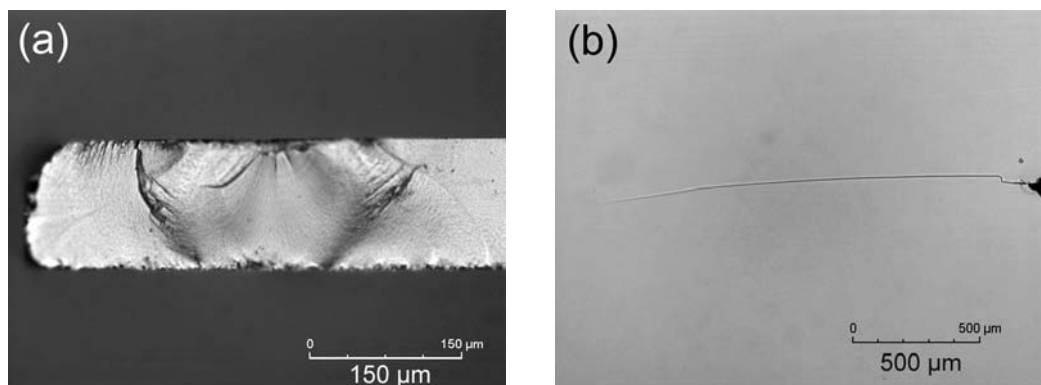


Fig. 3.2. Light micrographs of the starter crack and whole crack in SiCN-130012 specimen. (a) cross sectional view of the starter crack produced by Knoop indentation (b) whole crack grown by application of the displacement controlled loading; crack length ≈ 1.9 mm.

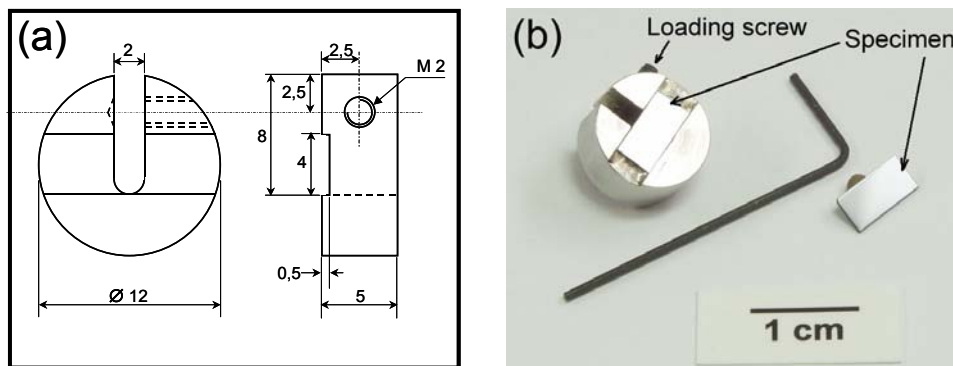


Fig. 3.3. Line diagram (a) and photograph (b) of the loading fixture used to apply displacement controlled loading to the specimen. The photograph also depicts the specimen slide-fitted and glued in the slot provided.

was accomplished by tightening of the screw that opens the fixture arms. Crack propagation during loading was monitored under a low power light microscope. Stable crack propagation was achieved, as the loading was displacement-controlled ($dK_I / da \leq 0$). The loading was stopped as soon as a crack length of around 2 to 2.5 mm was obtained. At this point, the crack is critically loaded to the verge of further growth, where the crack-tip stress intensity factor equals the crack-tip fracture toughness (K_{I0}) of the sample.

The near-tip COD ($2u_{near-tip}$) of this crack, in static equilibrium with the applied load, was measured at progressively increasing distance from the crack tip (crack interface coordinate, X) up to 200 μm from the tip, using AFM (model Nanoscope IIIa, Digital Instruments, Veeco Metrology Group, Santa Barbara) in tapping mode. The measurement range was covered with a series of individual scans of the crack topography, with a scan size of $3 \times 3 \mu\text{m}$ up to a crack length of 50 μm from the tip and thereafter with a scan size of $5 \times 5 \mu\text{m}$ till 200 μm . Super cone probe tips were used in cases where magnitude of COD was small. In other cases a regular Silicon probe was used. A scan rate of 1 to 1.5 Hz was employed. The crack length data was obtained by the sequential overlapping of the scanned images, while the COD across the crack were determined by the section analysis procedure (Fig. 3.4). COD was measured across at least three

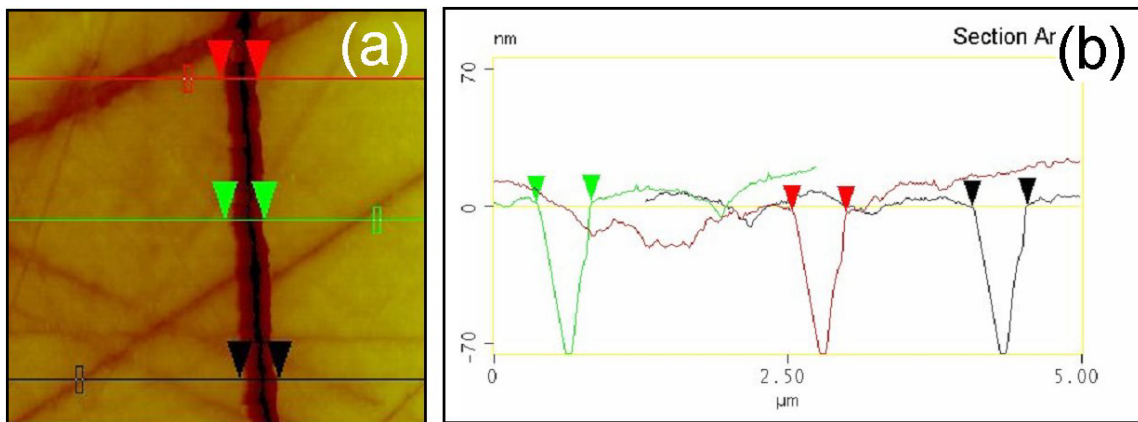


Fig. 3.4. Example of the section analysis using AFM image processing software; (a) Topographic image of a crack segment; (b) the corresponding surface profile trace that enables locating the crack edges.

locations from each AFM image in order to realize a smooth COD profile. For each sample, two COD profile measurements were carried out to ensure the reliability of the data. As a means to cross-verify the validity of the crack loading procedure, COD profiles were additionally measured from the radial indentation cracks in samples SiCN-120012 and SiCN-130012. Vickers indentation with the applied loads P of 98.1 N and 137.3 N was employed to obtain the cracks. In the following text, distinction is made between “indentation cracks” derived from Vickers indentation and “long cracks” derived from fixture loading. To study the morphology of the crack propagation, AFM imaging of the Si-C-N fracture surfaces freshly created using either fixture loading or indentation as described above was performed under topographic, phase and frictional contrasts using tapping and contact (lateral force) mode AFM. As a stable crack propagation was achieved for the entire crack length, the whole fracture surface can be viewed as the mirror region. However the AFM imaging was mainly performed close to the crack tip region, roughly 100-200 μm behind the crack front. Fracture surfaces of the SiCN-120012 and SiCN-130012 samples were additionally examined using high-resolution SEM (HRSEM, Model Zeiss DSM 982 Gemini).

3.4. Results

3.4.1. COD profiles

The measured near-tip COD data from the long cracks in the six samples are plotted in [Fig. 3.5\(a\)](#) and [Fig. 3.5\(b\)](#). Repeated measurements confirmed that the COD profiles are reproducible. That the measured COD data are free from the effect of sub-critical crack growth was ascertained from the observation of the crack tip before and after the COD measurement. The overall shapes of the COD profiles were parabolic in the measured range of crack interface coordinate X , although some noticeable shape deviations and data scatter were present. The scatter in the COD data arises from the uncertainty in locating the crack edges, due to the finite radius of the AFM probe tip, ranging between 5 to 10 nm for the super-cone tips and 10 to 20 nm for the standard Silicon tips. The crack tip

toughness K_{I0} was evaluated from the curve fitting of the COD data according to Eq. 3.2. The correlation coefficients of the curve fits for the overall COD data ranged from 0.95 to 0.99 (Table 3.1) confirming the good agreement of the COD data to Eq. 3.2. The resultant fits are included in Fig. 3.5(a) and Fig. 3.5(b) as solid curves. In order to quantify the variation in K_{I0} due to profile shape deviations, curve fitting of the COD data (from Fig. 3.5(a)) was performed up to various final values of X , by incrementally including (X, u_y) data farther from the crack tip. Additionally, K_{I0} was also evaluated for each individual point (X, u_y) by inverting the Eq. 3.2. The results from the above are collectively plotted in Fig. 3.5(c) as half-filled symbols and unfilled symbols respectively. While the large scatter in the K_{I0} values for $X \leq 20 \mu\text{m}$ can be expected from the fewer data points considered, the overall variation in K_{I0} was negligible in samples SiCN-100001, SiCN-110001 and SiCN-130012. Significant variation in K_{I0}

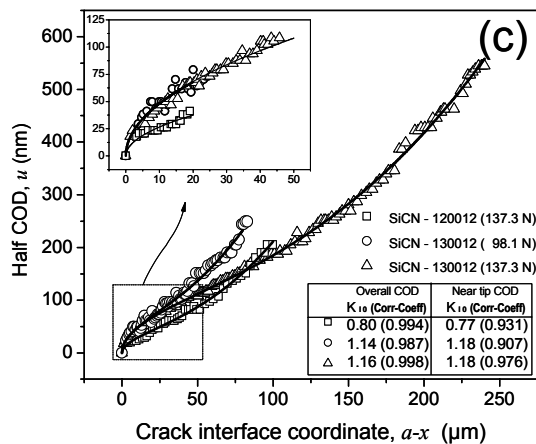
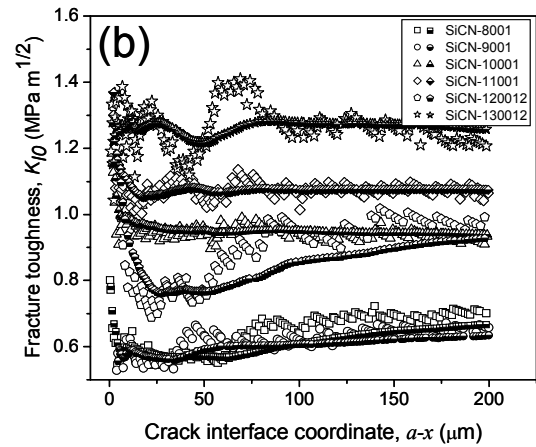
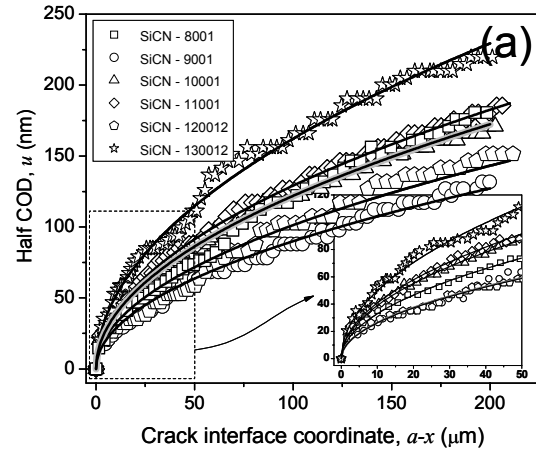


Fig. 3.5. (a) Near-tip COD data and curve fits (solid lines) from long cracks, from two individual sets of measurements (b) crack tip toughness K_{I0} derived from curve fits as a function of maximum fitting range X_{max} (half-filled symbols) and from point-wise evaluation of the COD data using Eq. 2 (unfilled symbols) (c) COD data from indentation cracks in SiCN-120012 and SiCN-130012; results of the curve fits (solid lines) of the overall and near-tip CODs are included in the inset table.

was observed in samples SiCN-080001, SiCN-090001 and SiCN-120012 due to the increase in the measured values of COD at $X > 50 \mu\text{m}$. Similar trends as above were observed from the consideration of COD data from repeated measurements (Fig. 3.5(c)). For further analysis, K_{I0} estimates from two sets of curve fits – one up to $X_{max} = 200 \mu\text{m}$ and the other, up to $X_{max} = 50 \mu\text{m}$ – were used. The data range and the curve fits of the latter are depicted as insets in Fig. 3.5(a) and Fig. 3.5(b).

3.4.2. K_{I0} and G_I estimates

The crack tip toughness of materials SiCN-080001 through SiCN130012 evaluated from the measured COD profiles as above are presented in Table 3.1, along with the values of elastic modulus E and Poisson's ratio ν of the respective materials, determined from resonance frequency testing (Chapter 2 [07Jan]). K_{I0} was found to increase in samples from increasing thermal treatment, from $0.6 \text{ MPa m}^{1/2}$ in SiCN-800001 to $1.1 \text{ MPa m}^{1/2}$ in SiCN-110001. Noteworthy here is the concurrent increase in the elastic modulus of the samples, from 82 GPa to 127 GPa. In SiCN-120012 however, the toughness dropped to $0.9 \text{ MPa m}^{1/2}$, in spite of a further increase in E to 140 GPa. K_{I0} increased to $1.2 \text{ MPa m}^{1/2}$ in SiCN-130012 while the associated modulus was 117 GPa.

Given the background of the profile shape deviations (section 3.4.1), K_{I0} estimates from two individual COD measurements compared reasonably well with each other, as indicated by the low standard deviation between the two

Table 3.1. Summary of K_{I0} and G estimates from the curve fitting procedure; values of elastic modulus E and Poisson's ratio ν of the sample materials are also included from Chapter 2. [07Jan].

Sample	Youngs modulus (GPa)	Poissons ratio	$(a-x)_{max} = 200\mu\text{m}$					$(a-x)_{max} = 50\mu\text{m}$				
			K_{I0} (MPa m ^{1/2})	Standard Deviation [K _{I0}]	Correlation Coeff. [K _{I0}]	G_{I0} (J/m ²)	Standard Deviation [G _{I0}]	K_{I0} (MPa m ^{1/2})	Standard Deviation [K _{I0}]	Correlation Coeff. [K _{I0}]	G_{I0} (J/m ²)	Standard Deviation [G _{I0}]
SiCN-080001	82 ± 1	0.245 ± 0.015	0.64	0.04	0.97	4.67	0.59	0.56	0.01	0.99	3.64	0.13
SiCN-090001	106 ± 1	0.24 ± 0.005	0.65	0.03	0.98	3.79	0.31	0.57	0.02	0.97	2.92	0.25
SiCN-100001	117 ± 1	0.22 ± 0.003	0.93	0.01	0.99	7	0.22	0.88	0.1	0.99	6.37	1.37
SiCN-110001	127 ± 1	0.21 ± 0.005	1.14	0.09	0.99	9.75	1.48	1.1	0.02	0.99	8.98	0.36
SiCN-120012	140 ± 4	0.22 ± 0.01	0.92	0.01	0.96	5.79	0.19	0.72	0.05	0.96	3.64	0.49
SiCN-130012	117 ± 4	0.23 ± 0.01	1.3	0.06	0.99	13.75	1.34	1.23	0.01	0.95	12.2	0.28

measurements (Table 3.1). However, the K_{I0} estimates from the data fitting range at $X_{max} = 200 \mu\text{m}$ tend to be higher than those from the fits at $X_{max} = 50 \mu\text{m}$ by a magnitude of approximately $0.1 \text{ MPa m}^{1/2}$. This is significant, in comparison to the variations characterizing the crack tip toughness behavior of the investigated materials. The difference between the two fits in the case of SiCN-120012 is remarkably high at $0.2 \text{ MPa m}^{1/2}$, with the K_{I0} estimate at $X_{max} = 50 \mu\text{m}$ being $0.7 - 0.75 \text{ MPa m}^{1/2}$. In light of the above, it was necessary to ascertain the cogency of the observed crack tip toughness behavior, particularly of SiCN-120012 and SiCN-130012. This was served by the indentation COD measurements. Accordingly, the measured COD profiles of indentation cracks in SiCN-120012 (one profile with $P = 98.1 \text{ N}$) and SiCN-130012 (2 profiles with

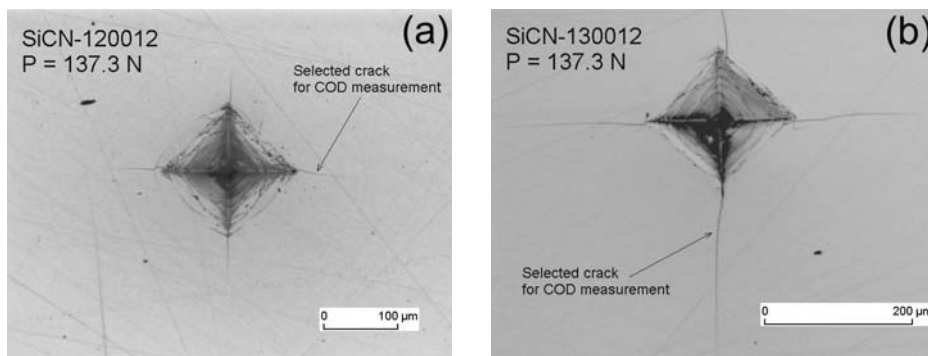


Fig. 3.6. Light micrographs of Vickers indents with the radial crack system from (a) SiCN-120012 and (b) SiCN-130012 samples.

$P = 98.1 \text{ N}$ and 137.3 N) are plotted in Fig. 3.5(d). Micrographs of the Vickers indents and crack systems in SiCN-120012 and SiCN-130012 obtained at the applied load of 137.3 N are shown in Fig. 3.6. K_{I0} of the materials were estimated both from the overall COD data and the near-tip COD data (inset in Fig. 3.5(d)) via curve fitting according to Eq. 3.4 and Eq. 3.2 respectively. The estimates, which are included in Fig. 3.5(d) as a table, agree well with K_{I0} estimates from long cracks at $X_{max} = 50 \mu\text{m}$.

To understand the energetics of the fracture behavior, the strain energy release rates G_{I0} were calculated from the corresponding K_{I0} values using the relation

$G = K^2 / E'$ and are presented in [Table 3.1](#). G_{I0} follows the same trend as K_{I0} with increasing pyrolysis temperature, but the variations are much more pronounced, attributable to the changes in the fracture surface energy in the materials as will be discussed further in [section 3.5](#).

3.4.3. Morphology of crack propagation

Microstructural toughening contributions from potential geometrical (effected by transitory obstacles to crack propagation) and shielding processes [[93Law](#)] can be discerned from the morphology of crack propagation. Towards this purpose, AFM images of the crack tips in samples SiCN-080001, SiCN-100001, SiCN-120012 and SiCN-130012 are shown in [Fig. 3.7\(a-d\)](#). Cracks in

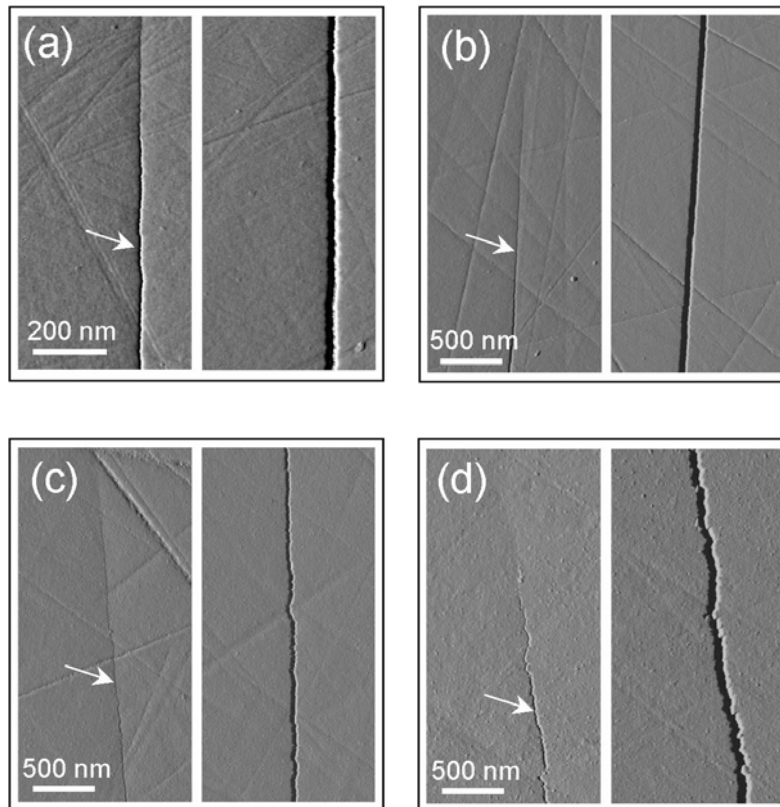


Fig. 3.7. Morphology of crack propagation in amorphous and phase segregated Si-C-N samples: (a) SiCN-080001 (b) SiCN-110001 (c) SiCN-120012 and (d) SiCN-130012. Left side images show the crack tips (indicated by arrows); right side images are crack segments from locations at approx. $15 \mu\text{m}$ ($4 \mu\text{m}$ in (a)) from the crack tip; AFM images in tapping mode, amplitude contrast.

SiCN-120012 and SiCN-130012 show a serrated appearance, with pronounced crack deflection observed in the latter. From structural and microstructural analysis (Chapter 2) [07Jan], these two samples are known possess a phase segregated microstructure. Interestingly, the cracks in electron-amorphous materials SiCN-080001 and SiCN-100001 (see Chapter 2, section 3.2.5) [07Jan] also exhibit crack deflection, although to a smaller magnitude. A higher magnification is employed in Fig. 3.7(a) to visualize the deflection. AFM images (Fig. 3.8) of the corresponding fracture surfaces serve to probe the extent of crack deflection and the causative microstructural elements. The progressive increase in crack deflection in samples from higher thermal treatment is evident

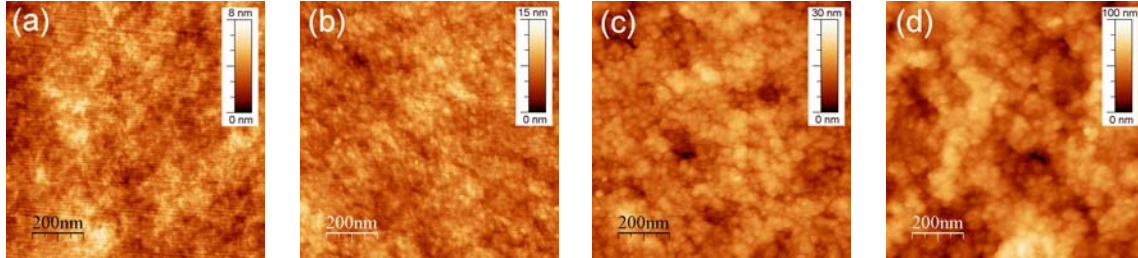


Fig. 3.8. Fracture surface morphology in amorphous and phase segregated Si-C-N samples: (a-d): tapping mode AFM topographic images of samples SiCN-080001, SiCN-100001, SiCN-120012 and SiCN-130012 respectively.

from the representative topographic (height) images of the fracture surfaces, Fig. 3.8(a-d). This is further quantified in terms of the root-mean-square roughness (RMS roughness, R_q) values and the ratios $\alpha = \text{actual} / \text{projected}$ fracture surface area (referred to the scan area of $1 \times 1 \mu\text{m}^2$), extracted from the above images and summarized in Table 3.2. The height images also depict topographic features with a lateral dimension of 10-30 nm and heights comparable to the R_q values in respective samples. A detailed examination using AFM probes with different tip radii however showed that the surface contour of these

Table 3.2. RMS roughness and the ratio $\alpha = \text{actual} / \text{projected}$ fracture surface area extracted from the $1 \times 1 \mu\text{m}^2$ AFM topographic images of the fracture surfaces in amorphous and phase segregated samples.

Roughness parameter	SiCN-080001	SiCN-100001	SiCN-120012	SiCN-130012
RMS roughness (nm)	0.97	1.42	3.12	12.77
Actual Fr. area / Proj. Fr. Area	1.0301	1.0353	1.05	1.2451

apparently granular features is significantly influenced by the effect of the tip convolution and dilation of the real topographic features at these locations. Thus, while the fracture surface topography is captured fairly well in the AFM height images, a one-to-one correspondence to the true surface is masked at the nano-scale level, due to the above effects. As the length scale of the measured crack deflection amplitudes, topographic feature dimensions and RMS roughness lies in the nanometer regime, the fracture surface roughness of the present Si-C-N materials can be appropriately termed ‘nanoscale roughness’.

3.4.4. Material contrast imaging

The fracture surfaces were further examined under tapping mode phase contrast as well as lateral force (contact) mode frictional contrast imaging in an attempt to identify the microstructural features from the physically or compositionally distinct phases that are involved in the fracture process. The sensitivity of the phase contrast imaging is derived from the differential attractive and repulsive tip-sample interactions in the tapping mode operation. Such interactions include elastic, viscoelastic, adhesion and friction, and are described using Hertzian, JKR, DMT and Maugis contact models [97Bur]. During tip-sample engagement, the cantilever response frequency experiences a phase shift from its free-air phase angle, which is negative for attractive and positive for repulsive interactions (according to the DI convention). It has been shown that genuine phase contrast reflecting material properties is obtained only with energy dissipative interactions e.g., viscoelasticity and adhesion hysteresis [98Gar]. Apparently strong phase shifts are also frequently observed when the phase imaging is carried out in a bi-stable tapping regime. Operation in either mono-stable or bi-stable regime is determined by the magnitude of the tapping force in relation to the attractive and repulsive forces. A mono-stable regime is characterized by the predominance of either attractive (soft tapping; $0.7 < \text{set-point amplitude } (A_{sp}) / \text{free-air amplitude } (A_0) \leq 0.9$) or repulsive interaction (hard tapping; $0.2 \leq A_{sp}/A_0 \leq 0.6$), whereas the bi-stable regime results

from the switching between attractive and repulsive interactions, strongly influenced by topography of the sample surface [01Jam]. Transient phase shifts of topographic origin can also arise due to the finite response time of the feedback system in restoring the set-point amplitude.

In the present study, phase imaging was carried out in ambient atmosphere with a range of tapping amplitudes varying from soft to hard tapping ($0.5 \leq A_{sp}/A_0 \leq 0.8$). In all fracture surfaces, the soft, moderate and hard tapping conditions yielded phase images corresponding to mono-stable attractive (arising from adsorbed moisture), bi-stable and mono-stable repulsive (arising from elastic response of the hard ceramic surface) interactions, respectively. The phase images obtained at identical measurement conditions and with $A_{sp}/A_0 = 0.5$ are shown in Fig. 3.9(a-d) and correspond to the height images presented in Fig. 3.8(a-d). In comparison to the height images, the phase images delineate finer details of crack deflection in enhanced contrast. A one-to-one correlation was observed between the topography and the phase shifts in SiCN-080001 and

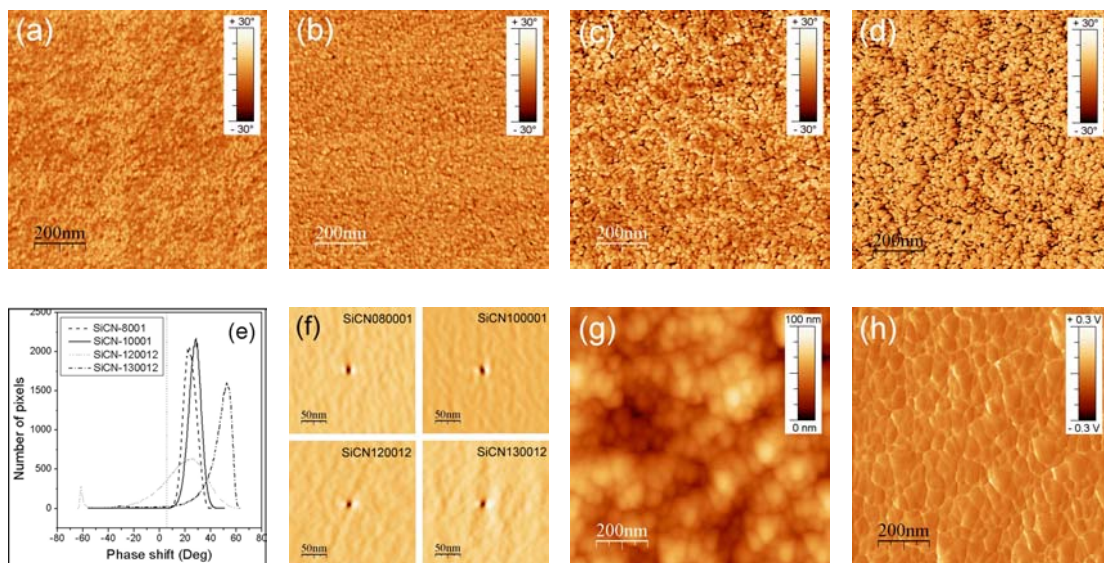


Fig. 3.9. TM-AFM phase contrast images of fracture surfaces in amorphous and phase segregated Si-C-N samples: (a) SiCN-080001 (b) SiCN-100001 (c) SiCN-120012 and (d) SiCN-130012. The images correspond to the topographic images presented in Fig. 3.8.(e) Phase shift distribution (f) Cross-correlation of the phase images with the second derivative of the corresponding height images. Also presented are the LFM topographic (g) and frictional contrast (h) images of the SiCN-130012 sample fracture surface.

SiCN-100001 samples *viz.*, hills and valleys were rendered in the phase images as bright (positive shift) and dark (negative shift) contrasts respectively. While a predominantly positive phase shift was observed in SiCN-120012 and SiCN-130012 samples, locations of surface crevices and pockets were highlighted as dark boundaries, surrounding the brighter grain-like features. Examination of these locations at higher magnification displayed a small elevation in the topography of corresponding shape, signifying a transient switching of the tapping into the non-contact regime, where attractive interaction is prevalent. In all the four samples, the phase images were anti-correlated (Fig. 3.9(f)) with the Laplacian of the corresponding height images, pointing to the association of the positive curvatures at the surface crevices with the negative phase shifts. A plot of the overall absolute phase shift distribution, extracted from the phase images Fig. 3.9(a-d) is shown in Fig. 3.9(e). Here, an increase in the average of the phase shift distribution is attributable to the overall increase in the repulsive interaction, whereas the variation about this average value arises from the surface topography. In spite of the apparent agreement with the former case in fig. 3.9(e), no consistent behavior to the effect was observed at other A_{sp}/A_0 values, suggesting that the phase shift variations were predominantly of topographic origin. In summary, the phase imaging in the present study did not resolve microstructural features assignable to material contrast. This result radically differs from the observation of Rouxel *et al.* [01Rou], where a negative phase shift in the phase image of a Si-C-O glass scratch surface was ascribed to regions of phase segregated graphite, with lateral dimensions of the order of several hundred nanometers. While an enhanced phase segregation and crystallization can be expected in Si-C-O based materials as compared to Si-C-N materials, lack of information in Ref. [01Rou] with regards to AFM operation conditions and sample topography limits a reasonable comparison of the two contrasting results.

The lack of material contrast was also reflected in the frictional contrast image (Fig. 3.9(h)) of the SiCN-130012 fracture surface. The features in the image

merely replicate the topographic details (Fig. 3.9(g)), with a poorer lateral resolution than the tapping mode images. HRSEM micrographs of the SiCN-120012 and SiCN-130012 fracture surfaces in secondary electron mode

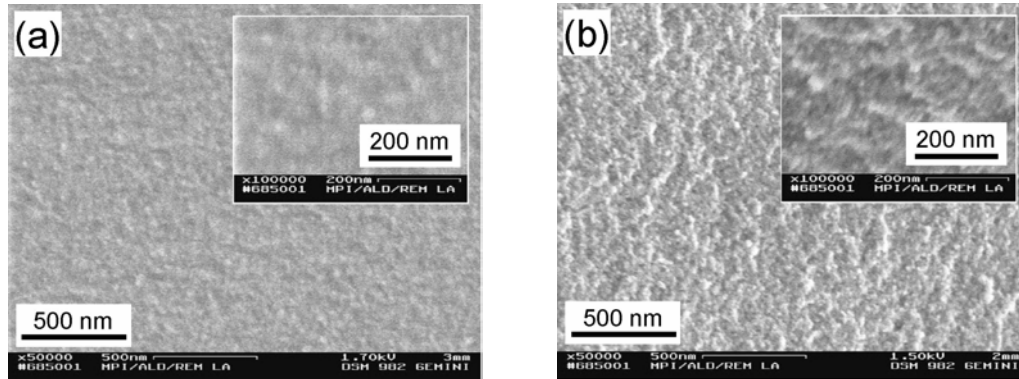


Fig. 3.10. HRSEM micrographs of the fracture surfaces in phase segregated Si-C-N samples; (a) SiCN-120012; (b) SiCN-130012. Higher roughness in (b) as compared to (a) is apparent. Closer examination also reveals the surface fine structure.

(Fig. 3.10(a, b)) support the AFM topographic observations. However, the potential chemical heterogeneities could not be detected from the back-scattering images of the fracture surfaces, due to the negligible variation in the atomic numbers and the insufficient electrical conductivity of the samples.

3.5. Discussion

Inspection of the typical cracks grown through the Si-C-N ceramic specimens (viz., light micrographs, Fig.3.2) indicates that the crack propagation is unaffected by any processing generated macro / microstructural features and thus, affirming that the fully dense specimens capture the true intrinsic fracture behavior of the investigated materials. Due to experimental limitations, the specimen geometry does not conform to any standard fracture test geometry, necessitating the crack tip toughness K_{I0} to be derived from the near tip COD data. However, considering the geometry of the actual specimen, calculated COD profiles according to the SENB geometry [91Fet] with equivalent dimensions agreed with the Irwin parabolic equation (with a correlation coefficient of 0.997) for $X \leq 500 \mu\text{m}$, validating the use of the presently measured near tip COD data, up to

$X \leq 200 \mu\text{m}$. The correlation coefficients of the curve fits using the measured COD data indeed show good agreement (Table 3.1) to this effect. The apparently increasing K_{I0} for larger X (Fig. 3.5(c)), especially in SiCN-080001, SiCN-090001 and SiCN-120012 specimens that display relatively narrow COD profiles (Fig. 3.5(a)), is attributable to the reduction in the crack image resolution due to the change of scan size from $3 \times 3 \mu\text{m}$ to $5 \times 5 \mu\text{m}$. This proposition is supported by the absence of any sub-critical crack growth in the investigated materials.

The measured crack tip toughness of the present Si-C-N ceramic materials for $50 \mu\text{m} \leq X \leq 200 \mu\text{m}$ range from 0.55 to 1.3 $\text{MPa m}^{1/2}$. These values are appreciably lower than the engineering toughness values reported by Nishimura [98Nis] (2.1 $\text{MPa m}^{1/2}$) and Gonon [95Gon] (3.3 to 4.3 $\text{MPa m}^{1/2}$) for the powder-derived Si-C-N ceramics, wherein the processing introduced microstructure dominates the fracture response. In contrast, our measurements reflect the intrinsic fracture response of the respective base materials, depending only on the degree of ceramization. K_{I0} increases in materials from increasing thermolysis treatment with the exception of SiCN-120012, which finds a minimum in K_{I0} at $\sim 0.75 \text{MPa m}^{1/2}$. The variation is effected by the changes in the fracture energy and the operative crack front – microstructure interactions, ultimately controlled by the material structure. A detailed structural characterization of the presently investigated materials is presented in Chapter 2 [07Jan]. In order to appreciate the correlation between material structure and the fracture behavior, it is worthwhile to restate the salient structural features here. Accordingly, the materials SiCN-080001 through SiCN-110001 are essentially electron-amorphous, with the two chief discriminating features among them being (i) a progressive decrease in the hydrogen content leading to an increased structural density and (ii) a progressive organization of sp^2 carbon. Materials SiCN-120012 and SiCN-130012 are phase segregated, with the former containing a turbostratic graphite (TG) phase distributed in an amorphous Si-C-N matrix, while the latter additionally contains nanocrystalline SiC and a more developed TG layer network.

In understanding the influence of the above phase constitution on the crack tip toughness, distinction is made between the contribution of the changes in the fracture surface energy and of the crack tip processes. Pertinent to the crack tip toughness, the latter encompass crack deflection and crack pinning. AFM fractography (Fig. 3.8) reveals a progressive increase in the fracture surface roughness in samples SiCN-080001 through SiCN-130012, the increase in the last two samples being exponential (Table 3.2). Frischat and co-workers [97Räd, 99Wün, 03Pog] and Gupta *et al.* [00Gup] have studied the nanoscale roughness of the oxide glass fracture surfaces using AFM. While the earlier studies [97Räd, 99Wün] related the magnitude of the fracture surface roughness to the crack velocity via the classical mirror-mist-hackle theory, Gupta identified the nanoscale roughness as arising from the crack deflection around the structural and compositional inhomogeneities in the glass structure that provided minimum energy paths for the crack propagation. Small angle X-ray and neutron scattering investigations on precursor derived Si-C-N ceramics have revealed such local short and medium range ordering of $\text{Si}_3(\text{C,N})_4$ and amorphous carbon regions. The size and number density of these regions were found to increase with the degree of ceramization [02Hau]. Indeed, increased RMS roughness and thus an increased crack deflection has been also observed in heavy metal fluoride glasses with annealing treatment, inducing phase separation and crystallization [97Ans]. In light of these investigations, it is evident that the progressive increase of the nanoscale fracture surface roughness observed in the present Si-C-N materials is due to the evolution of structural and compositional inhomogeneities controlled by the phase evolution described above. In a more recent investigation of the fracture surfaces of different glasses using UHV-AFM, direct imaging of the glass network structure was achieved [03Pog]. The results showed an increase in the fracture surface roughness in glasses with higher network connectivity. Boolchand *et al.* have studied the influence of the decrease in the network connectivity due to the presence of one fold coordinated (OFC) atoms in covalent networks [96Boo]. Accordingly, the progressive stripping of hydrogen in higher

thermolyzed Si-C-N ceramics leads to an increased connectivity in the amorphous network. Crack propagation in the amorphous Si-C-N materials thus occurs through the non-bridged regions that are also the weaker regions in the material, in the spirit of Gupta's inference. The measured RMS roughness values (R_q) of the amorphous Si-C-N fracture surfaces (Table 3.2) are significantly higher than those from most of the oxidic glasses ($0.3 \leq R_q \leq 0.8$) [97Räd, 00Gup], suggesting that the weaker regions are more sparsely spaced. The decrease in the volume density of weaker regions should lead to a tortuous crack path. The resultant increase in crack resistance can be visualized either in terms of the increase in the average fracture surface energy or as crack deflection toughening, depending upon the length scale of observation [03Bou, 00Mor]. The discrimination of the relative contribution of each on the toughness increase is however not clear, as the operative fracture mechanisms in amorphous brittle solids are not yet completely understood [04Gui].

The micromechanics of crack propagation are less ambiguous in the phase segregated SiCN-120012 and SiCN-130012 samples. The drop in K_{I0} of the SiCN-120012 in spite of the observed increase in crack deflection indicates that the segregation of the TG phase on its onset is clearly associated with a decrease in the average fracture surface energy. The thermo-elastic residual stress state [93Law] around the graphite precipitates is such that the crack is deflected away from the layer ends while it is attracted to the layer planes. This should force TG interlayer as well as TG – Si-C-N matrix de-bonding (The bonding between graphitic layer and the Si-C-N matrix is expected to be weak.). In effect, the shorter TG precipitates provide low energy fracture paths through the microstructure. The extent of the induced crack deflection at this stage is evidently insufficient to compensate for the decrease in the crack resistance. The more developed TG network combined with the nucleated SiC nano-crystallites effect a pronounced crack deflection in SiCN-130012. The residual stress state prevailing around the TG phase is same as described above; however, the longer curly layers can deflect the crack along a more tortuous path than in

SiCN-120012. The SiC crystallites in contrast should always deflect the crack away through the amorphous phase due to the positive thermo-elastic mismatch *vis-à-vis* the amorphous matrix phase. The attendant increase in the K_{I0} is $\sim 50\%$ ($= 1.2 / 0.8$) in comparison to the SiCN-120012. This is relatively higher than the maximum limit of toughness increment as evaluated by Pezzotti for the deflection-toughened materials [93Pez]. However, it is highlighted here that the limitations with respect to the second phase alignment sighted by Pezzotti is not applicable to the present phase segregated materials, as the TG phase is formed *in-situ*. A comparison of the magnitude of the crack deflection in this sample in juxtaposition with the crack opening profile suggests of possible crack surface interactions up to a length of 5 to 10 μm from the crack tip. However, its influence is seemingly insignificant, as the recorded near tip COD profiles conform to the parabolic shape. The lower bound of the toughness increment from crack deflection is quantified by the increase in fracture surface area. A detailed fracture mechanics treatment additionally includes the cumulative effects of crack tilt and twist that increase with the aspect ratio and the volume fraction of the deflecting elements [93Pez, 83Fab]. For amorphous and nano-structured materials such as the present case, even the estimation of this lower bound – which necessitates a true capture of the actual fracture surface – is limited by the inherent trade-off between the resolution and sweep capabilities of the AFM fractography. Understandably, the presently estimated increase in the surface areas (α , Table 3.2) does not fully account for the K_{I0} variations.

The average crack tip toughness of the present Si-C-N materials is higher than that of oxidic glasses [04Bur]. The increase results from the higher bond strengths and a higher connectivity of the Si-C-N covalent network. This is further illuminated by the experimental [86Sak] and theoretical [05Kroa] investigations on oxynitride glasses, where clear improvements in the mechanical properties with increasing nitrogen content have been realized.

3.6. Conclusions

- (i) Crack opening displacement method was successfully applied for the evaluation of the crack-tip toughness of precursor-derived Si-C-N ceramics. The use of fully dense ceramic specimens allowed characterizing their intrinsic fracture behavior.
- (ii) The measured K_{I0} values ranged from 0.6 to 1.2 MPa m^{1/2} depending upon the structure of the materials that varied from partly organic amorphous to inorganic nanocrystalline states. In amorphous materials, the increase in crack resistance was realized through the progressive stripping of the OFC- hydrogen at higher thermolysis temperatures that increased the network connectivity. Nano-scale crack deflection in these samples reflected the presence of structural and compositional inhomogeneities within the amorphous structure. Low energy fracture paths provided by TG phase segregation controlled the micromechanics of crack propagation in phase separated materials. The net change in crack resistance in these materials was effected by the change in the average fracture surface energy as well as crack deflection toughening.
- (iii) Although the influence of TG phase segregation on the fracture behavior is reflected in the measured K_{I0} values, direct fractographic evidence to this effect could not be recorded using material contrast imaging using AFM. It is proposed that an UHV-AFM analysis of the relevant fracture surfaces would be more illuminating in this regard.

A different approach to the understanding of the fracture of amorphous materials is through the fractal analysis of the fracture surfaces. The method as applied to the present materials is presented in the next chapter.

4. Fracture in precursor-derived Si-C-N ceramics – analysis of crack roughness and damage mechanisms

4.1. Introduction

In the previous chapter, the evaluation of crack tip toughness (K_{I0}) of Si-C-N ceramics synthesized from a polysilazane precursor was presented [07Jana]. The net change in crack resistance in the investigated range of materials was discussed in terms of the phase evolution at various degrees of ceramization. Depending on the pyrolysis temperature during synthesis, the derived Si-C-N materials possess an amorphous structure with an appreciable quantity of bonded hydrogen below 1000°C and convert into nanocrystalline ceramics with the loss of hydrogen at higher annealing temperatures [07Jan]. The observed variations in K_{I0} were identified with the progressive increase in the network connectivity, promoted by the stripping of one-fold coordinated (OFC) hydrogen in amorphous materials, and the formation of turbostratic graphite (TG) and nanocrystalline SiC (n-SiC) in the phase segregated materials (Chapter 3) [07Jana]. Concomitant to the overall increase in K_{I0} a monotonous increase in the root mean square roughness (RMS roughness, R_q) of the fracture surfaces was also recorded, proceeding with the ceramization and phase segregation.

Traditionally, an increase in fracture surface roughness indicating the creation of additional fracture surface is associated with increased fracture toughness. However, a detailed consideration [93Law, 92Röd, 90Dux] of the crack tip processes, microstructure and the energetics of the constituent phases and interfaces reveals that such a generalization would be misleading. Nevertheless, fractographic analysis of fracture surfaces can be usefully applied (i) to identify fracture mechanisms and energy consuming processes e.g., in metals, ceramics and composites [87ASM] and (ii) with necessary additional considerations, towards a quantitative evaluation of the toughening mechanisms [99Dus, 00Dus].

Attempts to the former with respect to amorphous ceramics e.g., silicate glasses however have proved to be non-trivial and are a subject of intense discussion recently [03Cel, 03Cela, 04Gui, 05Gui].

Analysis and quantification of the fracture surface topography with first order roughness parameters such as R_q is inadequate towards understanding the physics of the fracture process, as it does not reflect the spatial correlation of the morphological features contained in the fracture surface. This inadequacy is fulfilled with second order statistical functions such as height-height correlation function (structure function), autocorrelation function and power spectral density (PSD) function [97Fan]. PSD function completely describes the fracture surface, as the height distributions in the fracture surface show Gaussian behavior. A PSD plot in double logarithmic coordinates groups the individual strengths of the fracture surface undulations in inverse length space, enabling analytical comparison and characterization of different fracture surfaces. Extended linear regions in the PSD plot have been shown to signify fractal character of fracture surfaces, associated with a fractal dimension D (or alternatively a roughness exponent ζ) in the respective length scales. Roughness analysis of the fracture surfaces using fractal approach was initiated by Mandelbrot *et al.* [84Man] and has been applied [89Mec, 02Mec, 97Bor, 97Bou, 03Bou] to understand the fundamental physical process of fracture at the crack front or process zone towards establishing correlations to the gross fracture behavior. (Definitions and methods of fractal analysis are presented in the next section.) Mecholsky *et al.* have addressed the problem through the inclusion of D (or precisely, the fractal dimensional increment, D^*) as a sub-parameter within the critical surface energy term, based on experiments and modeling. The experimental data supporting their formulation suggest a positive correlation of D^* with K_{IC} , with an implicit notion that K_{IC} scales with crack tortuosity [89Mec, 02Mec]. Borodich proposed a different formulation for accounting the fractal character of fracture surfaces, where the surface energy term in the Griffith energy balance equation is defined in terms of the “specific energy absorbing capacity of the fractal surface”, which

corresponds to the amount of elastic energy spent on forming a unit of fractal surface area [97Bor]. On the other hand, Bouchaud *et al.* conjectured that the fractal scaling of fracture surfaces from a wide range of materials *e.g.*, glasses, metals and wood displays a *universal* roughness exponent ($\zeta \sim 0.8$), and that the correlation to the fracture properties is reflected in the observed correlation lengths ξ of the fractal regimes in the respective materials [97Bou]. Additionally, depending on the crack velocity, two regimes of damage processes (quasi-static and dynamic) were discussed, exhibiting two universal roughness exponents *viz.*, 0.5 and 0.8 in short and large length scales respectively. The crossover lengths ξ_c between the two regimes were discussed to be both crack velocity and material dependant, the later dependency arising from the size of the heterogeneities in the material structure [03Bou, 97Dag]. Concerning the investigation of the damage mechanisms at the crack-tip / process zone, formation and linkage of damage cavities akin to plastic deformation was proposed, even for nominally brittle materials such as silicate glasses and amorphous ceramics. Further, the roughness exponent within the damage cavities was related to a quasi-static damage process, while that arising from the linkage of cavities was related to a dynamic damage process [03Bou]. This interpretation derived strong motivation from the results of MD simulations of fracture in silica glass and amorphous Si_3N_4 [99Van, 97Kai]. Subsequently, *in-situ* high-resolution AFM imaging of propagating cracks in silicate glasses were presented to support the formation of 'damage cavities' [03Cel, 03Cela].

In light of the above background, it is worthwhile to examine the fractal scaling of roughness in the fracture surfaces of the precursor-derived Si-C-N amorphous and nanocrystalline ceramics possessing a progressively varying material structure in terms of the number and size of the heterogeneities. The objectives of this work are two-fold: (a) examination of the possible correlations of fractal scaling parameters and fracture behavior and (b) examination of the damage mechanisms at the advancing crack front that lead to the fracture surface roughness. Towards the first objective, the roughness analysis of the fracture

surfaces of Si-C-N ceramics is presented, performed using second order statistical functions to evaluate the fractal scaling, relevant length scales of fractal regimes and attendant roughness exponents. These results are then discussed with reference to previously developed understanding of the subject from literature as above to examine possible correlations between fractal scaling and fracture behavior. The second objective is pursued using high-resolution AFM imaging of the crack-tip process zones and crack faces of the critically loaded cracks, where the possibility of the formation of damage cavities is investigated.

4.2. Theoretical background

Fracture surfaces are self-affine objects displaying scale invariance under an affine transformation [97Bor, 97Bou]

$$x' = \lambda x, \quad y' = \lambda y, \quad z' = \lambda^\zeta z \quad (4.1)$$

and are characterized by their non-integer fractal dimensions D , in contrast to Euclidian objects. The fractal dimension of a fractal surface ranges between $2 < D < 3$ and that of the fractal curve, between $1 < D < 2$. To illustrate, if N is the number of balls or cubes with diameter Δ required to cover a fractal object and if the increase in N due to a corresponding decrease in Δ is proportional to Δ^{-D} (i.e., $N \propto \Delta^{-D}$), then the object is said to have a fractal dimension of D (more specifically, the box dimension, D_B) [97Bor]. To enable comparison of the fractal dimensions derived from surfaces and curves, the fractal dimensional increment D^* is defined such that $D = 2 + D^*$ for a fractal surface and $D = 1 + D^*$ for a fractal curve [89Mec, 97Bor, 02Mec]. An increase in fractal dimension is physically manifested as an increased tortuosity of the fracture surface profile trace. Considering the self-affine rather than self-similar scaling that is observed in fracture surfaces (Eq. 4.1), the more appropriate parameter that describes the fractal scaling in fracture surfaces is the roughness exponent ζ (also known as self-affine exponent or Hurst exponent), which varies between 0 and 1 [97Bou].

The roughness exponent ζ and (box) fractal dimension D_B of fracture profile are related to each other as $\zeta = 2 - D_B$ in the limit where the horizontal increment of the fracture profile data is small compared to the typical range of profile heights, i.e., $\delta x \ll |z_{Max} - z_{Min}|$. Thus, a higher fracture profile tortuosity corresponds to a higher D but a lower ζ . Unlike the ideal fractal objects, fractal character of real fracture surfaces is limited to regimes of finite length scales, characterized by their corresponding correlation lengths ξ_i . The fractal dimension D_i or the roughness exponent ζ_i is defined as valid within ξ_i , beyond which either a different fractal regime or the Euclidian plane (flat surface) is realized.

Several methods are described in literature for the evaluation of fractal scaling of fracture surfaces, and include slit island analysis (SIA) [89Mec], variable bandwidth method [95Sch], return probability method [95Sch, 97Bou] and power spectrum method [95Sch, 97Bou, 97Dag]. The analytical procedures and reliability issues of these methods have been extensively reviewed [94Mil, 95Sch]. Generally, the analysis is performed on the fracture profile curves obtained by sectioning of the fracture surface, either along the plane of the surface (as for SIA, yielding island curves) or normal to it (e.g., in power spectrum method). In this work, fractal scaling is evaluated in terms of the roughness exponent ζ from fracture profile curves obtained from vertical sectioning of the fracture surface, using the following relations:

(i) from the variational R_q method [95Sch, 97Kie]:

$$R_q(r) \propto r^\zeta, \quad \zeta = (d \log R_q(r) / d \log r) \quad (4.2)$$

(ii) from the structure function $S(r)$ [97Bou, 03Bou]:

$$S(r) = \langle |h(x+r) - h(x)|^2 \rangle \propto r^{2\zeta}, \quad \zeta = (1/2) * (d \log S(r) / d \log r) \quad (4.3)$$

(iii) from the Hurst method [97Bou, 03Bou]:

$$z_{max}(r) = \left\langle \text{Max}\{z(r')\}_{x < r' < x+r} - \text{Min}\{z(r')\}_{x < r' < x+r} \right\rangle_x \propto r^\zeta,$$

$$\zeta = (d \log z_{max}(r) / d \log r) \quad (4.4)$$

(iv) from the power spectrum $p(f)$ of the fracture profile [97Bou, 97Dag, 95Sch]:

$$p(f) \propto f^{-(1-2\zeta)}, \quad \zeta = -(1/2) - (1/2) * (d \log p(f) / d \log f) \quad (4.5)$$

In the above equations, $h(x)$ is the fracture profile height function, r is the horizontal distance between two points on the fracture profile (equivalent to wavelength in the structure function or window size in the Hurst as well as variational R_q relations), $z_{max}(r)$ is the difference between the maximum and minimum of heights z in the fracture profile within the window r , $R_q(r)$ is the standard deviation of heights z within the window r and f is the inverse of wavelength in the PSD function.

4.3. Materials and methods

Fully dense monolithic Si-C-N ceramics were prepared from the liquid poly(ureamethylvinyl)silazane precursor through a casting route. Details of the processing are described in Chapter 2 [07Jan]. In brief, The process involves the thermal crosslinking of the liquid precursor, cast and sealed in PTFE molds, followed by pyrolysis of the obtained pore-free transparent green bodies in flowing argon or nitrogen atmosphere, at temperatures between 800 and 1300°C to obtain ceramic bodies with structures ranging from amorphous Si-C-N-H to nanocrystalline Si-C-N materials. The samples are denoted here, code-named according to their thermal treatment, e.g., SiCN-080001, SiCN-110001, SiCN-120012, and SiCN-130012, the first four of the digits denoting the pyrolysis temperature (T_p) and the last two denoting the holding time at T_p . Fracture surfaces of the samples were obtained by pre-cracking with Knoop indentation followed by stable crack extension using a specially made loading fixture, which enabled a displacement controlled mode-I loading. The nominal velocity of crack

propagation was $\sim 10^{-4}$ m/s, estimated from the total crack length and propagation time controlled under a light microscope. The topography of fracture surfaces were digitally recorded using atomic force microscopy (AFM, model Multimode Nanoscope IIIa, Digital Instruments, Veeco Metrology Group, Santa Barbara) in tapping mode at image scan sizes ranging from 500×500 nm to 25×25 μm and a pixel density of 512×512 , with the fast scan direction oriented perpendicular to the direction of crack propagation. The fracture surface imaging was performed at a location roughly about 100 to 200 μm behind the final crack front. Standard silicon probe tips were used for imaging except for high-resolution scans e.g., 500×500 nm and 1×1 μm , where super cone tips were also employed. The fractal analysis of the topographic data was performed using variational R_q method, Hurst method, structure function and power spectral density (PSD) as described in the previous section. The above methods were chosen due to their widespread acceptance in the literature for the roughness analysis of surfaces. Additionally, the results could be cross-compared against each other to ascertain the overall reliability of the estimates. The analysis was performed on the 512 line profiles in the fast scan direction, and the results were averaged along the slow scan direction. The only pre-processing applied to the as acquired topographic images before fractal analysis was to correct for the image bow arising from the AFM piezo-scanner, by quadratic subtraction. Additionally, topographic images of the equilibrium loaded mode-I cracks in the near-tip region as well as the crack-tip process zones were acquired in tapping mode at image scan sizes of 500×500 nm and 3×3 μm to examine the elastic deformations and the possibility of 'damage cavities'.

4.4. Results

Fig. 4.1(a) depicts the variation of RMS fracture surface roughness R_q as a function of fracture profile window size r in the amorphous and phase segregated Si-C-N ceramics. In all cases, R_q increased with window size and saturated at a value R_{q-max} commensurate with the general behavior of rough surfaces. The

magnitude of R_{q-max} and the corresponding window size was observed to depend on the extent of crack deflection in the respective materials and increases monotonously from SiCN-080001 through SiCN-130012. From the plot of the same data $R_q(r)$ in double logarithmic coordinates, Fig. 4.1(b), a power law variation of $R_q(r)$ according to $R_q \propto r^\xi$ was observed up to length scales of

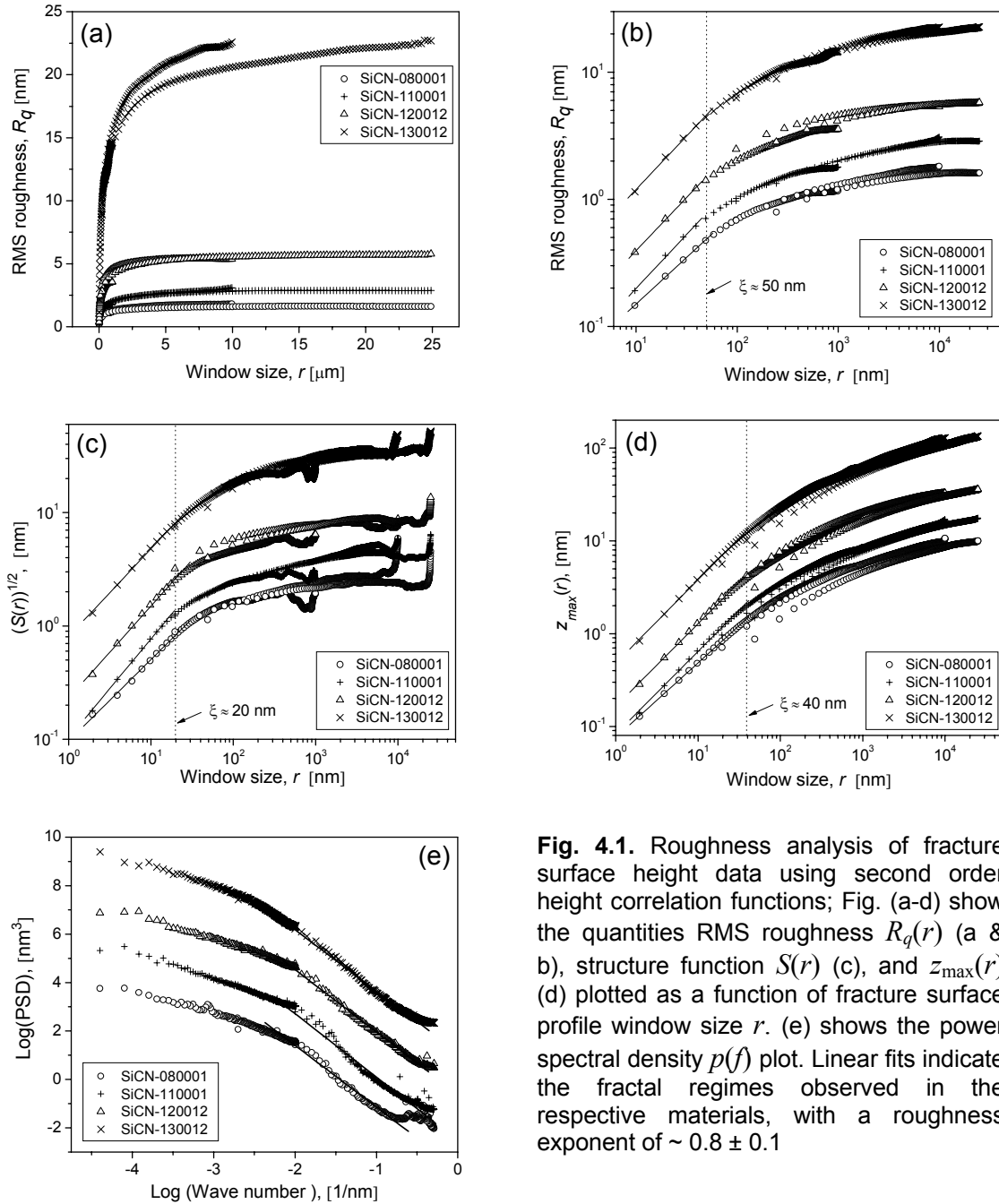


Fig. 4.1. Roughness analysis of fracture surface height data using second order height correlation functions; Fig. (a-d) show the quantities RMS roughness $R_q(r)$ (a & b), structure function $S(r)$ (c), and $z_{max}(r)$ (d) plotted as a function of fracture surface profile window size r . (e) shows the power spectral density $p(f)$ plot. Linear fits indicate the fractal regimes observed in the respective materials, with a roughness exponent of $\sim 0.8 \pm 0.1$

~ 50 nm, signifying the fractal self-affine scaling of roughness in the investigated fracture surfaces. From least square fitting of the respective linear regimes, corresponding self-affine roughness exponents ζ were determined (Table 4.1) all of which lay around 0.8 ± 0.1 . This value is in agreement with the universal roughness exponent conjectured by Bouchaud *et al.* [97Bou]. The range of variations in ζ were smaller for a given evaluation method and were non-systematic. From the extent of the linear portion in the four plots, the self-affine correlation length ξ of the fractal regime was estimated to be around 50 nm. This is in close comparison with the previously reported characterization of the correlation lengths in silicate glass [97Dag, 00Hin] and metallic alloys [02Hin] and polymers [00Rey], where ξ was observed to scale with the microstructural feature size in the corresponding materials. However, a more accurate resolution of the variation in ξ among the materials SiCN-080001 through SiCN-130012 was difficult due to the smaller magnitude of the variations, especially on the logarithmic scale. Also, the fractal regime at smaller length scales corresponding to the 'static-damage' roughness exponent ($\zeta \approx 0.5$) reported by Daguier *et al.* [97Dag] was not observed from the above plots. At length scales between 100 nm to ~10 μm , the plots exhibit a second linear regime (Fig. 4.1(b-e)), corresponding to an exponent of 0.3 ± 0.05 . Such an exponent has not been reported previously in the literature and as such, its physical meaning is not clear at the moment. Plots from the roughness analysis of the fracture surface topographies using the structure function, Hurst method and PSD are presented in Fig. 4.1(c-e), and yield nearly similar results to those of the variational R_q method as above. The determined roughness exponents from all the four methods are summarized in Table 4.1. Notably, no correlation was detected between the fracture toughness values of the materials [07Jana] and their corresponding roughness exponents.

In order to probe the damage mechanisms during fracture, AFM imaging of the crack morphology was performed. Fig. 4.2 (a-c) show the AFM topographic images of the mode-I cracks loaded to equilibrium in SiCN-080001, SiCN-110001

and SiCN-130012 respectively, with the magnified view of the crack tip region included as insets. A flame shaped depression around the crack tip corresponding to the Poisson contraction of the free surface was observed in all the three specimens. Such elastic deformation near the crack tip is well known

Table 4.1. Roughness exponents determined from the least square fits of the linear part of the height correlation function plots in Fig. 4.1. Indicated errors correspond to 95% confidence band. For comparison, the maximum RMS roughness R_{q-max} and the crack-tip toughness K_{I0} values of the respective materials are also included from Chapter 3 [07Jan].

Material	Roughness exponent, ζ				R_{q-max} (nm)	Crack-tip toughness, K_{I0} (MPa m ^{1/2})
	from variable R_q	from structure function	from $z_{max}(r)$	from PSD		
SiCN-080001	0.74 ± 0.01	0.72 ± 0.01	0.8 ± 0.01	0.77 ± 0.02	1.61	0.57
SiCN-110001	0.85 ± 0.03	0.88 ± 0.01	0.89 ± 0.01	0.81 ± 0.02	2.88	1.08
SiCN-120012	0.84 ± 0.02	0.81 ± 0.02	0.89 ± 0.01	0.79 ± 0.01	5.77	0.76
SiCN-130012	0.84 ± 0.02	0.77 ± 0.01	0.89 ± 0.01	0.76 ± 0.01	22.71	1.22

and has been reported in glasses [00Hen], sintered SiC [98Kin] and single crystal NiAl [96Gök]. From the height contrast in the images, the crack opening displacements (COD) in this region appear discontinuous, suggesting the possible formation of ‘damage cavities’ near the crack tip as reported by Celerie *et al.* [03Cel, 03Cela]. However, the extremely narrow CODs in this region relative to the AFM probe tip radius, along with the nanoscale roughness of the specimen surface cast ambiguity to this inference. To ascertain the presence of any *persistent* damage cavities formed during crack propagation, high-resolution

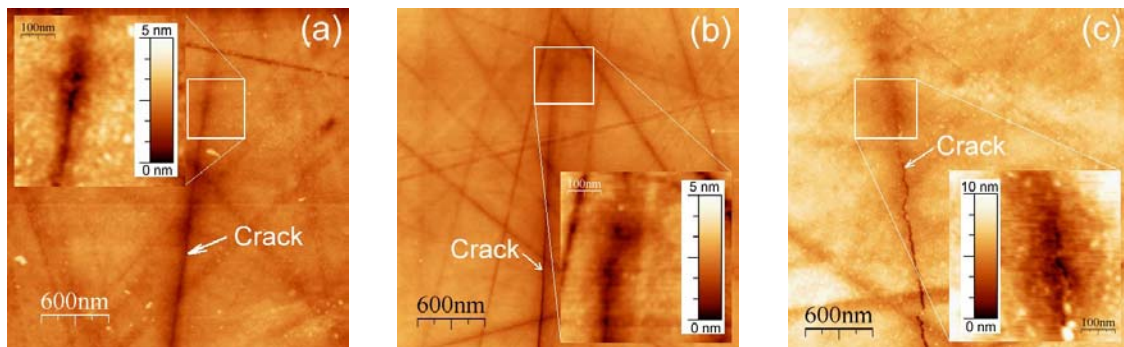


Fig. 4.2. AFM topographic images of the loaded crack tips in SiCN-080001 (a) SiCN-110001 (b) and SiCN-130012 (c); insets show the magnified view of the crack-tip, revealing poisson contraction of the free surface.

topographic images of the cracks were recorded from regions few micrometers behind the crack tip, where the crack edges are well-defined. The images from SiCN-080001, an electron-amorphous material (Chapter 2, [section 3.2.5](#)) [07Jan], and SiCN-130012, which is partly phase separated containing TG and n-SiC in an amorphous Si-C-N matrix [07Jan] are shown in [Fig. 4.3\(a\)](#) and [Fig. 4.3\(b\)](#) respectively. Interestingly, the amplitude of nanoscale crack deflection (R_{max}) in the amorphous SiCN-080001 specimen (*viz.*, from [Fig. 4.3\(a\)](#), $R_{max} \approx 10$ nm; also from RMS roughness $R_q \approx 1$ nm (Chapter 3, [Table 3.2](#)) [07Jana]) are higher than those observed in oxidic glasses ($R_{max} \approx 2.5$ nm; $0.3 \leq R_q \leq 0.8$) [00Gup, 04Gui, 05Gui]. From the images, it is seen that the left and right sides of the crack edge profiles in both the materials match exactly, strongly suggesting the absence of damage cavities in the resolvable length scales. This is in agreement with the analysis of Guin and Wiederhorn [04Gui, 05Gui], who derived the same result by a three-dimensional matching of the fracture surface undulations in soda-lime and silica glasses at comparable resolutions. It is to be noted here that a three dimensional visualization of crack opening morphology from AFM topographic images such as in [Fig. 4.3](#) may give an impression of discontinuities in crack opening along the crack, suggestive of cavity formation. However, this involves a potential artifact arising from the variability of the AFM probe tip penetration into the crack opening, which is strongly dependant on the spatial orientation of the accessible crack faces relative to the probe tip. Crack face orientations that are skewed about the nominal direction of crack

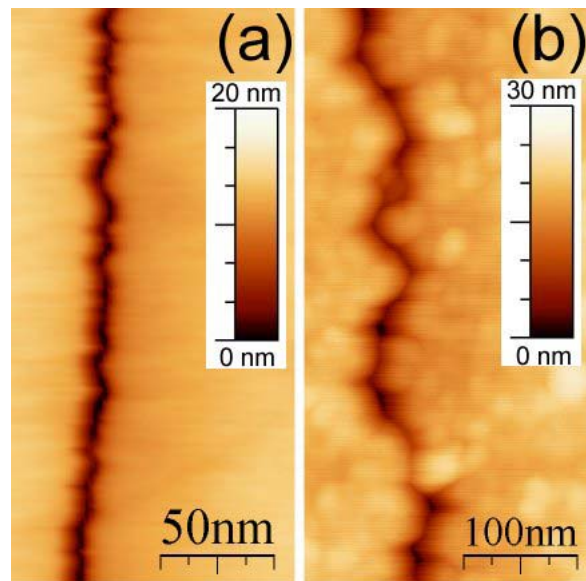


Fig. 4.3 AFM topographic images of the loaded cracks from locations close to the crack tip in SiCN-080001 (a) and SiCN-130012 (b); Note that the crack faces on the left and right sides match exactly, proving the absence of *persistent* damage cavities during crack propagation.

propagation (e.g., mode-III deflections) will lead to smaller probe penetration depths. Thus, in the near-tip regions where the COD are close to the limit of lateral resolution, variations in tip penetration may be perceived as discontinuities in crack openings.

4.5. Discussion

Roughness analysis of fracture surface topography from the investigated Si-C-N materials reveal self-affine scaling, in agreement with the universal observation of fractal scaling in fracture surfaces from a wide range of materials [97Bou]. However, the extracted self-affine roughness exponents ζ from the observed fractal regimes do not show any correlation with the fracture toughness. This is especially significant as the observed variation in toughness, concomitant with the microstructural evolution in the materials (in spatial respect, which can be related to the crack roughness at appropriate length scales) is not monotonous but sensitive to the phase evolution, i.e., the nature of phases formed. This can be appreciated from the observed non-monotonous variations in toughness in materials SiCN-110001 through SiCN-130012 juxtaposed to the monotonous increase in crack roughness, the former clearly correlating with the phase segregation of TG and n-SiC. The absence of a direct one-to-one correspondence between toughness and increased crack roughness is immediately illustrated, when fracture in porous materials or poly-phase materials composed of weak phases or interfaces is considered [90Dux]. In such materials, a net increase in toughness can be realized only when the reduction in fracture resistance caused by these microstructural elements is adequately offset by toughening contributions from crack tip blunting or crack deflection [93Law].

The geometrical contribution to toughening visualized to manifest in a higher fractal dimension (or smaller roughness exponent, leading to a higher crack tortuosity) takes into account only the *richer texture* at small length scales *relative* to larger length scales, which is independent of the magnitude of crack tortuosity,

viz., the roughness. This is significantly different from the classical fracture mechanics approach, where both the changes in magnitude and direction of crack path are accounted (embodied in the net increase in fracture surface area) to yield crack deflection toughening [93Law]. Interpretation of the toughness variations in the investigated materials according to the later approach was presented in Chapter 3 [07Jana]. As the fractal regime in the present materials is limited to ~ 50 nm, the length scales at which potential variations in the fracture surface texture leading to a $K_{I0} - \zeta$ correlation lie close to the resolution limits of AFM topographic imaging. However, experiments with different AFM probe tips showed that the tip convolution of the topographic data did not significantly affect the estimated ζ values, suggesting that any systematic variations in texture leading to variations in ζ were not obscured by the measurement technique.

While the absence of correlation between the roughness exponents and fracture toughness is clear from the above, the estimated roughness exponents from all the four materials compare closely with the large length scale roughness exponent ($\zeta \approx 0.8$) reported from the fractal analysis of fracture surfaces in a range of materials [97Bou, 03Bou]. Thus, the present results reinforce the conjecture by Bouchaud *et al.* that the self-affine roughness exponents in fracture surfaces are universal [97Bou]. The non-observation of the small scale ($\zeta \approx 0.5$) exponent in the present roughness analysis can be related to the applied crack velocity ($v \approx 10^{-4}$ m/s) in the present fracture experiments. From the roughness analysis of silica glass fracture surfaces, Daguer *et al.* found a downward shift of the crossover length ξ_c between small scale and large scale roughness exponents at increasing crack velocities, with ξ_c measuring only a few nanometers at $v \approx 10^{-7}$ m/s [97Dag]. The structure of the presently investigated materials being comparable to those of silicate network glasses, it is reasonable to expect that the crossover lengths are shifted to sub-nanometer scale due to the higher crack velocity employed. The similarity in the structure with respect to fractal scaling is also reflected in their respective fractal correlation lengths, which lay around 100 nm for silicate glasses [03Cel, 97Dag, 00Hin], comparable with

50 nm presently observed in the Si-C-N ceramics. A comparison of the correlation lengths observed from the roughness analysis of fracture in a variety of materials ranging from metals, ceramics and polymers reveal that ξ scales with their respective microstructural dimensions [03Cel, 03Bou, 97Dag, 00Hin, 02Hin, 00Rey], suggesting correlations with the *geometrical* contributions of toughening. Such a correlation between ξ and fracture toughness was discussed in [94Bou], where an inverse relationship between ξ and K_{IC} , for a given crack roughness amplitude (z_{max} , outside the fractal regime) was proposed. The presently estimated fractal correlation lengths in Si-C-N ceramics are relatively smaller than those in silicate glasses, although no resolvable variation was detected among the four materials, correlating with their respective toughness values. While the proposed correlation in [94Bou] with respect to ξ needs to be verified on several materials, it can be expected that ξ reflects correlations of fracture processes at length scales comparable with the process zone size.

The following discussion will focus on the correlation between the material structure and potential damage processes that facilitate fracture initiation and propagation, leading to the observed nanoscale crack roughness. It is evident that the fracture in the phase segregated materials SiCN-120012 and SiCN-130012 is strongly influenced by TG and n-SiC phases. These second phases and their interfaces with the amorphous Si-C-N matrix presumably act as microstructural defects leading to crack initiation, whereas crack deflection is governed by their respective surface energies, phase morphology and the surrounding thermo-elastic stress fields (Chapter 3) [07Jana]. Hence, the associated contribution to the increase in crack roughness can be described by brittle fracture. Nevertheless, the microstructures of the phase segregated materials also contain an appreciable fraction of amorphous Si-C-N phase, and its individual contribution to the crack roughness needs to be considered. The later contribution is manifested in the crack roughness of amorphous Si-C-N materials *viz.*, SiCN-080001 through SiCN-110001. While no second phase was resolvable using high-resolution transmission electron microscopy (HRTEM) in

these materials, progressive formation and organization of sp^2 carbon was detected by Raman spectroscopy (Chapter 2) [07Jan]. However, considering the concomitant increase in toughness with the increase in crack roughness (Chapter 3, Table 3.1), it can be deduced that the sub-nanometer sized sp^2 carbon domains did not function as weak interfaces (which is the case in the fracture of SiCN-120012) in deflecting the crack. On the other hand, the simultaneous increase in the density and elastic modulus in materials SiCN-080001 through SiCN-110001 reveal the densification of the amorphous structure through increased network connectivity, via the stripping of residual hydrogen, to varying extents determined by the degree of pyrolysis (Chapter 2) [07Jan]. Removal of residual hydrogen has been identified to introduce nano-voids in the precursor-derived Si-C and Si-C-O amorphous ceramic fibers, where a reduction in the void number density coupled with the void growth evolves at higher pyrolysis temperatures [96Suz]. A graphical evidence of the density fluctuations in amorphous Si-B-C-N precursor-derived ceramics (PDC) was achieved using STEM-HAADF imaging [99Bau]. Additionally, compositional fluctuations in the form of sub-nano sized domains structurally similar to SiC and Si_3N_4 have also been detected in binary and ternary Si-C-(N) PDC, by small angle X-ray and neutron scattering [96Suz, 98Sch]. The progressive evolution of the above density and compositional fluctuations in terms of size, amount and distribution in materials obtained at $800^\circ\text{C} < T_p < 1100^\circ\text{C}$ evidently provide sources of crack deflection, even in the amorphous state. Specifically, the increase in the size of the fluctuations, coupled with the decrease in the number density of the nano-voids can clearly explain the increased crack roughness in materials SiCN-080001 through SiCN-110001. This is perfectly in agreement with the experimental and simulation investigations on the fracture of silicate glasses [00Gup, 99Cam] and amorphous Si_3N_4 [97Kai]. The needed further resolution here is, whether the fracture involved any amount of permanent non-elastic deformation before material separation, e.g., *via* void growth and coalescence, as suggested from MD simulations [99Van, 97Kai].

Experimental evidence confirming the later damage mechanism requires the identification of persistent damage cavities along the propagating crack. However, the topographic images of the crack in the amorphous SiCN-080001 as well as the phase separated SiCN-130012 do not resolve any such cavities. This result only allows us to interpret the fracture in precursor derived Si-C-N ceramics as brittle. However, it is to be noted that the static damage fractal regime (whose roughness exponent $\zeta \approx 0.5$ was proposed to characterize the fractal scaling within the damage cavities [03Bou, 97Dag]) was not observed in the present roughness analysis of the fracture surfaces. As this regime was shown to emerge only at extremely low crack velocities for silicate glasses [97Dag], a further resolution on the fracture damage mechanisms of the title materials requires roughness analysis of cracks realized at crack velocities $<10^{-11}$ m/s.

4.6. Conclusions

Roughness analysis of fracture surfaces from precursor-derived amorphous and phase segregated ceramics were carried out using RMS roughness (R_q) and second order height-height correlation functions. The evolution of R_q was well correlated with the evolution of sub-nanoscale structural and compositional inhomogeneities in the amorphous materials and formation of second phases in the phase segregated materials, leading to crack deflection. Fractal analysis of the fracture surface roughness revealed self-affine scaling up to a correlation length of around 50 nm and a self-affine roughness exponent of 0.8 ± 0.1 in all the materials, the later in agreement with the universal roughness exponent conjectured by Bouchaud *et al.* Specifically, no correlation was observed between the observed roughness exponents and the fracture toughness of the corresponding materials. Examination of the crack opening near the crack tip revealed no persistent damage cavities along the crack, concluding that the fracture in the investigated Si-C-N ceramics proceeded in a brittle manner at crack velocities employed in the experiments.

5. Nanoindentation analysis of elastic and plastic deformation in precursor-derived Si-C-N ceramics

5.1. Introduction

Precursor-derived silicon based non-oxide ceramics are a new class of materials investigated for room- and high-temperature structural applications [95Bil]. By virtue of their synthetic route, these materials are predominantly amorphous or nanocrystalline at the end of the precursor-to-ceramic transformation depending on the precursor chemistry and processing conditions [96Mon], and display brittle fracture behavior under remote loading, comparable to inorganic silicate glasses [02Wal, 02Bau, 03Mor]. The fracture mechanical characterization of the title materials under remote loading was presented in Chapter 3, where the crack-tip toughness (K_{I0}) was evaluated for a range of Si-C-N ceramics encompassing hydrogenated amorphous to nanocrystalline structures [07Jana]. While the gross fracture behavior of amorphous ceramics is evidently brittle at the macro- and micro- scale regimes, the possibility of inelastic permanent deformation at crack tips preceding fracture in the nano-scale regime is currently under intense study [03Cel, 04Gui]. This possibility was investigated with respect to amorphous Si-C-N ceramics in Chapter 4 and it was found that the fracture proceeds by brittle cleavage even at length scales of the order of few tens of nanometers at the employed crack velocities [07Janb]. In contrast to the deformation behavior under remote loading, permanent plastic deformation in inorganic glasses and amorphous ceramics under contact loading e.g., by sharp indenters is well documented, and is known to arise due to the tri-axial compressive stress state in the contact zone [64Mar, 68Nee]. As precursor derived ceramics (PDC) are envisaged for tribological applications [06Kla] and in MEM device components [01Lie] where contact loading is prevalent, understanding of the elastic and plastic deformation behavior of these materials under contact loading is important.

Previous studies have revealed that the deformation behavior of PDC under indentation is also comparable to that of silicate network glasses [01Rou, 04Bur]. Specifically, the permanent deformation in amorphous Si-C-O and Si-C-N PDC under the indenter has been identified to display anomalous behavior, occurring predominantly by the non-volume conserving densification rather than the volume conserving shear flow, commensurate with the estimated low values of (elastic modulus normalized) residual stresses [01Rou, 04Bur]. Evaluation of the nanoindentation hardness and elastic modulus of an amorphous Si-C-N ceramic was reported in [01Gal], although the results were influenced by porosity in the samples. Apart from this work and a couple of microhardness evaluations of Si-O-C PDC [01Rou, 96Sor, 02Sha], no systematic quantitative investigations on the indentation deformation of PDC have been carried out until now, partly due to the unavailability of fully dense homogeneous test specimens. Additionally, it is obvious that the relative extent of densification and shear flow during plastic deformation cannot be distinguished from the measured values of indentation hardness. This distinction can be important in controlling the evolution of material resistance to deformation beyond the elastic limit.

In this Chapter, a detailed investigation of the elastic and plastic deformation in precursor-derived Si-C-N ceramics by spherical and Berkovich indentation is presented, using depth-sensing nanoindentation measurements. Adopting the well established Oliver-Pharr method [92Oli], the evolution of indentation hardness and elastic modulus are evaluated for a series of Si-C-N PDC varying in material structures, from partly hydrogenated amorphous to phase separated nanocrystalline states. From the analysis of reversible and irreversible energies evaluated from the indentation load-unload cycle, contributions from the elastic and plastic deformation during indentation are discussed in correlation with hardness and elastic modulus. The indentation size effect on hardness is examined from the measurement of Meyer hardness using Vickers microindentation at loads ranging from 0.245 N to 49.05 N. By applying two individual nanoindentation reverse analysis methods reported in literature, an

attempt is made to evaluate the plastic deformation parameters *viz.*, yield stress and strain hardening exponent from the analysis of the experimentally recorded loading and unloading *P-h* curves. From an analysis of hold time creep deformation, the effect of strain rate on plastic deformation is examined. The pile-up and sink-in behavior is probed by atomic force microscopy (AFM) imaging of residual impressions from Vickers indentation.

5.2. Experimental procedure

5.2.1. Materials

Fully dense monolithic Si-C-N ceramics were prepared from the liquid poly(ureamethylvinyl)silazane precursor through a casting route. Details of the processing are described in Chapter 2 [07Jan]. In brief, the process involves the thermal crosslinking of the liquid precursor, cast and sealed in PTFE molds, followed by pyrolysis of the obtained pore-free transparent green bodies in flowing argon atmosphere, up to various final pyrolysis temperatures between 800 and 1300°C. By this way, a range of material structures of the final ceramic products were realized, varying from partly hydrogenated amorphous to nanocrystalline microstructures. A detailed structural and phase characterization of these materials is reported in [07Jan]. The materials are denoted here, code-named according to their thermal treatment, *viz.*, SiCN-080001, SiCN-090001, SiCN-100001, SiCN-110001, SiCN-120012 and SiCN-130012, the first four digits denoting the temperature and the last two digits, the hold time of the pyrolysis / annealing treatment. The materials SiCN-080001 through SiCN-110001 are electron-amorphous, whereas the remaining two possess phase separated microstructures. The resultant ceramic bodies were subsequently ground and polished in the form of thin (200 – 400 μm) rectangular plates with dimensions 8×4 mm, with the final surface finishing performed with a 0.25 μm diamond suspension.

5.2.2. Indentation

Nanoindentation experiments were performed using a *Nano Indenter*® *XP* nanoindentation system (MTS Nano Instruments, Oak Ridge, TN, USA), located in a temperature and atmosphere controlled laboratory. Two sets of nanoindentation measurements were made using a Berkovich indenter. In the first set, P - h curves were recorded with five different maximum loads (P_{max}) of 25, 50, 100, 200 and 500 mN, using the following schedule: 30 s loading to P_{max} ; 10 s hold at P_{max} ; 30 s to full unload. In the second set, P - h curves were recorded in the continuous stiffness measurement (CSM) mode under the following parameters: load cycle depth limit target \approx 1500 to 1950 nm (leading to $P_{max} \approx$ 450 to 490 mN); strain rate target: 0.05 s⁻¹; superimposed harmonic amplitude limit: 2 nm; harmonic frequency: 45 Hz; 10 s hold at P_{max} ; 20 s to 90% unload; 50 s hold at 0.1 P_{max} for drift correction followed by full unload. For both the above measurements, ten indentations were made for each sample-load combination for statistical evaluation. Nanoindentation P - h curves using a spherical tipped indenter (tip radius (R_{sph}) = 150 μ m) were recorded with $P_{max} =$ 500 mN using the following schedule: 60 s loading to P_{max} ; 10 s hold at P_{max} ; 60 s to full unload. A minimum of thirty measurements were made for each material, and the data that showed significant deviation from the spherical contact exponent of 1.5, arising from imperfect initial contact were discarded. Prior to actual measurements, the nanoindentation system was calibrated for frame compliance and tip shape imperfection using a fused silica standard specimen.

Vickers microindentation was performed using a *Micromet 1* microhardness tester (Buehler Ltd., Lake Bluff, IL, USA) for indentation loads 0.245, 0.490, 0.981, 1.962, 4.905 and 9.81 N, and using a *Zwick* indentation instrument (Zwick & Co. KG, Einswigen, Germany) for loads 19.62 and 49.05 N with a dwell time of 15 s at maximum load. Four to six indentations were made at each load. AFM topographic imaging of the residual Vickers impressions was carried out in tapping

mode using a *Multimode Nanoscope IIIa* AFM (Digital Instruments, Veeco Metrology Group, Santa Barbara) and standard Si probe tips. The images were recorded in height and amplitude contrasts simultaneously. The former contrast served to dimensionally quantify the topography via section analysis, while the latter enabled to resolve the finer variations or features in topography.

5.3. Results

5.3.1. Analysis of Berkovich loading curves and tip imperfection

The representative P - h curves recorded from Berkovich nanoindentation of specimens SiCN-080001 through SiCN-130012 are shown in Fig. 5.1. For visual clarity, only the data from the 500 mN load is included. In order to examine the square dependence of displacement (h) to the load (P) in the loading curve as expected from ideal self-similar indenters [04Che], least square fitting of the loading curve data from loads 25 mN through 500 mN was performed according to the general power expression

$$P = Ah^{x_f} \quad (5.1)$$

The loading curve exponent $x_l = x_f$ from the curve fits varied from 1.81 to 1.97 for loading curves from $P_{max} = 25$ mN through 500 mN, while showing negligible dependence to the material being indented. Accordingly, the deviation from the square dependence can be ascribed to the indenter tip imperfection. Assuming that the actual tip has worn to a spherical shape, the tip radius R_{Berk} was estimated following the procedure described by Cheng *et al.* [98Che] by least square fitting of

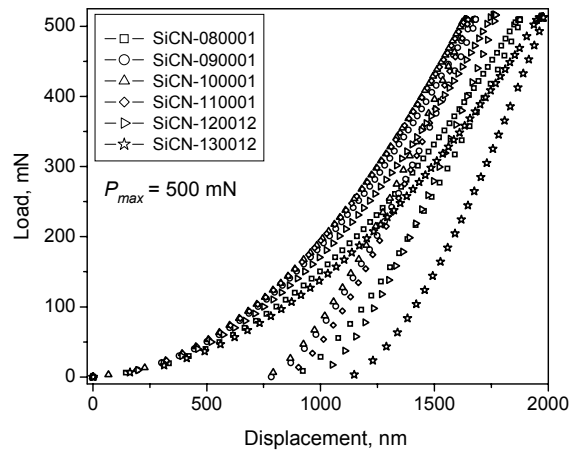


Fig. 5.1. Representative P - h curves from Berkovich nanoindentation of Si-C-N ceramics with $P_{max} = 500$ mN.

the measured loading curves according to the quadratic polynomial expression

$$P = c_0 h^2 + c_1 h + c_2 \quad (5.2)$$

from which R_{Berk} was estimated as

$$R_{Berk} = c_1 / \left(2c_0 \left((1 / \sin \psi) - 1 \right) \right) \quad (5.3)$$

where $\psi = 70.3^\circ$ for Berkovich indenter. The derived values showed wide scatter with $R_{Berk} \approx 360 \pm 160$ nm. As the loading curves from 500 mN loading are the least influenced with respect to the tip imperfection, the evolution of material parameters across different materials will be discussed in the following, mainly based on the analysis of these P - h curves, except where load dependence of the material behavior is observed.

5.3.2. Oliver-Pharr analysis – Berkovich indentation

Towards evaluating elastic modulus and hardness of the materials, the Oliver-Pharr analysis [92Oli] was applied, along with the recent refinements presented by the same authors in [04Oli]. Accordingly, the unloading curves were least square fitted to the expression:

$$P = B(h - h_{res})^{x_{ul}} \quad (5.4)$$

where h_{res} is the residual depth at full unload, and x_{ul} is the unloading curve exponent. The derived values of x_{ul} increased from 1.39 to 1.49 in materials SiCN-080001 through SiCN-130012 respectively, while a smaller increase was also observed with increasing maximum load, P_{max} . The unloading slope (S) was evaluated from the derivative of Eq. 5.4 at P_{max} . The true contact depth (h_c) was evaluated from the relation

$$h_c = h_{\max} - \chi(P_{\max} / S) \quad (5.5)$$

where the geometric parameter χ was explicitly evaluated according to Eq. 17 in Ref. [04Oli] using the value of x_{ul} for each unloading curve. The value of χ showed only a marginal variation in the range $0.76 \leq \chi \leq 0.75$. The true contact area (A_c) was evaluated taking into account the tip imperfection via the use of an area function calibrated using fused silica standard. Further, the elastic modulus (E) and hardness (H) were evaluated from the relations:

$$E_r = \frac{1}{\beta} \frac{\sqrt{\pi}}{2} \frac{S}{\sqrt{A_c}} \quad (5.6)$$

$$\frac{1}{E_r} = \frac{1-\nu^2}{E} + \frac{1-\nu_i^2}{E_i} \quad (5.7)$$

$$H = P_{\max} / A_c \quad (5.8)$$

A value of $\beta = 1.05$ was used in Eq. 5.6. [04Oli] $E_i = 1141$ GPa and $\nu_i = 0.07$ are the elastic modulus and Poisson's ratio of the diamond indenter. The Poisson's ratios of the investigated Si-C-N materials were 0.245, 0.24, 0.22, 0.21, 0.22 and 0.23 for materials SiCN-080001 through SiCN-130012 respectively, obtained from the resonance frequency testing using circular disk specimens (Chapter 2) [07Jan]. The evolution of elastic modulus and hardness in materials SiCN-080001 through SiCN-130012 evaluated from the unloading curve analysis as above is presented in Fig. 5.2(a) and 2(b) respectively. The elastic modulus increased in amorphous materials SiCN-080001 through SiCN-110001 from 95 GPa through 140 GPa, and decreased in the phase separated materials SiCN-120012 and SiCN-130012 to 129 GPa and 105 GPa respectively. Elastic moduli of these materials have been determined independently by resonance frequency testing (82, 106, 117, 127, 140, and 117 GPa for materials SiCN-080001 through SiCN-130012

respectively, Chapter 2) [07Jan], and represent the mean behavior from the whole specimen bulk. Compared to these values, the elastic moduli from the unloading curve analysis were higher by 15 to 10 % for the amorphous materials and by 8 and 10 % lower for the phase separated materials. The nanoindentation hardness increased from 12.4 GPa to 15.7 GPa in materials SiCN-080001 through SiCN-100001 and decreased from 14.5 GPa to 9.3 GPa in materials SiCN-110001 through SiCN-130012. On the other hand, the variations of E and H with increasing maximum indentation loads from 50 mN through 500 mN were comparatively small. The above results are in excellent agreement with those from the CSM analysis, Fig. 5.2(c) and Fig. 5.2(d), where the evolution of

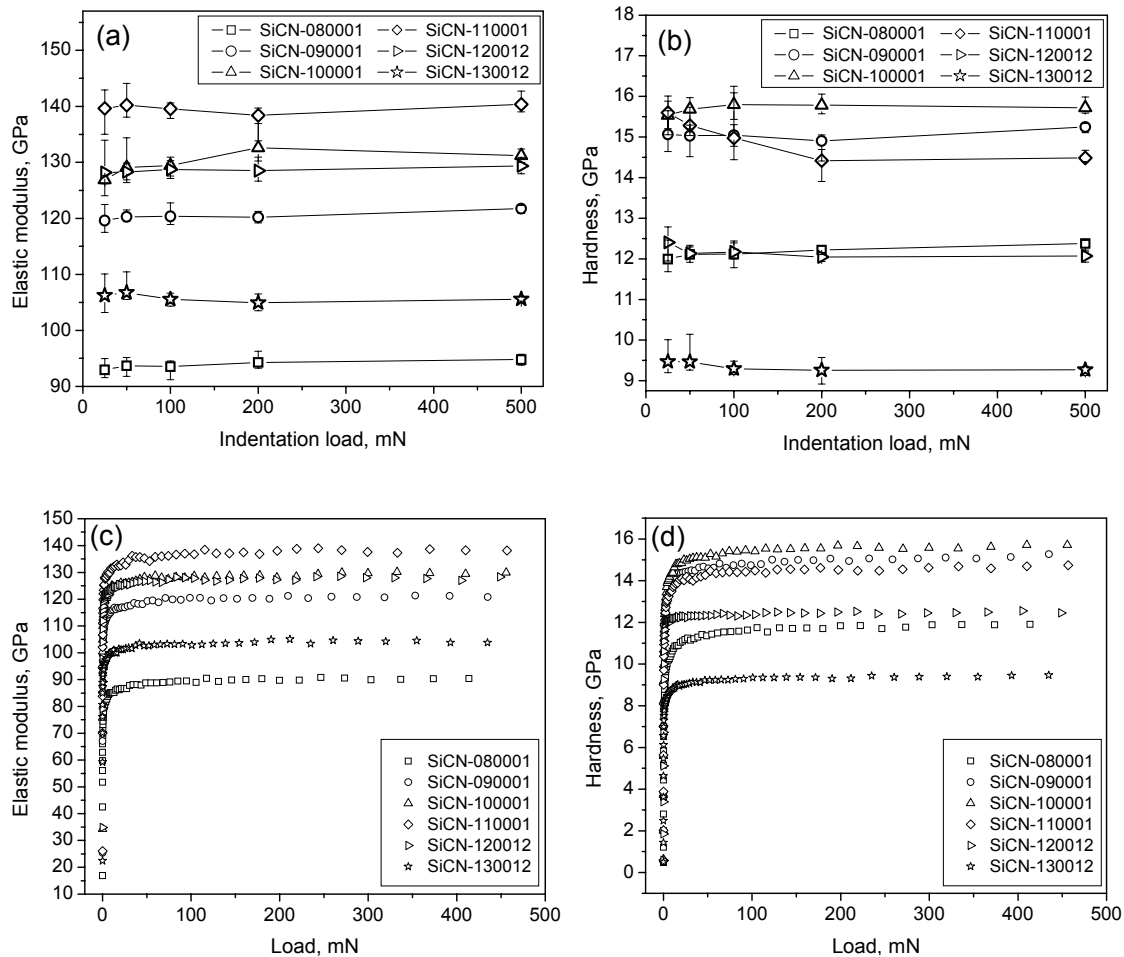


Fig. 5.2. Elastic modulus (a) and hardness (b) of Si-C-N ceramics determined from Oliver-Pharr analysis of Berkovich nanoindentation data obtained at $25 \text{ mN} \leq P_{max} \leq 500 \text{ mN}$. (c) and (d) show the evolution of elastic modulus and hardness determined from CSM analysis.

respectively E and H , with progressively increasing load is plotted.

5.3.3. Oliver-Pharr analysis – spherical indentation

Plastic deformation invariably accompanies elastic deformation during sharp indentation and has been recently supposed to affect elastic modulus measurements in PDC [06Moy]. In order to verify this possibility on the elastic moduli determined as above, the moduli of three materials, SiCN-080001, SiCN-110001 and SiCN-130012 that cover the entire range of the investigated Si-C-N material structures, were independently evaluated by spherical indentation within the elastic contact regime.

The representative P - h curves recorded from these measurements with $P_{max} = 500$ mN are presented in Fig. 5.3. The respective loading and unloading curves overlap with each other for all the three materials, indicating that the deformation was completely elastic during the experiments. Least square fitting of the unloading curves according to Eq. 5.1 also showed that the unloading

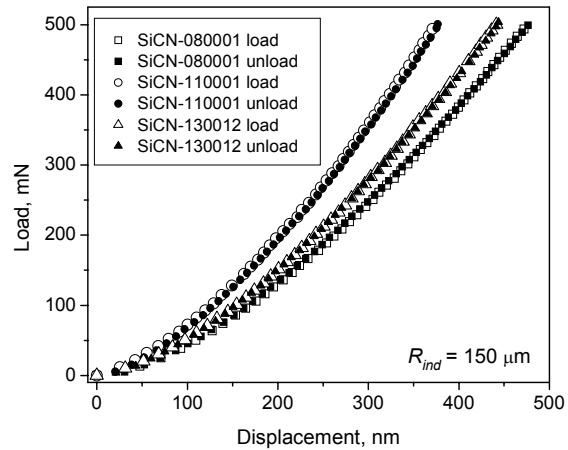


Fig. 5.3. Representative P - h curves from spherical nanoindentation of Si-C-N ceramics with $P_{max} = 500$ mN.

curve exponents $x_{ul} = x$ varied in the range $1.49 \leq x_{ul} \leq 1.53$, closely comparing with the theoretical value of 1.5 expected for elastic spherical contact loading. The elastic moduli of the materials were evaluated by applying the Oliver-Pharr method of unloading curve analysis for spherical indentation [01Her]. The contact depth h_c was evaluated from Eq. 5 with $\chi = 0.75$ verified as described earlier. That the contact loading was elastic was also verified from the ratio h_c / h_{max} yielding a value of 0.507 ± 0.02 , comparing well with the theoretically expected value of 0.5 [01Her]. The contact radius (a_c), contact area (A_c) and the mean contact pressure (p_m) at maximum load P_{max} were evaluated from the relations:

$$a = \sqrt{2h_c R - h_c^2} \quad (5.9)$$

$$A_c = \pi a_c^2 \quad (5.10)$$

$$p_m = P_{max} / \pi a_c^2 \quad (5.11)$$

E_r and E were evaluated respectively from [Eq. 5.6](#) and [Eq. 5.7](#) with $\beta = 1$ in accordance with spherical indentation [[04Oli](#)]. The values of E from the analysis were 96.8 ± 1.4 GPa, 141 ± 4.7 GPa and 113 ± 4.2 GPa for materials SiCN-080001, SiCN-110001 and SiCN-130012 respectively, in good agreement with those derived from the Berkovich indentation analysis. This shows that the elastic moduli determined by the later analysis were not drastically influenced by plastic deformation. Specifically, the measurements were unaffected by errors due to pile-up or sink-in effects. However, as mentioned in the previous section, small variations were indeed observed at increasing applied loads for Berkovich indentation. This load effect will be further described in [section 5.3.5](#). The mean contact pressures (p_m) at P_{max} were 2.18 ± 0.07 GPa, 2.77 ± 0.17 GPa and 2.41 ± 0.18 GPa in the respective materials. Evidently, these values are far less than the contact pressures (hardness) realized in the Berkovich indentation experiments.

5.3.4. Analysis of the load-unload cycle

While the elastic modulus and nanoindentation hardness evaluated as above quantify the overall variations in the elastic and plastic deformation in the materials during contact loading, they do not completely describe the nature of the deformation process. Previous studies have shown that more insight into such processes is gained by the analysis of the load-unload cycle [[04Che](#), [04Oli](#), [03Att](#)]. The widely studied parameters in this approach are the residual depth of penetration (h_{res}), total work of contact deformation (W_{tot}), work from elastic

recovery (W_{el}) and the work of inelastic deformation (W_{pl}). The quantities of W_{tot} , W_{el} and W_{pl} are directly obtained from the load-unload P - h cycle as the area under the loading curve, under the unloading curve and the area enclosed by the two curves respectively. A schematic of the nanoindentation load-unload cycle illustrating the above parameters is shown in Fig. 5.4. For efficient analysis the depth quantities

are usually normalized with the depth at maximum load h_{max} and the work quantities are normalized with the total work W_{tot} , leading to the characteristic ratios e.g., h_{res} / h_{max} , W_{pl} / W_{tot} , W_{el} / W_{tot} etc. The residual depth ratio h_{res} / h_{max} and plastic work ratio W_{pl} / W_{tot} characterize the extent of plastic deformation during contact loading and thus were examined with respect to the deformation behavior of the present Si-C-N materials.

The evolutions of the ratios h_{res} / h_{max} and W_{pl} / W_{tot} in materials SiCN-080001 through SiCN-130012 are presented in Fig. 5.5(a) and Fig. 5.5(b) respectively. The residual depth ratio registered a small decrease from 0.46 to 0.44 in materials SiCN-080001 through SiCN-100001 and increased from 0.50 to 0.56 in materials SiCN-110001 through SiCN-130012. This variation correlates well with the evolution of hardness in the corresponding materials. In comparison, the plastic work ratio increases from 0.41 to 0.49 in materials SiCN-110001 through SiCN-130012, but remains nearly constant at 0.34 in materials SiCN-080001 through SiCN-100001. The correlation between the residual depth ratio and plastic work ratio is presented in Fig. 5.6. The increase in residual depth ratio and plastic work ratio in materials SiCN-110001 through SiCN-130012 display a linear correlation, indicating the progressively increasing extent of plastic deformation in

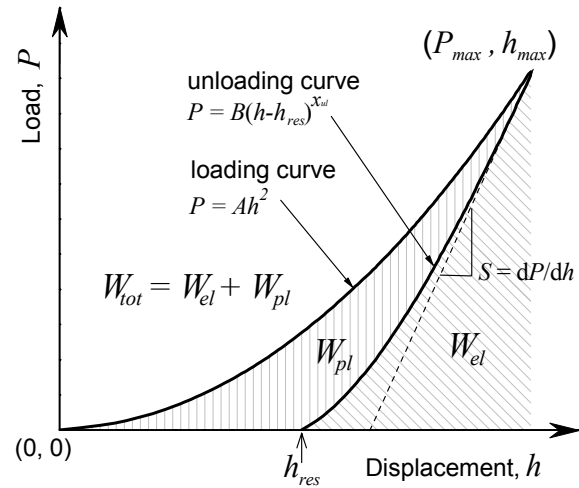


Fig. 5.4. Schematic of the nanoindentation loading-unloading cycle illustrating key experimental parameters.

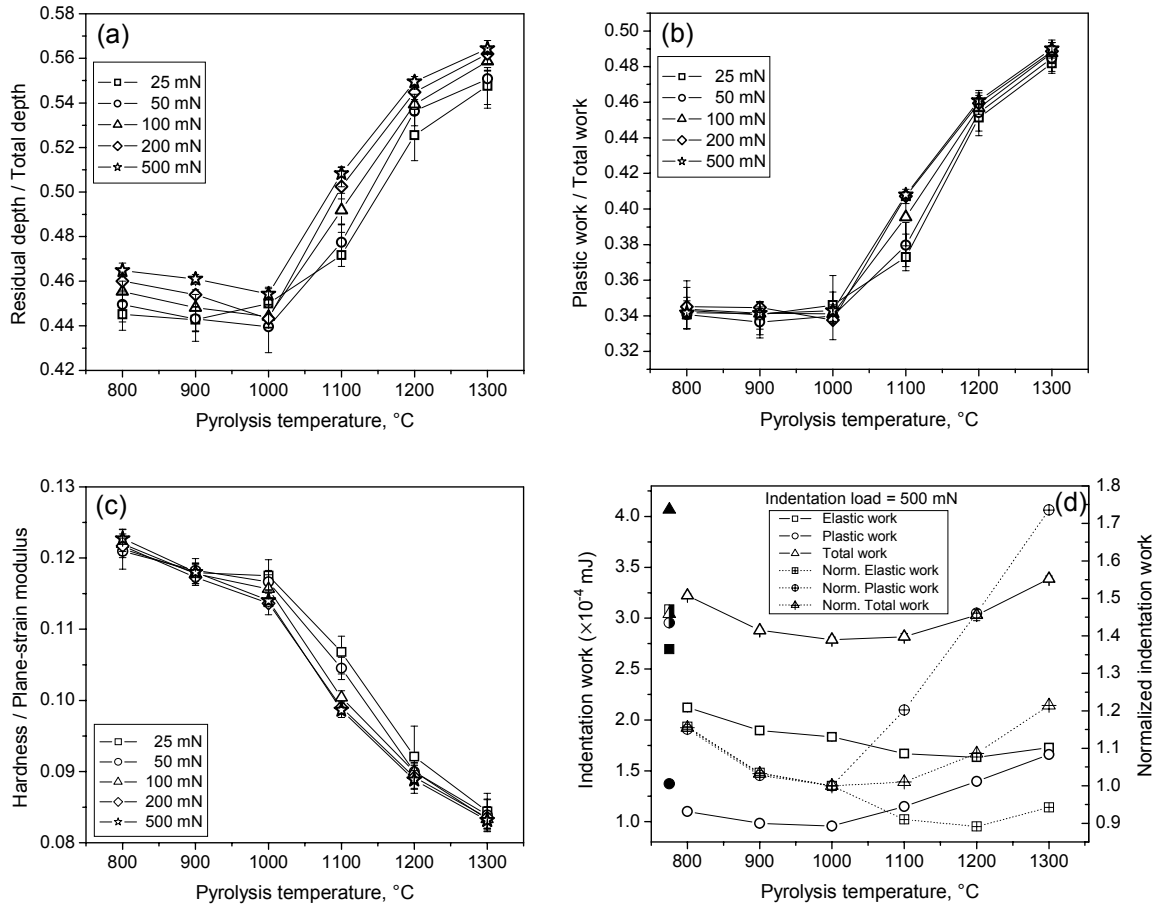
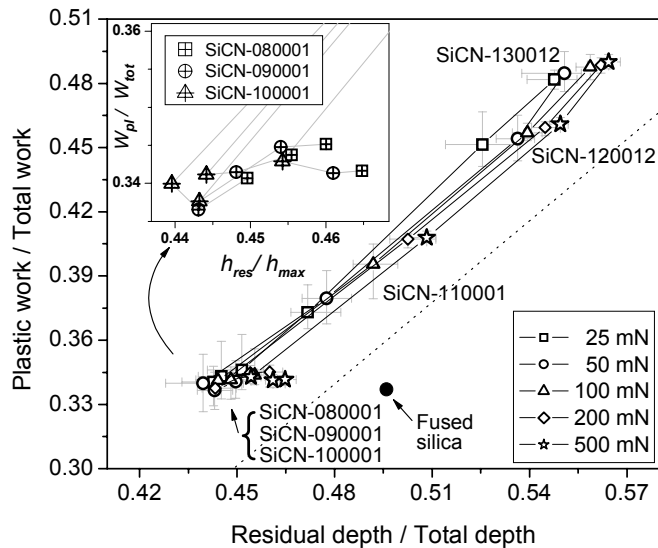


Fig. 5.5. Evolution of the ratios h_{res} / h_{max} (a), W_{pl} / W_{tot} (b) and H / E^* (c) evaluated from the load-unload cycle data from Berkovich nanoindentation of Si-C-N ceramics. The elastic, plastic and total work of indentation is plotted in (d). Crossed symbols are indentation work normalized with those from SiCN-100001. Filled and half-filled symbols show respectively absolute and normalized work data from fused silica.

Fig. 5.6. Correlation between the ratios h_{res} / h_{max} and W_{pl} / W_{tot} evaluated from the load-unload cycle data from Berkovich nanoindentation of Si-C-N ceramics. The dotted line is the linear correlation reported in Ref. [04Che]. The data point of fused silica (full circle) is derived from the $P-h$ curve reported in Ref. [04Oli]. The region covering the amorphous ceramics SiCN-080001 through SiCN-100001 is magnified in the inset for clarity.

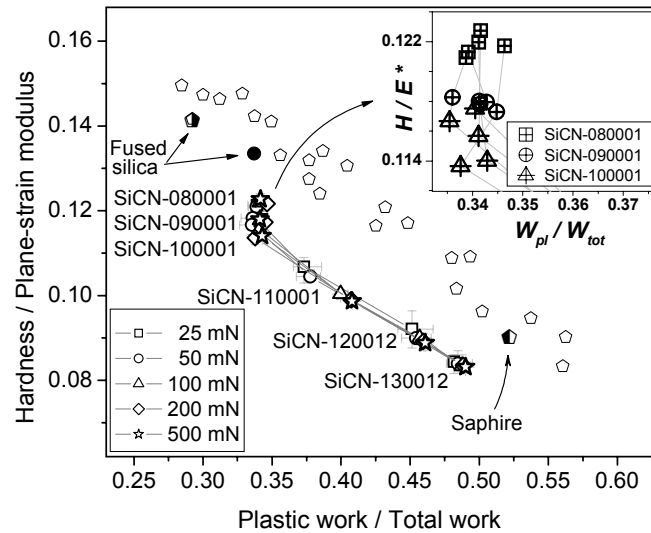


these materials. The slope of this linear correlation is identical with that reported by Cheng and Cheng [04Che] (dotted line in Fig. 5.6), expressed by the relation:

$$\frac{W_{pl}}{W_{tot}} = (1 + \gamma) \frac{h_{res}}{h_{max}} - \gamma \quad \text{for } \frac{h_{res}}{h_{max}} > 0.4 \quad \text{and } \gamma = 0.27 \quad (5.12)$$

However, the overall residual depth ratios are shifted towards lower values by 0.02 to 0.04, the higher shift corresponding to lower indentation load, or in other words, lower probing depth (further described in the next section). In contrast, the materials SiCN-090001 and SiCN-080001 do not follow the above linear correlation, due to the invariance in plastic work ratio even at increasing residual depth ratios. Relative to the linear trend observed for the other materials, this deviation is translated into enhanced elastic recovery in these materials. For comparison, the correlation data for fused silica evaluated from the P - h curve reported in [04Oli] is included in Fig. 5.6, which shows a larger residual depth ratio, while the plastic work ratio is nearly equal to that of materials SiCN-080001 through SiCN-100001. This means that the elastic recovery in fused silica is even higher than in SiCN-080001. Interpretation of these variations is further facilitated by comparing with the corresponding variations in the elastic modulus and hardness. For this purpose the ratio between the hardness and plane-strain elastic modulus, viz., H / E^* (where $E^* = E / (1 - \nu^2)$) is useful [04Che]. The evolution of H / E^* in materials SiCN-080001 through SiCN-130012 is presented in Fig 5.4(c). The H / E^* ratio decreases from 0.123 to 0.114 in materials SiCN-080001 through SiCN-100001 and further more rapidly from 0.099 to 0.083 in materials SiCN-110001 through SiCN-130012. The decrease of H / E^* in the former materials is dominated by the increase in E^* whereas in the latter materials it is controlled by the reduction in hardness. The correlation between the plastic work ratio and H / E^* is presented in Fig. 5.7. For materials SiCN-110001 through SiCN-130012, a linear correlation is observed, reinforcing the result in Fig. 5.6. The slope of this linear correlation is also in agreement with

Fig. 5.7. Correlation between the ratios W_{pl}/W_{tot} and H/E^* calculated from the load-unload cycle data from Berkovich nanoindentation of Si-C-N ceramics. The correlation data of the same ratios (half-filled pentagons: experimental data from fused silica and sapphire; open pentagons: FEM simulated data) reported in Ref. [04Che] are included for comparison. The second data point (full circle) of fused silica is derived from the $P-h$ curve reported in Ref. [04Oli]. The region covering the amorphous ceramics SiCN-080001 through SiCN-100001 is magnified in the inset for clarity.



the FEM simulated correlation data in [04Che], while the overall data are relatively shifted towards lower H/E^* values. Again, the materials SiCN-090001 and SiCN-080001 deviate from this linear correlation, and show progressively higher H/E^* ratios (due to the higher elastic recovery, leading to lower contact stiffness S and thereby, lower E^*) at constant plastic work ratio equal to that of SiCN-100001. A still higher H/E^* ratio at comparable plastic work ratio observed in fused silica (shown as full circle in Fig. 5.7) confirming its further enhanced elastic recovery. For completion, the absolute and normalized indentation work of elastic, plastic and total deformations, derived from the $P-h$ curves at 500 mN loading are presented in Fig. 5.5(d). Normalization was performed with the work quantities of SiCN-100001 material. The work quantities of fused silica were derived from the $P-h$ curve from [04Oli], duly accounting for the difference in the applied maximum loads. The normalized elastic and plastic work data for amorphous materials SiCN-100001 through SiCN-080001 and fused silica nearly overlap on a single curve, showing that the progressively increasing plastic deformation is matched by a concomitant equi-proportional increase in the elastic recovery, manifested in the invariance of plastic work ratio. The same behavior was observed for indentation at lower loads down to 25 mN. These results are suggestive of a common deformation mechanism operative in these materials. As fused silica is known to plastically deform primarily by densification [79Aro], it can

be reasoned that the plastic deformation in materials SiCN-080001 through SiCN-100001 also occurs by the same mechanism. On the other hand, the elastic and plastic work data for materials SiCN-110001 through SiCN-130012 predominantly show an anti-correlation, indicating that their deformation mechanism is different from the former materials.

5.3.5. Load / size effect on hardness

Significant influence of applied load was noted in all the measured elastic and plastic deformation parameters. The following observations were made, pertaining to the increase of load from 25 to 500 mN: (i) residual depth ratio increased uniformly in all the materials; (ii) plastic work ratio remained practically constant in materials SiCN-080001 through SiCN-100001, but increased in materials SiCN-110001 through SiCN-130012, the increase in SiCN-110001 being appreciable; (iii) hardness increased in materials SiCN-080001 through SiCN-100001, but decreased in materials SiCN-110001 through SiCN-130012, with a highest decrement in SiCN-110001 correlating with the increase in plastic work ratio; (iv) elastic modulus increased in samples SiCN-080001 through SiCN-120012, with a highest increment in SiCN-100001. These variations are relatively small compared to the inter-material variations describing material properties. However, they merit consideration from the view point of indentation size effect (ISE), and the evolution of material resistance against increasing contact stresses. From the uniform increase in the residual depth ratios, it is clear that the increase in load enhances plastic deformation in all the materials, commonly observed as the manifestation of ISE. Even so, the evolution of hardness proceeds in different directions in the amorphous (SiCN-080001 through SiCN-100001) and phase separated materials, as noted above. It is to be noted that if the observations (i)-(iv) were to be due to the tip imperfection, it should affect the behavior of all the materials in the same direction. The invariance of plastic work ratio juxtaposed with the increase in residual depth ratio at increasing loads in the former materials reveals that the increased plastic

deformation was matched by increased elastic recovery as described in the previous section. Identification of this behavior with the densification type of plastic deformation further suggests that the increase in hardness in these materials is related to densification of the material under the indenter. The decrease of hardness in the latter materials by corollary can be related to either a change or emergence of an additional plastic deformation mechanism, indicated also by the increase in plastic work ratios.

Traditionally, ISE is studied in the load range extending from nano- to microindentation regimes. To further examine the deformation behavior in the latter regime, microindentation experiments were performed using Vickers indentation at loads ranging from 0.245 to 49.05 N, and the Meyer hardness (H_M) of the materials SiCN-080001 through SiCN-130012 was evaluated according to the relation:

$$H_M = \frac{P}{2d^2} \quad (5.13)$$

where P is the indentation load and d is the half of the indentation impression

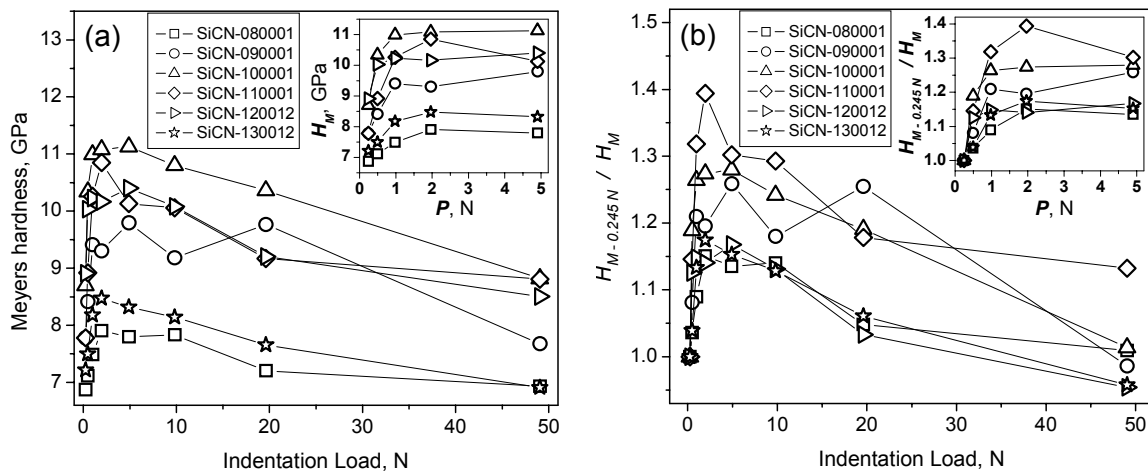


Fig. 5.8. (a) Evolution of Meyer hardness in Si-C-N ceramics, determined from Vickers microindentation at loads ranging from 0.245 N to 49.05 N; (b) Meyer hardness data in (a) normalized by the values measured at the lowest load of 0.245 N. The low load region is highlighted in the insets for visual clarity.

diagonal. The results are presented in Fig. 5.8(a). The Meyer hardness values are significantly lower than the nanoindentation hardness values as it has been usually observed for various materials in the literature [05Qia]. On the other hand, a continuous increase in H_M was observed for all the materials with increasing load in the range $0.245 \leq P \leq 4.905$ N (inset in Fig. 5.8(a)), and a continuous drop at further increasing load up to 49.05 N. For effective comparison of the variations across different materials, the H_M values at each load were normalized with the value measured at the lowest load viz., 0.245 N. The normalized data are plotted in Fig. 5.8(b). From these plots it is seen that hardness increased by a factor of 1.15, 1.19, 1.27, 1.39, 1.14 and 1.17 in the load range $0.245 \leq P \leq 2$ N for materials SiCN-080001 through SiCN-130012 respectively. (This increase is nearly nullified at still higher loads, except for SiCN-110001.) Comparing the effect of load on hardness in the nano- and microindentation experiments, two prominent differences are noted: (i) the factor of increase is appreciably higher in the latter experiments, even in the load range comparable in both nano- and microindentation, viz., between 250 – 500 mN (inset in Fig. 5.8(b)); (ii) increase in microindentation hardness is also observed in materials SiCN-110001 through SiCN-130012, in contrast to nanoindentation experiments where a decrease in hardness was registered. However, it should also be noted that the two experiments differ, primarily with respect to the load regimes as well as the employed loading rates, and secondarily with respect to the geometry of the indenter (Berkovich and Vickers) and the hardness evaluation method. The evolution of material resistance to plastic deformation depends on both of the above factors, viz., load (transformed into applied stress) via strain hardening and loading rate (transformed into strain rate) via strain rate sensitivity. These aspects are examined in the next two sections respectively.

5.3.6. Reverse analysis of $P-h$ curves

While plastic deformation is easily realized for ceramic materials under sharp indentation, evaluation of plastic deformation parameters from indentation

experiments is not as straight forward as in classical tensile or compressive loading experiments. For this reason, quantitative analysis of plastic deformation in ceramics has been elusive in the literature. The resolution of the yield point under indentation deformation is also very difficult as unlike metallic materials, no clear pop-in is generally observed during indentation of ceramics and silicate glasses [92Oli, 04Li]. At best, yield stress for such materials can be visualized based on the deviation from elastic behavior in spherical indentation experiments, where relations for transforming indentation stress and strain into equivalent uniaxial stress and strain quantities are available [01Her]. This is also facilitated experimentally as by choosing an appropriate indenter radius, practically resolvable region of pure elastic deformation can be realized. For sharp indentation, the problem of defining the stress and strain quantities beyond elastic limit is circumvented using the concept of representative stress and strain. Based on indentation experiments on metals [96Tab], Tabor defined the uniaxial flow stress σ_0 for sharp indentation in terms of hardness using the above concept as

$$H = 3\sigma_0 \approx 3\sigma_y \quad (5.14)$$

where σ_0 is realized for a Vickers indenter at a representative strain (ε_0) of 0.08 to 0.1. Using dimensional analysis however, Cheng and Cheng found that H/σ_y is not a linear function of σ_y/E for work hardening materials, but H/σ_0 (where $\sigma_0 = K\varepsilon_0^n$ with $\varepsilon_0 = 0.1$, $n =$ work hardening exponent) is approximately linear with σ_y/E [04Che]. Thus, due to the dependence of flow stress and thereby hardness on elastic modulus and work hardening exponent, it is evident that the estimation of yield stress from the Tabor's one-third rule $\sigma_y \approx H/3$ is too simplistic. Several procedures have been proposed in the literature for the determination of plastic deformation parameters σ_y and n for power-law work hardening materials, from the reverse analysis of indentation $P-h$ curves based on FEM simulations, dimensional analysis and empirical relationships [99Gia, 01Zen, 02Xu, 99Kna]. The uniqueness of the solutions derived from such procedures is also under

active discussion; for example, Cheng and Cheng showed by FEM simulation and dimensional analysis that more than one combination of σ_y and n can reproduce a given P - h curve by forward analysis [04Che]. However, the same authors have derived an approximate relationship using dimensional analysis and FEM simulation to estimate σ_y from the P - h loading curve, for elastic-perfect plastic ($n = 0$) materials [98Che]. It is frequently proposed in the literature that plastic deformation in ceramic materials can be treated according to the latter model [99Kna, 06Zha]. In the absence of a unique consensus on the constitutive model for the plastic deformation in ceramics, the plastic deformation of the present Si-C-N materials are examined here according to both the models, *viz.*, elastic-perfect plastic and elastic-power law work hardening behaviors. This approach allows to the least, in deriving a qualitative understanding of the deformation behavior as a whole, and also in probing the variations in behavior in the range of materials being investigated.

Accordingly, the yield stresses of the materials SiCN-080001 through SiCN-130012 were evaluated assuming elastic-perfect plastic behavior in the first step, and using the relation derived by Cheng and Cheng [98Che]:

$$\Pi[\sigma_y / E] = P(1 - \nu^2) / Eh^2 \quad := X \quad (5.15a)$$

adopted in the form

$$\begin{aligned} \sigma_y / E = f[X] = & 0.0141X + 0.0229X^2 - 0.0758X^3 \\ & + 0.1598X^4 - 0.1248X^5 + 0.0374X^6 \end{aligned} \quad (5.15b)$$

The polynomial at the right hand side of Eq. 5.15b was obtained from the least square fitting of the data plot in Fig. 3 of Ref. [98Che]. The deviation of the loading curves from the square dependence (of h to P) due to tip imperfection was accounted for, by replacing the term P/h^2 in Eq. 5.15a with the quadratic coefficient c_0 from Eq. 5.2. The values of σ_y evaluated using Eq. 5.15b with E

values derived from the Oliver-Pharr analysis are presented in Fig. 5.9. The evolution of σ_y with respect to different materials scaled with hardness, with the ratio H/σ_y varying from 1.7 to 2.0 for materials SiCN-080001 through SiCN-130012 respectively. Additionally, the σ_y values showed nearly similar increasing (or decreasing) trend as hardness, even after correcting for the tip shape imperfection. (Note that the hardness values were obtained after taking into account the actual indenter shape via the calibrated area function; section 5.3.2.) The same increasing trend was observed when σ_y values were separately estimated using progressively increasing fractions of the 500 mN loading curves and with $P/h^2 = c_0$. Cheng *et al.* concluded from FEM analysis that the tip imperfection does not affect the σ_y estimates from the above procedure for $h/R_{Berk} < 1$ [98Che]. As this limit is exceeded for all the materials for loads above 25 mN, the increase in σ_y at higher applied loads is suggestive of deviation from the assumed perfect plastic behavior.

In order to examine the applicability of power law work hardening model to the plastic deformation behavior of the present materials, the semi-empirical approach proposed by Zeng and Chiu was adopted [01Zen]. The choice for this method was based on the following reasons: (i) the method is simple to apply (ii) although being semi-empirical in nature, its formulation is based on key relationships derived from theoretical and finite element modeling (iii) it is one of the few methods available in the literature that leads to an estimate of both yield stress and work hardening exponent (iv) in

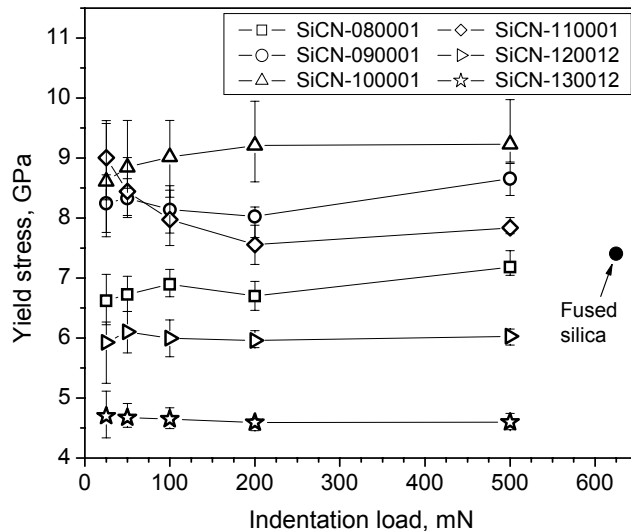


Fig. 5.9. Evolution of yield stress in Si-C-N ceramics, evaluated using the relation $\Pi[\sigma_y/E] = P(1-\nu^2)/Eh^2$ derived from FEM simulation in Ref. [98Che], assuming elastic-perfect plastic behavior. Data in full circle represents yield stress evaluated for fused silica.

its original presentation, this method has been tested on a range of materials with reasonable estimates of material parameters. A detailed description of the formulation and application methodology is found in Ref. [01Zen]. In brief, the method is based on describing the indentation P - h curves by the following equations:

For the loading curve:

$$P = \frac{1.273}{(\tan 24.7^\circ)^2} \left(1 + \frac{\sigma_u}{\sigma_y} \right) \left(1 + \ln \frac{E \tan 24.7^\circ}{3\sigma_y} \right) \sigma_y h^2 \quad (5.16)$$

For the unloading curve:

$$P = (1 - \phi) f[\nu] E h^2 + \phi S (h - h_0) \quad (5.17)$$

Eq. 5.16 is obtained from the finite element analysis of the loading curve from Berkovich indentation for an elastic plastic material, where σ_u is the stress at a representative strain (ε_u) of 0.29. Eq. 5.17 is formulated as a linear combination of unloading curve equations applicable for respectively a perfect elastic material and an elastic– perfect plastic material, expressed as:

$$P = f[\nu] E h^2 = 2.189(1 - 0.21\nu - 0.01\nu^2 - 0.41\nu^3) \frac{E}{1 - \nu^2} h^2 \quad (5.18)$$

$$P = S(h - h_0) = 2\sqrt{\frac{24.56}{\pi}} \frac{E}{1 - \nu^2} h_0 (h - h_0) \quad (5.19)$$

This empirical formulation is based on the common observation that experimental unloading curves of most materials are enclosed between these two extreme

behaviors. While Eq. 5.18 is derived from the FEM solution of the elastic Berkovich indentation, Eq. 5.19 is from the Doerner-Nix approximation of the unloading curve that fits well for elastic-perfect plastic materials [86Doe]. The weight factors $(1-\phi)$ and ϕ in Eq. 5.17 represent respectively the fractions of elastic and elastic-perfect plastic responses composing the unloading curve. The parameter ϕ is further modeled to represent the ratio σ_y/σ_u , termed as the strain hardening parameter. The values of E , σ_u , σ_y and h_0 are estimated from the non-linear curve fitting of the unloading and loading curves using bounded fitting parameters according to Eq. 5.17 and Eq. 5.16. The power law work hardening exponent n is estimated using the relation:

$$n = \frac{\ln(\sigma_u/\sigma_y)}{\ln(\varepsilon_u/\varepsilon_y)} \quad (5.20)$$

where $\varepsilon_y = \sigma_y / E$. Treating the parameter h_0 as analogous to the plastic penetration depth h_p , the ‘perfect plastic hardness’ (H_{pl}) is defined as

$$H_{pl} = P_{max} / 24.56h_0^2 \quad (5.21)$$

The above method was applied to estimate the plastic deformation parameters of materials SiCN-080001 through SiCN-130012. For comparison purpose, the analysis was also applied on the P - h data of fused silica adopted from [04Oii]. For the unloading curve fitting, only the first 50% of the data was used as recommended in [01Zen]. The representative unloading curve-fits for materials SiCN-080001 through SiCN-130012 as well as for fused silica are depicted along with the raw data in Fig. 5.10(a). The fitted curves truly represent the first 50 to 90% of the raw data, the deviation increasing in the sequence: fused silica, SiCN-080001 and SiCN-130012. A closer inspection reveals that the deviation is due to the rapid increase in the elastic recovery in the last part of the unloading curves. Note that such a rapid increase in curvature is observed even in the unloading curves of materials that display elastic- perfect plastic behavior

[98Che, 01Zen], where the region of higher curvature is shifted to lower portions of the unloading curve for lower σ_y / E ratios. Obviously the semi-empirical linear combination model used here is incapable of completely capturing the entire unloading curves, mainly because the change in the shape of unloading curve due to a progressive change in the material behavior from elastic- perfect plastic to pure elastic behavior does not manifest uniformly throughout the entire unloading curve. Also, the deviating fraction of unloading curve was unrelated to specific dimensions of the indenter displacement as suggested in [01Zen], but remained nearly fixed at all applied loads from 25 mN to 500 mN.

The elastic and plastic material parameters estimated from the application of the procedure are compiled in Fig 5.10(b). The evolution of the elastic moduli displays an identical trend with that of Oliver-Pharr results, but the magnitudes are lower by ~18 to 22%. This can be understood from the difference in the method of determining the unloading contact stiffness (S), which in the Zeng procedure is derived from a constrained curve fitting, whereas the derivative of a constraint-free fitted unloading curve at P_{max} is used in the Oliver-

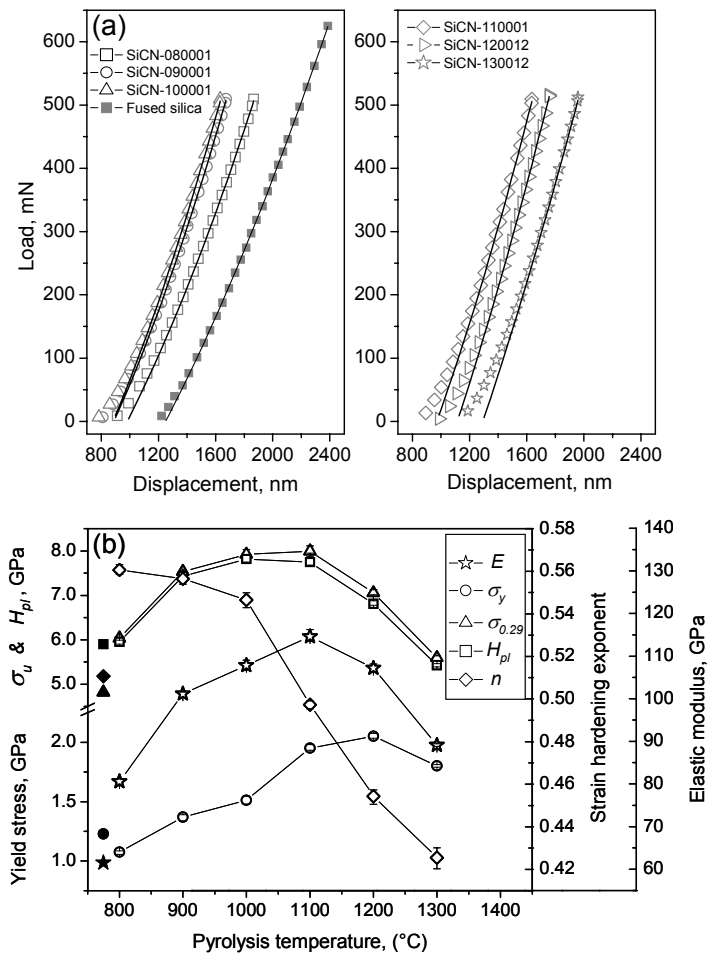


Fig. 5.10. Semi-empirical reverse analysis of nanoindentation load-unload P - h curves according to Ref. [01Zen]. (a) plots of unloading curves (at $P_{max} = 500$ mN) and curve-fits using Eq. 5.17. (b) evolution of the parameters E , σ_y , σ_u , n and H_{pl} determined from the analysis.

Pharr method [92Oli]. The parameters of most interest are the yield stress (σ_y) and the strain hardening exponent (n). The estimated σ_y values are appreciably lower than those derived based on the elastic- perfect plastic assumption (see Fig. 5.9), and increase from 1.1 GPa to 2 GPa for materials SiCN-080001 through SiCN-120012 respectively, and slightly decrease to 1.8 GPa in SiCN-130012. The corresponding strain hardening exponents were high around 0.5, (as against $n = 0$ assumed in the previous case) decreasing from 0.56 to 0.42. The variation in n for amorphous materials SiCN-080001 through SiCN-100001 was relatively small, ranging from 0.56 to 0.54 but decreased appreciably from 0.49 to 0.42 in materials SiCN-110001 through SiCN-130012. These estimates grossly compare well with the evolution of Meyers hardness at increasing loads and suggest that the amorphous materials display a higher strain hardening tendency than the phase separated materials, although the latter materials also show significant strain hardening, as observed from both the evaluations. In comparison to the amorphous Si-C-N materials, fused silica showed a yield stress value of 1.25 GPa and a strain hardening exponent of 0.51. As Eq. 5.16 is based on the square dependence $P \propto h^2$, deviations from this requirement can influence the parameter estimates. Accordingly, the results presented here correspond to the $P-h$ data from 500 mN loading that show the least deviation from the square dependence. However, the same evaluation procedure applied to the data from lower loads showed an identical trend across different materials as presented here, with small variations in actual magnitudes. This indicates that irrespective of its validity to the real behavior, the deformation behavior predicted by the semi-empirical analysis was not influenced by the change in applied load.

5.3.7. Analysis of Indentation creep deformation at constant loading

In order to eliminate the adverse influence of viscoelastic deformation in the determination of unloading contact stiffness, a constant load hold segment is usually included between the loading and unloading cycles of nanoindentation

measurements. For ceramic materials comparable to fused silica, the recommended hold time is around 10 s [01Chu] as has been used in the present study. An examination of the hold segment data recorded from the Berkovich indentation of Si-C-N materials revealed significant creep displacements, while the absolute magnitudes showed dependency on the material structure. On the other hand, no hold-time displacement was observed in the spherical indentation measurements performed in the elastic contact regime, even after accounting for the reduced contact pressures realized in the latter experiments. This suggests that the observed hold-time displacements originated from plastic creep deformation rather than from viscoelastic deformation. The creep displacement (h) – time (t) data for the materials SiCN-080001 through SiCN-130012 are presented in Fig. 5.11. For visual clarity, only the data recorded at $P_{hold} = 25$ mN and 500 mN are shown. The plots represent the averaged data from at least five individual measurements after discarding the data that showed large deviations from the average behavior. To facilitate comparison of the displacement magnitudes the initial h and t coordinates of all the curves have been aligned to zero. A general examination further showed that the overall magnitude of creep displacements roughly scaled in inverse proportion with the material hardness. While the increase in the displacements decelerated with time for all materials, harder materials showed tendency towards stability at the end of hold period, whereas the softer materials showed a steady linear increase up to the end. Independent of the

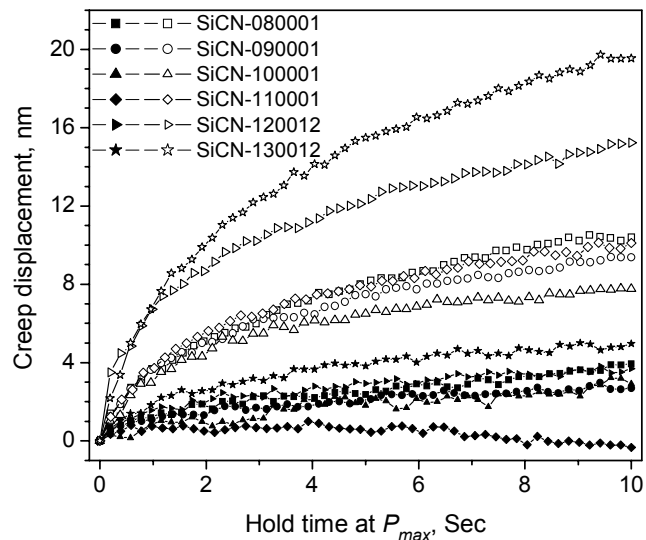


Fig. 5.11. Plots of hold-time creep displacement from Berkovich nanoindentation of Si-C-N ceramics. Closed and open symbols represent data from constant load hold segments at $P_{hold} = 25$ mN and $P_{hold} = 500$ mN respectively. The initial time and displacement values of the raw data curves are aligned to zero to facilitate comparison of creep magnitudes.

above observation, the rate of change of displacement (strain rate) showed significant sensitivity to the applied load. As the hold-time displacement leads to lower hardness values, any sensitivity of the displacement to the applied load will obviously influence the measured hardness values, indicating that the strain rate sensitivity is a potential factor to be considered with respect to the evolution of hardness at increasing loads. Notably, the influence of strain rate on ISE in silicate glasses has been studied [98Gra]. Strain rate sensitivity (m) can be accessed via the general flow equation

$$\sigma = b\dot{\epsilon}^m \quad (5.22)$$

where σ is the flow stress, and $\dot{\epsilon}$ is the strain rate. For indentation deformation, the flow equation is adopted in the form

$$H = b\dot{\epsilon}^m \quad (5.23)$$

by setting hardness (H) equal to the flow stress (σ) and using the indentation strain rate relation

$$\dot{\epsilon} = \frac{\dot{h}}{h} = \frac{dh/dt}{h} \quad (5.24)$$

where h is the instantaneous indenter displacement and t is the time. The flow equation for indentation deformation can also be expressed in terms of the creep or stress exponent (s) as:

$$\dot{\epsilon} = k\sigma^s \equiv kH^s \quad (5.25)$$

Evidently, the strain rate sensitivity and the stress exponent have a reciprocal relationship, $m = 1/s$. The analysis of strain rate sensitivity can be carried out under various loading schemes, namely, constant loading rate ($\dot{P} = \text{constant}$), constant indentation rate ($\dot{h} = \text{constant}$), constant strain rate ($\dot{\epsilon} = \text{constant}$) and constant load ($P = \text{constant}$). Compared to other schemes, the constant load

scheme is experimentally easy to achieve. For our purposes, it is convenient to use the $h - t$ data from the constant load hold segment for analyzing the influence of strain rate on the plastic deformation behavior.

For convenient mathematical analysis, the averaged $h - t$ raw data were curve fitted according to the following empirical equation:

$$h = h_{t_0} + \alpha_1 t + \alpha_2 t^q \quad (5.26)$$

which was found to satisfactorily describe the raw data with correlation coefficients above 0.99. The evolution of strain rates at $0 \leq t_{hold} \leq 10$ s were evaluated from these fitted data using Eq. 5.24. Assuming that the ratio of contact depth and maximum depth (h_c/h_{max}) remains constant and equal to the value at $t_{hold} = 0$ during the hold segment, the new contact depths at increasing hold time $0 \leq t_{hold} \leq 10$ s were evaluated as:

$$h_c|_{t_{hold}=t} = h_{max}|_{t_{hold}=t} \left(\frac{h_c|_{t_{hold}=0}}{h_{max}|_{t_{hold}=0}} \right) \quad (5.27)$$

The evolution of hardness at $0 \leq t_{hold} \leq 10$ s were evaluated from the contact depths determined as above, using the calibrated area function and Eq. 5.8. The strain rate ($\dot{\varepsilon}$) – hardness (H) data as obtained above for $25 \leq P_{hold} \leq 500$ mN from materials SiCN-080001 through SiCN-130012 are plotted in log-log coordinates in Fig. 5.12(a-f). The evolution of the stress exponent (s) at increasing t_{hold} can be evaluated from the instantaneous slopes of the log-log curves, according to Eq. 5.25. It is seen from Fig. 5.12(a-f) that the stress exponents decrease from their initially high values at the start of the hold period where $\dot{\varepsilon} \geq 3 \times 10^{-3} \text{ s}^{-1}$, to a near steady state value in the strain rate window $3 \times 10^{-3} \text{ s}^{-1} \geq \dot{\varepsilon} \geq 3 \times 10^{-4} \text{ s}^{-1}$, and further tend to increase asymptotically to infinity for $\dot{\varepsilon} \leq 3 \times 10^{-4} \text{ s}^{-1}$ as $t_{hold} \rightarrow t_{hold-max} = 10$ s. The inflexion towards the latter stage was just begun in amorphous materials SiCN-080001 through SiCN-100001 for $P_{hold} = 25$ mN, whereas the asymptotic increase had progressed to various higher

extents in other materials or at higher loads, depending on the hardness of the respective materials. Interestingly, the region of steady state stress exponent is

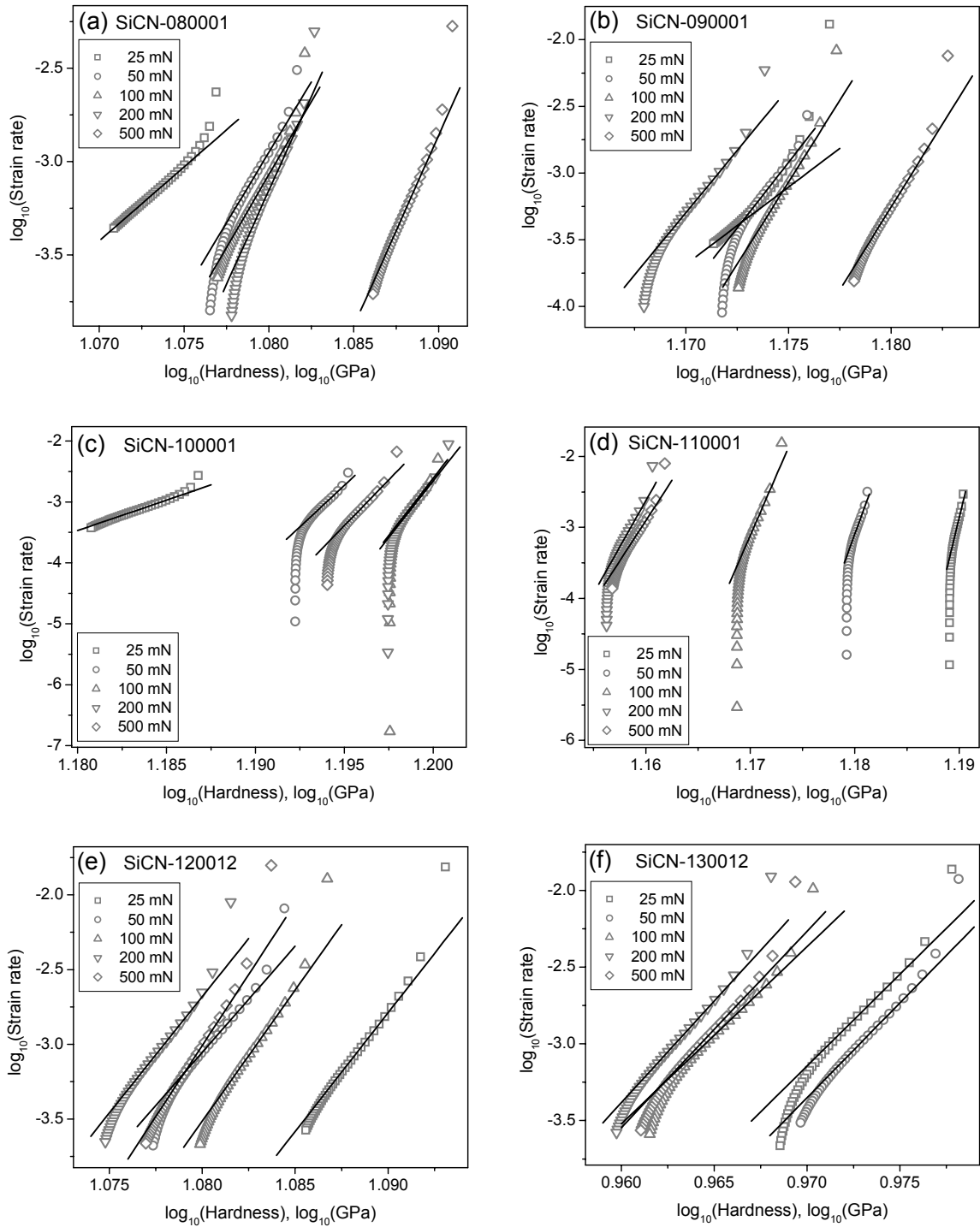


Fig. 5.12. log-log plots of hardness against creep strain rates evaluated from the P - h_{hold} - t_{hold} data from the constant load hold segment ($t_{hold-max} = 10$ s) of Berkovich nanoindentation of Si-C-N ceramics.

roughly the same, and corresponds to the strain rate window $3 \times 10^{-3} \text{ s}^{-1} \geq \dot{\epsilon} \geq 3 \times 10^{-4} \text{ s}^{-1}$ in all the materials. The steady state stress exponents derived from the linear portion of the $\log(\dot{\epsilon}) - \log(H)$ plots for $25 \leq P_{hold} \leq 500 \text{ mN}$ in materials SiCN-080001 through SiCN-130012 are summarized in Fig. 5.13(a). The corresponding values of strain rate sensitivity evaluated as $m = 1/s$ are shown in Fig. 5.13(b). The values of m and s for amorphous materials SiCN-080001 through SiCN-100001 showed clear load dependencies (the stress exponents increased and the strain rate sensitivities decreased with increasing applied load, P_{hold}) whereas the effect was relatively negligible in the phase separated materials SiCN-120012 and SiCN-130012 as seen in Fig. 5.13(a) and Fig. 5.13(b). Remarkably, the observed load dependency in material SiCN-110001 was diametrically opposite to those of materials SiCN-080001 through SiCN-100001. Apart from the load dependency, m and s also showed variation across the range of materials, evident from the values derived for $P_{hold} \geq 50 \text{ mN}$. Comparing the values derived at $P_{hold} = 500 \text{ mN}$, the stress exponent progressively increased (m decreased) from 204 ($m = 4.9 \times 10^{-3}$) to 300 ($m = 3.3 \times 10^{-3}$) in materials SiCN-080001 through SiCN-100001 and decreased (m increased) from 227 ($m = 4.4 \times 10^{-3}$) to 127 ($m = 7.8 \times 10^{-3}$) in materials SiCN-110001 through SiCN-130012 respectively.

The evolution of the stress exponents during creep deformation and the observed

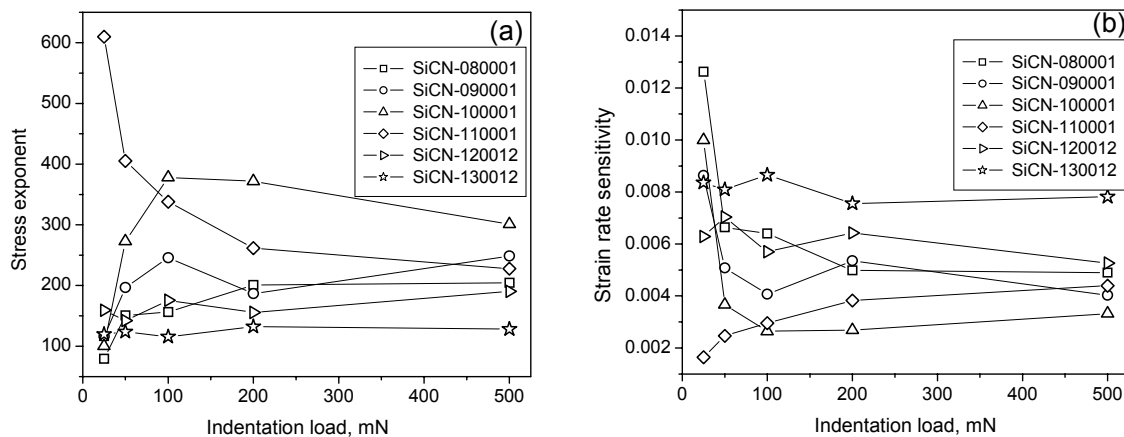


Fig. 5.13. Evolution of (a) stress exponent and (b) strain rate sensitivity, determined from the linear portion of the $\log(\text{hardness}) - \log(\text{creep strain rate})$ plots in Fig. 5.12.

load dependency for amorphous materials SiCN-080001 through SiCN-100001 are in close comparison with the behavior of fused silica reported by Li and Ngan [04Li]. (The stress exponents evaluated using the relation: contact flow stress (σ) = P/h^2 instead of $\sigma = H$ as above also yielded nearly identical values within numerical error.) However, the values of stress exponents are significantly higher than those of fused silica for comparable applied loads ($50 \leq s \leq 80$ for $16 \text{ mN} \leq P_{hold} \leq 64 \text{ mN}$, compare Fig. 5.13(a) with Fig. 12 reported in Ref. [04Li]). Also, the region of steady state exponent in fused silica is apparently realized at relatively lower strain rates ($\dot{\epsilon} \leq 2 \times 10^{-4} \text{ s}^{-1}$, inferred from Fig. 10 and 11 in Ref. [04Li]) than in materials SiCN-080001 through SiCN-130012. These observations suggest that the evolution of material resistance to creep (or plastic) deformation in the present Si-C-N materials is quantitatively different than in fused silica. The derived strain rate sensitivity values of the present materials were also lower than that of soda-lime glass by an order of magnitude ($m \geq 20 \times 10^{-3}$) [90Han, 93Keu, 98Gra], but showed an excellent agreement with the strain rate sensitivities determined for amorphous hydrogenated diamond-like-carbon (*a*-DLC:H or *a*-DLC, $1.8 \times 10^{-3} \leq m \leq 4.6 \times 10^{-3}$) and amorphous hydrogenated carbon nitride (*a*-CN_x:H or *a*-CN_x, $4 \times 10^{-3} \leq m \leq 10 \times 10^{-3}$) films [00Tan, 01Ohk]. Specifically, it was reported that a decrease in the hydrogen termination in *a*-C:H and *a*-CN_x:H films led to a decrease in *m*, while a progressive formation and organization of *sp*² carbon into graphitic clusters in DLC:H and *a*-DLC:N:H led to an increase in *m* [00Tan]. Remarkably, the effect of both dehydrogenation and graphitic segregation are manifested in the variation of *m* in the amorphous and phase segregated materials as seen above.

5.3.8. Pile-up and sink-in behavior

In order to examine the manifestation of plastic deformation and the strain hardening characteristics on the transport of the deformed material around the indenter, AFM topographic imaging of the residual indentation impressions were carried out. The residual impressions from Vickers indentation at $P = 4.905 \text{ N}$

were chosen for this purpose as they have the potential of exhibiting the maximum effect due to the high loads employed. Note that the increase in Meyer hardness reached saturation at this load (see Fig. 5.8). The recorded images of indents from materials SiCN-080001, SiCN-110001, SiCN-120012 and SiCN-130012 are depicted in Fig 5.14. The images show pile-up of deformed material around the indent impressions in the amorphous materials SiCN-080001 and SiCN-110001, with the magnitude being appreciably higher in the former as evident from the section analysis. Except at the inner core, the impression surfaces were nearly smooth, devoid of any shear faults. (The smaller irregular features are artifacts replicating the surface imperfections on the indenter surface.) Fine symmetrical steps resembling shear faults were observed at the

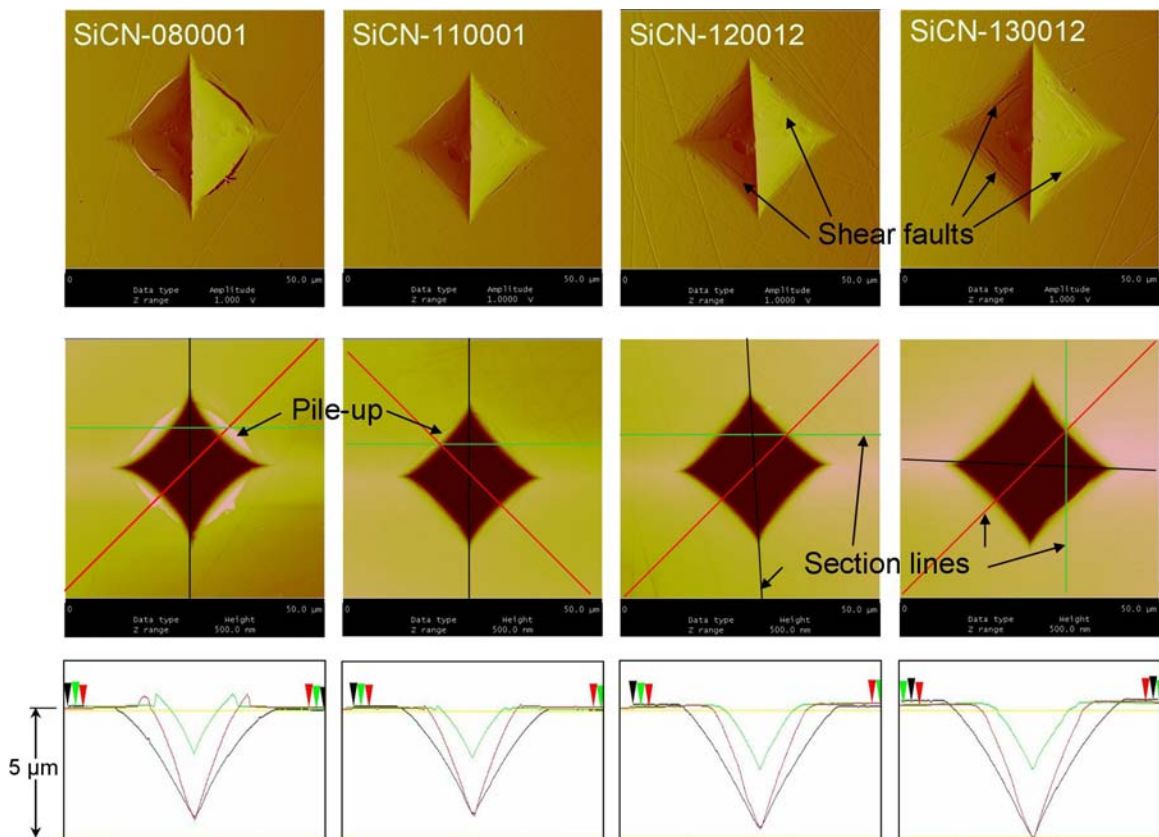


Fig. 5.14. Tapping mode AFM topographic images of Vickers micro-indents in SiCN-080001, SiCN-110001, SiCN-120012 and SiCN-130012 showing features of plastic deformation. Illustrations in the first, second and third rows are from amplitude contrast imaging, height contrast imaging and sectional analysis of height contrast images respectively. Width of the images = 50 μm .

impression core for both materials, which were well defined in SiCN-080001 than in SiCN-110001. While no pile-up at the impression edge was observed in the phase separated materials SiCN-120012 and SiCN-130012, irregular shaped shear faults appeared at the impression surface, their number density increasing from SiCN-120012 to SiCN-130012. From the height contrast images, it is evident that the edge curvature of the impression cavities progressively decreased (leading to the transition from a pin-cushion shape towards a regular square) in materials SiCN-080001 through SiCN-130012. This shape change is irrespective of piling up but indicates that the elastic recovery in the materials decreased in the same order. This is also in agreement with the progressive increase in the ratio h_{res}/h_{max} from the nanoindentation measurements of these materials. On the other hand, the appearance of pile-up in materials SiCN-080001 and SiCN-110001 is suggestive of perfect-plastic deformation behavior, at least at the moment when the pile-ups were formed. The absence of pile-up for materials SiCN-120012 and SiCN-130012 implies either a change in yielding and strain hardening character in these materials, or a change in the friction character of the indenter-impression interface.

5.4. Discussion

A first hand comparison of the determined elastic moduli and hardness from the present nanoindentation analysis shows that the quantities are in agreement with the range of E and H values reported for precursor-derived Si-C-O ($50 \text{ GPa} \leq E \leq 130 \text{ GPa}$; $4 \text{ GPa} \leq H \leq 9 \text{ GPa}$;) [02Wal], Si-C ($H \approx 12 \text{ GPa}$) [03Mor], Si-C-N ($E \approx 120 \text{ GPa}$, $H \approx 13 \text{ GPa}$) [01Gal] and a-CN_x:H ($110 \text{ GPa} \leq E \leq 170 \text{ GPa}$; $6 \text{ GPa} \leq H \leq 12 \text{ GPa}$;) [00Tan, 01Ohk] materials, determined from various experimental techniques. The evolution of E and H also correlate well with the structural evolution across the range of investigated materials. As mentioned in section 5.2, the latter was effected by changing the degree of polymer-to-ceramic transformation by progressively increasing the final pyrolysis temperature from 800°C to 1300°C. Accordingly, while the materials SiCN-080001 through

SiCN-100001 possess an electron-amorphous structure, progressively increasing network connectivity in the amorphous structure is realized due to the progressive stripping of one-fold coordinated hydrogen from the initial Si-C-N-H network in these materials [07Jan]. This transformation leads to an increase in the network density and rigidity [96Boo] and thereby, an increased resistance to deformation manifested in the E and H values. The effect of dehydrogenation in improving the mechanical properties of tetrahedrally coordinated amorphous carbon has been well documented [00Tan, 01Ohk], and has also been reported with respect to precursor-derived Si-C-O ceramics [02Wal]. With the further increase in pyrolysis temperature above 1100°C, a progressive phase separation and organization of turbostratic graphite (TG) is realized in the present Si-C-N ceramics, the materials SiCN-120012 and SiCN-130012 falling in this category (Chapter 2) [07Jan]. Due to the lower density and deformation resistance intrinsic to the TG phase, combined with a weakening effect in disrupting the continuous Si-C-N tetrahedral network, the latter materials display a progressive drop in the mechanical properties, again reflected in the presently determined E and H values. The effect of the precipitation of sp^2 graphitic carbon within a sp^3 tetrahedral carbon network in lowering the mechanical properties has also been shown in the literature [01Ohk, 01Iwa]. The material SiCN-110001 – although being electron-amorphous [07Jan] – lies in the borderline between the electron-amorphous and phase-separated material categories, which is responsible for the peculiar inflexions in its mechanical behavior observed in sections 5.3.2 through 5.3.7. In fact, nucleation and organization of sp^2 - hybridized carbon is observed in the present materials pyrolyzed at 800°C upwards. Thus, it is clear that the influence of the graphitic phase becomes effective only above a critical size of its organization within the Si-C-N matrix, which is just reached in the material SiCN-110001.

The elastic moduli derived from nanoindentation show significant deviations from the mean elastic moduli of the whole specimens determined from the resonance frequency testing. However, as the moduli determined independently from

spherical and Berkovich indentation analyses agree well with each other, it can be reasoned that the elastic properties in the layer of nanoindentation measurements are truly determined and nearly invariant. Thus, the observed deviation of the local properties from the bulk elastic behavior must originate either from a gradient in the material properties across the specimen cross section, arising from a compositional or structural gradient, or from the presence of residual stresses, or from a combination of both effects. Also, it is noted that the deviations are in different directions for amorphous and phase separated materials. This observation additionally suggests that the evolution of the gradients at increasing degree of ceramization showed an inflexion. Development of structural and stress gradients can be expected from the special nature of the PDC synthesis, where a differential precursor-to-ceramic transformation across the material bulk inevitably occurs due to the constraints imposed by the sample dimensions on the pyrolytic effluents and transformation induced shrinkage [02Wal, 07Jan]. Evaluation of the nature and magnitude of these gradients is an involving task in itself and offers scope for future investigation. However, since the presently observed deviations are limited to ~10% spread over the entire specimen bulk, and as the nanoindentation measurements offer the advantage of probing the local mechanical properties ($h_{max} \ll 0.01w$, w = specimen thickness), the present efforts are restricted to the understanding of the properties from the local material behavior.

From the analysis of P - h load-unload cycle, it is found that the elastic and plastic deformations in amorphous materials SiCN-080001 through SiCN-100001 evolve in a fixed proportion, approximately equal to that in fused silica. This proportion, quantified in terms of the plastic work ratio (W_{pl} / W_{tot}) displays an approximately constant value of 0.34 for all the above four materials. This value represents one of the lowest among the experimentally recorded plastic work ratios for fully developed plastic contacts, and signifies the high elastic recovery observed in these materials. Along with the anomalous densification behavior [68Nee, 79Aro, 05Yos], the high elastic recovery in fused silica is well documented [92Oli,

[04Che, 06Tan]. On the other hand, the anomalous character of materials SiCN-080001 through SiCN-100001 has been recently confirmed from the typical indentation crack patterns and the evaluated low residual contact stresses [04Bur]. Thus, it seems that a low plastic work ratio is characteristic of materials that undergo pronounced densification under the indenter. A significant increase in the hardness of the amorphous materials SiCN-080001 through SiCN-100001 is also found at increasing indentation load, while the plastic work ratio remains constant at the above low value, even when the residual depth ratio increases. Notably, a similar invariance of the plastic work ratio at increasing residual depth ratio has been reported for fused silica. (Fig. 7 in Ref. [06Tan]) Recently, Perriot *et al.* showed using diamond anvil cell (DAC) experiments, Raman microspectroscopy and FE calculations that indentation induced densification in fused silica leads to strain hardening [06Per]. Thus, it is evident that the observed indentation deformation behavior of materials SiCN-080001 through SiCN-100001 and fused silica has implications on ISE and strain hardening, and is related to their densifying type of plastic deformation. In materials capable of densification, the enhancement of plastic deformation at increasing applied loads (or ISE, tending to lower hardness) and the concomitant evolution of strain hardening compete with each other in determining the material resistance to deformation. This can explain the near invariance of hardness of fused silica and the small but significant increase of nanoindentation hardness in the above amorphous Si-C-N materials. Yoshida *et al.* experimentally evaluated the relative fractions of densification and shear flow during nanoindentation of silicate glasses including fused silica, where a decrease in the fraction of densification was observed at increasing loads [05Yos]. Noting that fused silica strain-hardens during densification, it is understandable that a progressive plastic deformation by densification at increasing loads will also simultaneously reduce the capability of the deformed material for further densification. At saturation density this deformed material will be expected to behave in a 'normal' manner, i.e., deform further by shear flow. This is indeed observed in the case of materials SiCN-080001 and SiCN-110001, evident in Fig 5.14.

While strain hardening reasonably explains the evolution of hardness in the amorphous materials SiCN-080001 through SiCN-100001, the decrease of hardness at higher loads in the phase separated materials SiCN-120012 and SiCN-130012 reveals that the enhancement of plasticity at higher loads leading to ISE dominates over the strain hardening effect, due to the emergence of additional plastic deformation mechanisms. A microstructural examination shows that the latter is effected by the shear deformation of the graphitic phase in these materials. A similar influence of the graphitic precipitation on the strain hardening characteristics of glass-like carbons was reported by Iwashita [01Iwa]. However, the persistence of densification deformation in promoting strain hardening in these materials is revealed in the microindentation analysis, in spite of the effect of the graphitic precipitation. Evidently, this contribution arises from the amorphous Si-C-N matrix phase.

Although the above discussion provides a qualitative understanding of the evolution of plastic deformation, a precise quantification of the yield stress and strain hardening parameter (n) is more challenging. The results from the reverse analysis of nanoindentation data according to both models – elastic-perfect plastic and power-law strain hardening behavior – describe the overall evolution of resistance to plastic flow across the range of the investigated materials. However, the determined values of σ_y and n are apparently different from the real material quantities. Firstly, the yield stress estimates according to the elastic-perfect plastic model display load dependence, revealing that the assumption is not wholly tenable. This conclusion is also supported by the evolution of nano- and microindentation values with increasing load. Secondly, the yield stress estimates from the semi-empirical analysis according to the power-law strain hardening model are ostensibly low, evident from the absence of any yielding during the spherical indentation experiments, in spite of the high (by a factor of two) mean contact pressures realized at maximum load. It can be reasonably expected that the real quantities are intermediate to the above two

estimates. Nevertheless, the semi-empirical analysis qualitatively captures the variation in the strain hardening behavior across amorphous and phase segregated materials, in agreement with the microindentation results.

The difference in the magnitude of strain hardening observed in the nano- and microindentation experiments underline the effect of strain rate in controlling the ISE. In agreement with the results of hold-creep experiments on fused silica reported by Li and Ngan [04Li], the amorphous materials SiCN-080001 through SiCN-100001 display a load (or size) effect on the evolution of stress exponent, where s is found to increase with applied load. The observation that only the amorphous materials display this load effect indicates that the behavior is again related to the densifying mode of plastic deformation similar to fused silica. However, the behavior of fused silica in the load range employed in the present study is unavailable for comparison. In contrast to the nanoindentation regime, the influence of strain hardening on hardness and stress exponent should be substantial at microindentation regime, as indicated by the microindentation results from the present amorphous Si-C-N materials.

While the applied load influenced the stress exponent (or the strain rate sensitivity) via densification induced strain hardening, the values of s and m corresponding to each individual material are determined by its microstructure and can be well described using the cluster model discussed in [01Ohk]. According to this model, the disruptions in the otherwise continuous amorphous Si-C-N network, arising from hydrogen terminated regions, phase separated TG and nanocrystalline SiC (n-SiC) are visualized to separate the bulk of the material into a collection of clusters. An increase in the number density of clusters promotes material flow during creep deformation, due to the increased freedom of movement of the cluster regions. From the evaluated m values for amorphous and phase segregated Si-C-N materials, it is seen that the phase segregated TG and n-SiC are more effective in increasing the value of m than the disruptions of the network due to hydrogen termination. The load dependent increase in the

stress exponent is most effective in SiCN-100001, which is also the material composed of least disruptions in the amorphous network in the sense of the cluster model. (Again, in spite of the formation of sp^2 carbon starting from material SiCN-080001, the effectiveness of such precipitates to qualify as a cluster seems to require attainment of a critical size.) This observation confirms that the load dependent increase of s in the investigated materials is solely due to the densification deformation. The remarkably inverted load dependency of the strain rate sensitivity displayed by SiCN-110001 may suggest that the sub-critical clusters of TG are 'activated' only at high enough loads.

Finally, it has to be mentioned that the understanding of the deformation behavior of the present Si-C-N materials developed above are partly shadowed by the unknown influence of phase and / or residual stress gradients. Two potential manifestations of this influence are (i) the deviations between the elastic moduli estimated from nanoindentation and resonance frequency testing (ii) the deviations of the linear correlations from the FEM predicted behavior. While the latter observation can be due to the incapability of FEM modeling in capturing the true material behavior, an agreement with the predicted behavior requires the overall shift of all materials toward a more hard and compliant response. This blanket requirement does not equally fit possible patterns of structural or residual stress gradients that can be visualized from the pyrolysis process. Thus a clearer interpretation of these deviations needs further investigation.

5.5. Conclusions

The elastic and plastic deformation behavior of precursor derived Si-C-N ceramics was investigated using depth sensing nanoindentation. The elastic moduli and nanoindentation hardness evaluated from the analysis of load-displacement curves correlated well with the evolution of material resistance to elastic and plastic deformation, commensurate with the structural and microstructural evolution in the materials. Analysis of the work of indentation

during the load-unload cycle highlighted the characteristics of anomalous plastic deformation in the electron-amorphous Si-C-N materials. The consequence of the densifying type of plastic deformation in promoting strain hardening behavior in these materials was identified from the load dependant increase in hardness, to a measurable extent in the nanoindentation load regime and to an appreciable extent in the microindentation load regime. A semi-quantitative understanding of the yielding and strain hardening behavior of the materials was realized using reverse analysis of nanoindentation $P-h$ curves. The present results suggest that the magnitude of strain hardening is controlled both by the applied load and strain rate. The capacity of the phase separated materials for strain hardening was relatively lower than the amorphous materials. The pile-up and sink-in behavior was in agreement with the strain hardening capability of the materials. Also, the presence or absence of ISE in ceramic materials including PDC and silicate glasses seems to be determined by the relative dominance of the two competing factors: indentation creep and capability for strain hardening. The variations in the strain rate sensitivity of the present Si-C-N materials were in agreement with the cluster model of material flow.

6. Summary and conclusions

This thesis deals with the investigation of deformation and fracture mechanical properties of precursor derived ceramics (PDC) in the Si-C-N system. The materials were synthesized by thermal crosslinking and controlled thermolysis of a liquid poly(ureamethylvinyl)silazane precursor polymer. An important prerequisite for the mechanical characterization experiments was the fabrication of fully dense defect-free PDC test specimens with sufficient size. The factors critically affecting the successful fabrication of test specimens were: (a) bubble formation during crosslinking (b) internal gas pressure induced stress leading to bloating and cracking and (c) stresses from differential precursor-to-ceramic transformation due to thermal gradients across the sample bulk. These problems were addressed in two folds. Firstly, the formation of bubbles was eliminated using a special casting process, where the liquid precursor was crosslinked in hydrostatic confinement in PTFE molds. Secondly, by limiting the green body thickness to 1 mm and by moderating the conductive heat transfer to the sample during thermolysis through a proper choice of the heat transfer media, the pyrolytic stresses were minimized to produce defect-free dense ceramic bodies. Any remnant stresses were further relaxed during subsequent mechanical preparation of the specimens, *viz.*, cutting, grinding and polishing.

In order to develop an understanding of the influence of material structure on the mechanical behavior, the investigations were performed on a range of Si-C-N-(H) PDC, obtained at progressively increasing degree of polymer-to-ceramic transformation by increasing the final pyrolysis temperature. The range of selected thermolysis treatments enabled the synthesis of ceramic specimens covering material structures from partly organic amorphous to inorganic nano-crystalline states. For the purpose of understanding the structural evolution and the related mechanical behavior, these materials can be grossly divided into two groups as (a) amorphous materials and (b) phase-separated materials. Structural variation in the amorphous specimens was realized through the

progressive stripping of hydrogen with increasing thermal treatment, leading to materials with progressively increasing network connectivity. The presence of hydrogen in the amorphous materials can be visualized as disruptions in the otherwise continuous Si-C-N network, rendering the whole Si-C-N-H bulk as an assemblage of isolated regions of Si-C-N network. The elimination of hydrogen also ensued phase segregation at still higher thermolysis treatments, via the organization of the excess free carbon into a turbostratic graphite phase at 1200°C and the nucleation of nano-crystalline SiC at 1300°C thermolysis treatment. The latter phases again disrupt the continuous amorphous Si-C-N network. The preliminary evaluation of the physical and mechanical properties *viz.*, density and thermal conductivity elastic modulus and hardness correlated well with the above structural evolution.

The crack-tip toughness (K_{I0}) of the above range of Si-C-N materials was evaluated using the novel crack opening displacement (COD) method. The method proved to be well suited for the characterization of the present materials, considering the limitations of sample size. The use of fully dense defect-free specimens as obtained above ensured that the estimated values of K_{I0} were intrinsic to the respective materials. The reliability of the K_{I0} estimates was ascertained by the agreement of values evaluated from 'long cracks' realized from fixture loading and radial cracks from Vickers indentation. The estimated K_{I0} values ranged from 0.6 to 1.2 MPa m^{1/2} depending upon the structure of the materials that varied from partly organic amorphous to inorganic nanocrystalline states. The increase in the resistance to fracture in amorphous materials can be interpreted to directly result from the increased network connectivity realized through the progressive stripping of the one-fold coordinated (OFC) hydrogen. The latter structural change also led to an increase in the nano-scale crack deflection in these materials. On the other hand, low energy fracture paths provided by TG phase segregation controlled the micromechanics of crack propagation in phase separated materials. The prominent drop in the K_{I0} value of the SiCN-120012 material highlights the dominance of the effect of reduced

fracture surface energy over the toughening effect of crack deflection. The net change in crack resistance in these materials was effected by the change in the average fracture surface energy as well as crack deflection toughening. While it is clear that the organization and growth of the TG phase significantly influenced the crack propagation and thereby the evolution of fracture resistance in the phase separated materials, direct fractographic evidence to this effect could not be recorded using material contrast imaging using AFM. While the reasons for the lack of contrast is not clear at this moment, it is realized that the adherent moisture on the surfaces can induce potential artifacts in phase contrast imaging and can lead to misleading interpretations. It is proposed that an UHV-AFM analysis of the relevant fracture surfaces would be more illuminating in this regard.

In order to examine possible correlations of the geometrical contributions to toughening on the estimated K_{I0} values, and to probe the damage mechanisms operative at the propagating crack tip that manifest on the crack face morphology, roughness analysis of fracture surfaces were carried out using RMS roughness (R_q) and second order height-height correlation functions using the fractal approach. The evolution of R_q was well correlated with the evolution of sub-nanoscale structural and compositional inhomogeneities in the amorphous materials and formation of second phases in the phase segregated materials, leading to crack deflection. Fractal analysis of the fracture surface roughness revealed self-affine scaling up to a correlation length of around 50 nm and a self-affine roughness exponent (ζ) of 0.8 ± 0.1 in all the materials, the latter in agreement with the universal roughness exponent conjectured by Bouchaud *et al.* However, no correlation was observed between the observed roughness exponents and the fracture toughness of the corresponding materials. This result suggests that any manifestation of the variations in K_{I0} on the values of D or ζ is only marginal if any, at least in the presently investigated materials. However, the observation that the fractal correlation lengths of the present Si-C-N materials are of the same order of magnitude to that of silicate glasses indicates that the fractal

analysis reasonably captures the length scales of the damage (or process) zones in the respective materials. Examination of the crack opening near the crack tip revealed no persistent damage cavities along the crack, concluding that the fracture in the investigated Si-C-N ceramics proceeded in a brittle manner in the resolvable length scales, at crack velocities employed in the experiments. Digressing towards a general understanding of the fracture mechanisms in amorphous materials, the present observations and the similar investigations on silicate glasses suggest that a better experimental verification of the formation of persistent damage cavities requires investigations using materials of lower elastic modulus and higher crack-tip toughness (together leading to higher crack openings, thus enabling better resolution of possible cavities), along with lower crack velocities. Further, fractography of nanostructured materials towards the above ends leaves much more to be desired in terms of the resolution capabilities of the imaging techniques.

The elastic and plastic deformation behavior of the present Si-C-N ceramics under contact loading conditions was investigated using blunt (spherical) as well as sharp (Vickers and Berkovich) indentation experiments. The elastic moduli and nanoindentation hardness evaluated from the analysis of the nanoindentation load-displacement curves correlated well with the evolution of material resistance to elastic and plastic deformation, commensurate with the structural and microstructural evolution in the materials. Specifically, the elastic deformation behavior was directly correlated with the overall rigidity of the material structure, which was determined by the level of network connectivity and structural density of the materials. Analysis of the elastic and plastic deformation work quantities derived from the load-unload cycle of Berkovich nanoindentation enabled the discrimination of the different plastic deformation characteristics of the amorphous and phase segregated materials. The equi-proportional change in the work of elastic and plastic deformation in the amorphous materials revealed their anomalous character of plastic deformation that proceeded by densification. The contrasting evolution of deformation work in the phase separated materials

indicated the emergence of an additional mode of plastic deformation, promoted by the shear deformation of TG phase. The effect of the above two different mechanisms controlled the evolution of material resistance to plastic deformation at increasing stress in the respective materials. The densifying mode of plastic deformation in the amorphous materials led to strain hardening. This is manifested in the load dependant increase in hardness, which is observed to a measurable extent in the nanoindentation load regime and to an appreciable extent in the microindentation load regime. Although the estimates of plastic deformation parameters from the nanoindentation reverse analyses provided a semi-quantitative understanding of the yielding and strain hardening behavior of the materials, they do not completely quantify the real material behavior, which lies somewhere in between the two estimates presented. The present results suggest that the magnitude of strain hardening is controlled both by the applied load and strain rate. The capacity of the phase separated materials for strain hardening was relatively lower than the amorphous materials, evidently due to the additional shear deformation promoted by the TG phase. The two modes of plastic deformation also influenced the indentation size effect (ISE). The presence or absence of ISE in ceramic materials including PDC and silicate glasses seems to be determined by the relative dominance of the two competing factors: indentation creep and capability for strain hardening. The variations in the strain rate sensitivity of the present Si-C-N materials were in agreement with the cluster model of material flow. The contrasting influence of applied load on the strain rate sensitivity of amorphous and phase-separated materials again highlight the different operative deformation mechanisms in the respective materials.

While maximum efforts were exercised in minimizing the presence of residual stresses in the PDC test specimens, the possibility of any remnant residual stresses in quantitatively modifying the above results cannot be completely excluded. The evaluation of the magnitude and distribution of transformation-induced residual stresses in bulk PDC is an involving task in itself and offers

scope for future study. One possible effect of residual stresses on the present investigations is for example reflected in the significant deviations of the elastic moduli estimates from the non-destructive resonance frequency testing and nanoindentation analysis. However, it is noted that the former estimates were derived from relatively large test specimens, and hence the magnitude of attendant residual stresses can be expected to be larger. The span of test specimens used for crack-tip toughness estimation were smaller by a factor of roughly three, leading to a corresponding decrease in the residual stresses by elastic relaxation. Additionally, the good agreement between the K_{I0} estimates from 'long cracks' and Vickers indentation cracks indicates that these estimates were not measurably influenced by any remnant residual stresses. As the nanoindentation experiments were confined to an even smaller volume, the effect of residual stresses can be expected to be further negligible, especially on the qualitative evolution of contact deformation behavior across the range of investigated materials.

Finally, it should be noted that the exact values of the presently estimated mechanical properties of (particularly amorphous) Si-C-N materials are dependent on the PDC material structure and chemical constitution, and thus will be modified significantly depending on the chemistry of the starting precursor and processing conditions, e.g., heating rate, hold time etc. The variations due to the latter effect can be understood akin to the property variations in glasses with the change in fictive temperature. However, the structure of amorphous PDC is not bi-directionally variable by thermal treatment in a manner similar to glasses, as they do not exhibit a glass transition temperature. However, it is yet to be verified whether part or whole of the densification deformation during sharp indentation will be recoverable by thermal annealing, which is in fact observed in silicate glasses. This is also an interesting aspect for future investigations.

References

- [58lrw] G. R. Irwin, *Handbuch der Physik*. Vol. **6**. Springer–Verlag, Berlin, Germany, (1958).
- [64Mar] D.M. Marsh, *Proc. R. Soc. London. Ser. A.* **279**, 420 (1964).
- [68Nee] J. E. Neely and J.D. Mackenzie, *J. Mater. Sci.* **3**, 603 (1968).
- [70Tui] F. Tuinstra, J. L. Koenig, *J. Chem. Phys.* **53[3]**, 1126 (1970).
- [72Ric] J. R. Rice, *Int. J. Solids Struct.* **8**, 751 (1972).
- [78Yaj] S. Yajima, X. Hasegawa, J. Hayashi, M. Iiuma, *J. Mater. Sci.* **13**, 2569 (1978).
- [79Aro] A. Arora, D.B. Marshall and B.R. Lawn, *J. Non-Cryst. Solids.* **31**, 415 (1979).
- [79Nem] R. J. Nemanich, S. A. Solin, *Phys. Rev. B.* **20[2]**, 392 (1979).
- [81Wad] N. Wada, S. A. Solin, J. Wong, and S. Prochazka, *J. Non-Cryst. Solids.* **43**, 7 (1981).
- [83Fab] K. T. Faber and A. G. Evans, *Acta Metall.* **31[4]**, 565 (1983).
- [84Man] B. B. Mandelbrot, D. E. Passoja, A. J. Paullay, *Nature.* **308**, 721 (1984).
- [86Doe] M. F. Doerner and W. D. Nix, *J. Mater. Res.* **1**, 601 (1986).
- [86Sak] S. Sakka, *Ann. Rev. Mater. Sci.*, **16**, 29 (1986).
- [87ASM] *ASM handbook*, Vol. **12**, ASM International, Materials Park, Ohio, USA (1987)
- [87Kay] D. M. Kalyon and S. Kovenklioglu, *Adv. Polym. Tech.* **7[2]**, 191, (1987).
- [87Leg] G.E. Legrow, T.F. Lim, J. Lipowitz, R.S. Reaach, *Am. Ceram. Soc. Bull.* **66**, 363 (1987).
- [88Cha] R. Chaim, A.H. Heuer, *J. Am. Ceram. Soc.* **71**, 960 (1988).
- [89Mec] J.J. Mecholsky, D.E. Passoja, K.S. Feinberg-Ringel, *J. Am. Ceram. Soc.* **71**, 60 (1989).
- [90Dux] P.M. Duxbury in, H.J. Herman, S. Roux (eds.). p. 189 (1990).

- [90Han] W. -T. Han and M. Tomozawa, *J. Am. Ceram. Soc.* **73**, 3626 (1990).
- [90Röd] J. Rödel, J. F. Kelly, B. Lawn, *J. Am. Ceram. Soc.* **73**[11], 3313 (1990).
- [90Wan] Y. wang, D. C. Alsmeyer, R. L. McCreery, *Chem. Mater.* **2**, 557 (1990).
- [90Yao] H. Yao, S. Kovenklioglu, D.M. Kalyon, *Chem. Eng. Communications.* **96**, 155, (1990).
- [91Fet] T.Fett, *Eng. Fract. Mech.* **40**, 683 (1991).
- [92Oli] W.C. Oliver and G.M. Pharr, *J. Mater. Res.* **7**, 1564 (1992).
- [92Röd] J. Rödel, *J. Eur. Ceram. Soc.* **10**, 143, (1992).
- [93Keu] N. M. Keulen, *J. Am. Ceram. Soc.* **76**, 904 (1993).
- [93Law] B. R. Lawn, *Fracture of Brittle Solids*, Cambridge University Press, Cambridge, U.K. (1993).
- [93Pez] G. Pezzotti, *Acta Metall. Mater.* **41**[6], 1825 (1993).
- [94Bou] E. Bouchaud, J. P. Bouchaud, *Phys. Rev. B.*, **50**, 17752 (1994).
- [94Mil] V.Y. Milman, N.A. Stelmashenko, R. Blumenfeld, *Prog. Mat. Sci.* **38**, 425 (1994).
- [95Bil] J. Bill and F. Aldinger, *Adv. Mater.* **7**, 775 (1995).
- [95Gon] M. F. Gonon, G. Fantozzi, M. Murat, and J. P. Disson, *J. Eur. Ceram. Soc.* **15**, 591 (1995).
- [95Hei] D. Heimann, J. Bill, F. Aldinger, P. Schanz, F. Gern, W. Krenkel, R. Kochendoerfer, *Zeitschrift fuer Flugwissenschaften und Weltraumforschung.* **19**[3], 180 (1995).
- [95Sch] J. Schmittbuhl, J.P. Vilotte, *Phys. Rev. E.* **51**, 131 (1995).
- [96Boo] P. Boolchand, M. Zhang and B. Goodman, *Phys. Rev. B.* **53**, 11 488 (1996).
- [96Fre] H. Freimuth, V. Hessel, H. Kölle, M. Lacher, W. Ehrfeld, T. Vaahs, M. Brück, *J. Am. Ceram. Soc.* **79**, 1457 (1996).
- [96Gök] M. Göken, H. Vehoff, P. Neumann, *J. Vac. Sci. Technol. B.* **14**, 1157 (1996).

- [96Mal] H. Maleki, L. R. Holland, G. M. Jenkins, R. L. Zimmerman and W. Porter, *J. Mater. Res.* **11**[9], 2368 (1996).
- [96Mon] M. Monthieux and O. Delverdier, *J. Eur. Ceram. Soc.* **16**, 721 (1996).
- [96Sei] J. Seitz, J. Bill, *J. Mater. Sci. Lett.* **15**, 391, (1996).
- [96Sor] G.D. Soraru, E. Dallapiccola and G. D'Andrea, *J. Am. Ceram. Soc.* **79**, 2074 (1996).
- [96Suz] K. Suzuya, M. Furusaka, N. Watanabe, M. Osawa, K. Okamura, K. Shibata, T. Kamiyama, K. Suzuki, *J. Mater. Res.* **11**, 1169 (1996).
- [96Tab] D. Tabor, *Phil. Mag. A.* **74**, 1207 (1996).
- [97Ans] L. Anselm and G.H. Frischat, *J. Non Cryst. Solids.* **213 & 214**, 375 (1997).
- [97Bor] F. M. Borodich, *J. Mech. Phys. Solids.* **45**, 239 (1997).
- [97Bou] E. Bouchaud, *J. Phys. Condens. Matter.* **9**, 4319 (1997).
- [97Bur] N. A. Burham et al, *Nanotechnology*, **8**, 67 (1997).
- [97Dag] P. Dagquier, B. Nghiem, E. Bouchaud, F. Creuzet, *Phys. Rev. Lett.* **78**, 1062 (1997).
- [97Fan] S. J. Fang, S. Haplepete, W. Chen, C. R. Helms and H. Edwards, *J. Appl. Phys.* **82**[12], 5891 (1997).
- [97Kai] R. K. Kalia, A. Nakano, A. Omeltchenko, K. Tsuruta, P. Vashishta, *Phys. Rev. Lett.* **78**, 2144 (1997).
- [97Kie] J. D. Kiely, D. A. Bonnell, *J. Vac. Sci. Technol. B.* **15**, 1483 (1997).
- [97Räd] E. Rädlein, G. H. Frischat, *J. Non Cryst. Solids*, **222**, 69 (1997).
- [97Sei] J. Seidel and J. Rödel, *J. Am. Ceram. Soc.* **80**[2], 433 (1997).
- [98Che] Y-T. Cheng and C-M. Cheng, *J. Mater. Res.* **13**, 1059 (1998).
- [98Gal] D. Galusek, S. Reschke, C. Konetschny, R. Riedel, *Sil. Ind.* **63**[9-10], 123 (1998).
- [98Gar] R. Garcia, J. Tamayo, M. Calleja and F. Garcia, *App. Phys. A*, **8**, **66**, S309 (1998).

- [98Gra] P. Grau, G. Berg, H. Meinhard and S. Mosch, *J. Am. Ceram. Soc.* **81**, 1557 (1998).
- [98Kin] T. Kinoshita, *Acta mater.* **46**, 3963 (1998).
- [98Nis] T. Nishimura, R. Haug, J. Bill, G. Thurn, F. Aldinger, *J Mater Sci.* **33**, 5237 (1998).
- [98Sch] S. Schempp, J. Dürr, P. Lamparter, J. Bill, F. Aldinger, Z. Naturforsch, A, *Phys. Sci.* **53**, 127 (1998).
- [99Bal] H. P. Baldus, M. Jansen, D. Sporn, *Science*, **285**, 699 (1999).
- [99Bau] B. Baufeld, H. Gu, J. Bill, F. Wakai, F. Aldinger, *J. Eur. Ceram. Soc.* **19**, 2797 (1999).
- [99Cam] T. Campbell, R. K. Kalia, A. Nakano, F. Shimojo, K. Tsuruta, P. Vashishta, S. Ogata, *Phys. Rev.Lett.* **82**, 4018, (1999).
- [99Dus] J. Dusza and M. Steen, *Intl. Mater. Rev.* **44[5]**, 165 (1999).
- [99Gia] A. E. Giannakopoulos and S. Suresh, *Scripta Mater.* **40**, 1191 (1999).
- [99Kna] J. A. Knapp, D. M. Follstaedt, S. M. Myers, J. C. Barbour and T. A. Friedmann, *J Appl. phys.* **85**, 1460 (1999).
- [99Kon] C. Konetschny, D. Galusek, S. Reschke, C. Fasel, R. Riedel, J. *Europ. Ceram. Soc.* **19**, 2789 (1999).
- [99Van] L. Van Brutzel, PhD thesis, *Paris VI University* (1999)
- [99Wün] C. Wünsche, E. Rädlein, G. H. Frischat, *Glass Sci. Technol.* **72[2]**, 49 (1999).
- [00Dus] J. Dusza, *Int. J. Mater. Prod. Technol.* **15[3-5]**, 292 (2000).
- [00Fer] A.C. Ferrari, J. Robertson, *Phys. Rev. B.* **61[20]**, 14095 (2000).
- [00Gup] P. K. Gupta, D. Inniss, C. R. Kurkjian, Q. Zhong, *J. Non Cryst. Solids.* **262**, 200 (2000).
- [00Hen] S. Hénaux, F. Creuzet, *J. Am. Ceram. Soc.* **83**, 415 (2000).
- [00Hin] M. Hinojosa, L. Chávez, *Glass researcher.* **9**, 23 (2000).
- [00Kro] E. Kroke et al, *Mat. Sci. & Engg. (R).* **26**, 97 (2000).
- [00Li] Y. Li, R. Riedel, J. Steiger and H. V. Seggern, *Adv. Engg. Mater.* **2[5]**, 290 (2000).

- [00Mor] S. Morel, J. Schmittbuhl, E. Bouchaud and G. Valentin, *Phys. Rev. Lett.* **85**[8], 1678 (2000)
- [00Mot] G. Motz, J. Hacker, G. Ziegler, *Ceramic Engineering & Science Proc.* **21**[4], 307 (2000)
- [00Rey] E. Reyes, C. Guerrero, V. González, M. Hinojosa, *MRS Symp. Proc.* **578**, 357 (2000).
- [00Tan] D. Tanaka, S. Ohshio and H. Saitoh, *Jpn. J. Appl. Phys.* **39**, 6008 (2000).
- [00Wan] J. Wan, M.J. Gasch, A. K. Mukherjee, *J. Mat. Sci.* **15**[8], 1657 (2000).
- [01Bau] A. Bauer, M. Christ, A. Zimmermann, F. Aldinger, *J. Am. Ceram. Soc.* **84**[10], 2203 (2001).
- [01Chu] Chudoba and F. Richter, *Surf. Coat. Technol.* **148**, 191 (2001).
- [01Fer] A.C. Ferrari, J. Robertson, *Phys. Rev. B.* **64**[7], 075414 (2001).
- [01Gal] D. Galusek, F. L. Riley and R. Riedel, *J. Am. Ceram. Soc.* **84**, 1164 (2001).
- [01Gal] D. Galusek, F. L. Riley, R. Riedel, *J Am. Ceram. Soc.* **84**[5], 1164 (2001).
- [01Her] E.G. Herbert, G.M. Pharr , W.C. Oliver , B.N. Lucas and J.L. Hay, *Thin Solid Films.* **398–399**, 331 (2001).
- [01Iwa] N. Iwashita, M. V. Swain, J. S. Field, N. Ohta and S. Bitoh, *Carbon.* **39**, 1525 (2001).
- [01Jam] P. J. James et al, *Langmuir*, **17**, 349 (2001).
- [01Li] Y. Li, E. Kroke, R. Riedel, C. Fasel, C. Gervais and F. Babonneau, *App. Organometall. Chem.* **15**, 820 (2001).
- [01Lew] C.A. Lewinsohn, P. Colombo, Ö. Ünal, *J. Am. Ceram. Soc.* 2001, **84**[10], 2240 (2001).
- [01Lie] L. Liew, W. Zhang, V. M. Bright, L. An, M. L. Dunn, and R. Raj, *Sensors and Actuators*, **89**, 64 (2001).
- [01Ohk] Y. Ohkawara, S. Ohshio, T. Suzuki, H. Ito, K. Yatsui and H. Saitoh, *Jpn. J. Appl. Phys.* **40**, 7007 (2001).

- [01Rou] T. Rouxel, J-C. Sangleboeuf, J-P. Guin, V. Keryvin and G.D. Soraru, *J. Am. Ceram. Soc.* **84**, 2220 (2001).
- [01Tur] C. Turquat, H. J. Kleebe, G. Gregori, S. Walter and G. D. Soraru, *J. Am. Ceram. Soc.* **84**[10], 2189 (2001).
- [01Wan] J. Wan, M.J. Gasch, A. K. Mukherjee, *J. Am. Ceram. Soc.* **84**[10], 2165 (2001).
- [01Zen] K. Zeng and C-H. Chiu, *Acta Mater.* **49**, 3539 (2001).
- [02Bau] A. Bauer, PhD thesis, *Universität Stuttgart* (2002)
- [02Fet] T. Fett, *Int. J. Frac.* **114**[4], 29 (2002).
- [02Hau] J. Haug, PhD thesis, *Universität Stuttgart* (2002)
- [02Hin] M. Hinojosa, J. Aldaco, *J. Mater. Res.* **17** 1276 (2002).
- [02Ish] S. Ishihara, H. Gu, J. Bill, F. Aldinger and F. Wakai *J. Amer. Ceram. Soc.* **85**[7], 1706 (2002).
- [02Jan] N. Janakiraman et al., *J. Am. Ceram. Soc.* **85**, 1807 (2002).
- [02Mec] J.J. Mecholsky, J. K. West, D.E. Passoja, *Phil. Mag. A.* **82** ,3163 (2002).
- [02Mot] G. Motz und G. Ziegler, *Key Eng. Mater.* **206-213**, 475 (2002).
- [02Xu] Z-H. Xu and D. Rowcliffe *Phil. Mag. A.* **82**, 1893 (2002).
- [02Sha] S. Shah and R. Raj, *Acta Mater.* **50**, 4093 (2002).
- [02Wag] S. Wagner, H. J. Seifert, F.Aldinger, *Mat. Manu. Proc.* **17**[5], 619 (2002).
- [02Wal] S. Walter, G.D. Soraru, H. Brequel and S. Enzo, *J. Eur. Ceram. Soc.* **22**, 2389 (2002).
- [03Att] M. T. Attaf, *Mater. Lett.* **57**, 4684 (2003).
- [03Bou] E. Bouchaud, *Surf. Rev. Lett.* **10**[5], 797 (2003).
- [03Cel] F. Célarié, S. Prades, D. Bonamy, A. Dickele, E. Bouchaud, C. Guillot, C. Marlière, *Appl. Surf. Sci.* **212-213**, 92 (2003)
- [03Cela] F. Célarié, S. Prades, D. Bonamy, L. Ferrero, E. Bouchaud, C. Guillot and C. Marlière, *Phys. Rev. Lett.* **90**, 075504 (2003).
- [03Kou] A. B. Kounga, T. Fett, D. C. Lupascu and J. Rödel, *J. Am. Ceram. Soc.*, 2003, **86** [11], (1973).

- [03Mor] K. V. Moraes and L. V. Interrante, *J. Am. Ceram. Soc.* **86**, 342 (2003).
- [03Pog] J. F.- Poggemann, G. Heide, G. H. Frischat, *J. Non Cryst. Solids.* **326 & 327**, 15 (2003).
- [03Tra] S. Trassl, M. Puchinger, E. Rössler and G. Ziegler, *J. Europ. Ceram. Soc.* **23**, 781 (2003).
- [04Bur] Z. Burghard, PhD thesis, *Universität Stuttgart* (2004).
- [04Bura] Z. Burghard, A. Zimmermann, J. Rödel, F. Aldinger, B. R. Lawn, *Acta Mater.* **52**, 293 (2004).
- [04Che] Y-T. Cheng and C-M. Cheng, *Mater. Sci. Eng.* **R 44**, 91 (2004).
- [04Gui] J. P. Guin and S. M. Wiederhorn, *Phys. Rev. Lett.* **92**, 215502 (2004).
- [04Kou] A. B. Kounga, T. Fett, J. Rödel, G. Quinn, *J. Am. Ceram. Soc.* **87[8]**, 1502 (2004).
- [04Lee] S. H. Lee, PhD thesis, *Universität Stuttgart*, 2004.
- [04Li] H. Li and A. H. W. Ngan, *J. Mater. Res.* **19**, 513 (2004).
- [04Oli] W. C. Oliver and G. M. Phaar, *J. Mater. Res.* **19**, 3 (2004).
- [05Fet] T. Fett, D. Munz, A. B. Kounga, J. Rödel, G. D. Quinn, *J. Eur. Ceram. Soc.* **25[1]**, 29 (2005).
- [05Gre] G. Gregori, H. -J. Kleebe, H. Brequel, S. Enzo and G. Ziegler, *J. Non Cryst. Solids*, **351**, 1393 (2005).
- [05Gui] J. P. Guin, S. M. Wiederhorn, T. Fett, *J. Am. Ceram. Soc.* **88**, 652 (2005).
- [05Kro] P. Kroll, *J. Non Cryst. Solids.* **351**, 1121 (2005).
- [05Kroa] P. Kroll, *J. Non Cryst. Solids.* **351**, 1127 (2005).
- [05Qia] L. Qian, M. Li, Z. Zhou, H. Yang and X. Shi, *Surf. Coat. Technol.* **195**, 264 (2005).
- [05Yos] S. Yoshida, J-C. Sanglebœuf and T. Rouxel, *J. Mater. Res.* **20**, 3404 (2005).
- [06Kat] Y. Katsuda, P. Gerstel, N. Janakiraman, J. Bill and F. Aldinger, *J. Am. Ceram. Soc.* **26**, 3399 (2006).

- [06Kla] D. Klaffke, R. Wasche, N. Janakiraman and F. Aldinger, *Wear.* **260**, 711 (2006).
- [06Moy] C. Moysan, R. Riedel, R. Harshe, T. Rouxel and F. Augereau, *J. Eur. Ceram. Soc.* in press. (2006).
- [06Per] A. Perriot, D. Vandembroucq, E. Barthel, V. Martinez, L. Grosvalet, Ch. Martinet and B. Champagnon, *J. Am. Ceram. Soc.* **89**, 596 (2006).
- [06Tan] M. Tan, *J. Mater. Res.* **21**, 1363 (2006).
- [06Zha] M. Zhao, X. Chen, J. Yan and A. M. Karlsson, *Acta Mater.* **54**, 2823 (2006).
- [07Jan] N. Janakiraman and F. Aldinger, *J. Eur. Ceram. Soc.* Submitted.
- [07Jana] N. Janakiraman Z. Burghard and F. Aldinger, *J. Non-Cryst. Solids.* Submitted.
- [07Janb] N. Janakiraman and F. Aldinger, *J. Non-cryst. Solids.* Submitted.

Zusammenfassung und Ausblick

In der vorliegenden Dissertation wird die Untersuchung der Verformung und der bruchmechanischen Eigenschaften von Si-C-N-Precursorkeramiken (precursor-derived ceramics, PDC) beschrieben. Die Materialien wurden durch thermische Vernetzung und temperaturkontrollierte Thermolyse eines flüssigen Poly(ureamethylvinyl)silazan-Precursorpolymers synthetisiert. Die Hauptziele der vorliegenden Arbeit waren (i) die intrinsischen mechanischen Eigenschaften der synthetisierten Si-C-N-Precursorkeramiken zu bestimmen und (ii) die mechanischen Eigenschaften dann mit der Struktur der Materialien, die bei der mehrstufigen Phasenbildung während der Precursor-zu-Keramik Umwandlung entsteht, zu korrelieren.

Bis jetzt erfolgte die mechanische Charakterisierung derartiger Materialien hauptsächlich an Proben, die pulvertechnologisch hergestellt wurden. Dadurch wurden deren Eigenschaften stark durch die extrinsischen Gefügemerkmale, wie z.B. die Porosität, beeinflusst. Die Herstellung völlig dichter Proben war deshalb eine wichtige Voraussetzung für die Bestimmung ihrer intrinsischen mechanischen Eigenschaften. Folgende Faktoren beeinflussen die erfolgreiche Herstellung eines völlig dichten Probenmaterials negativ: (a) Blasenbildung während der Vernetzung, (b) Entstehung eines inneren Gasdrucks, weil die bei der Pyrolyse sich bildenden gasförmigen Nebenprodukte nicht entweichen können und (c) Spannungen, die durch die differentielle Precursor-zu-Keramik-Umwandlung aufgrund von auftretenden thermischen Gradienten im vernetzten Grünkörper verursacht werden. Diese Probleme ließen sich wie folgt beseitigen: (a) Vermeidung der Entstehung von Blasen durch Anwendung eines speziellen Prozesses, bei dem der flüssige Precursor in PTFE-Formen gegossen und vernetzt wurde, wobei sich beim Aufheizen ein hydrostatischer Druck aufbaute und (b) Verminderung von Spannungen, die bei der Pyrolyse auftraten, sowohl durch Begrenzung der Grünkörperdicke auf 1 mm als auch durch Verlangsamung der Wärmeübertragung auf die Probe während der Thermolyse

durch die Wahl geeigneter Wärmeübertragungsmittel. Damit ließen sich völlig dichte defektfreie keramische Proben herstellen. Resteigenspannungen im Material wurden während der nachfolgenden mechanischen Bearbeitung wie Schneiden, Schleifen und Polieren abgebaut.

Um den Einfluss der Materialstruktur auf das mechanische Verhalten der Keramiken zu bewerten, wurden die Untersuchungen an einer Auswahl von Precursormaterialien mit stufenweise zunehmendem Grad der Precursor-zu-Keramik-Umwandlung, was durch eine Erhöhung der Pyrolysetemperatur erreicht wurde, durchgeführt. Die ausgewählten Thermolysebedingungen ermöglichten die Synthese von keramischen Materialien mit Strukturen, die einen fließenden Übergang vom organisch amorphen bis zum anorganisch nano-kristallinen Zustand umfassen. Um die strukturelle Entwicklung in Verbindung mit dem mechanischen Verhalten der Keramiken zu verstehen, wurden diese Probenmaterialien in zwei Gruppen eingeteilt: (a) amorphe Materialien und (b) phasenetrennte Materialien. Strukturelle Veränderungen der amorphen Probenmaterialien wurden durch die fortschreitende Entfernung des Wasserstoffs im Verlauf der Thermolyse und die damit einhergehende kontinuierliche Zunahme der Vernetzung (Strukturverdichtung) festgestellt. Die Anwesenheit von Wasserstoff in den amorphen Materialien führte zu einem Aufbrechen des Si-C-N-Netzwerks. Die Unterbrechungen können als Inhomogenitäten in der lokalen Struktur und/oder der lokalen Zusammensetzung des amorphen Si-C-N-Netzwerkes aufgefasst werden. Die Beseitigung des Wasserstoffs führte bei 1200°C zu einer Phasenausscheidung durch Überführung des überschüssigen freien Kohlenstoffs in eine turbostratische Graphitphase (TG-Phase) und bei 1300°C zur Keimbildung von nano-kristallinem SiC (n-SiC). Die Bildung dieser Phasen führt zu Inhomogenitäten in der amorphen Si-C-N Matrixphase. Die Auswertung der physikalischen und mechanischen Eigenschaften (Dichte, Elastizitätsmodul, Härte und Wärmeleitfähigkeit) ergab, dass diese gut mit den oben genannten strukturellen Merkmalen korrelieren.

Für die bruchmechanische Charakterisierung diente als Bewertungskriterium die Bruchzähigkeit an der Rissspitze („crack-tip toughness“, kritischer Spannungsintensitätsfaktor an der Rissspitze, K_{I0}), wozu eine neu entwickelte Rissöffnungsprofil-Methode (crack-opening displacement, COD) eingesetzt wurde. Diese Methode erwies sich unter Berücksichtigung der Begrenzung durch die Probengröße als gut geeignet für die Charakterisierung der genannten Si-C-N Materialien. Bei der Untersuchung von völlig dichten defektfreien Proben wurde eine Übereinstimmung der ermittelten intrinsischen Werte von K_{I0} mit den für die entsprechenden Keramiken an gekerbten Proben ermittelten Bruchzähigkeitswerten festgestellt. Die Übereinstimmung der Langrissmessungen (Rissbildung an gekerbten, rechteckigen Proben, Belastung in einer mechanischen Belastungsvorrichtung) mit den durch Vickers-Eindrücke erzeugten radialen Rissen, zeigt die Zuverlässigkeit der K_{I0} -Untersuchungen. In Abhängigkeit vom Umwandlungsgrad der Materialien wurden K_{I0} -Werte von 0.6 bis 1,2 MPam^{1/2} ermittelt. Die Zunahme des Bruchwiderstandes der amorphen Materialien kann auf die zunehmende Vernetzung durch die kontinuierliche Entfernung des Wasserstoffs zurückgeführt werden. Durch die daraus resultierende Erhöhung des Vernetzungsgrades wurde auch die nanoskalige Rissablenkung in amorphen Materialien erhöht. Andererseits steuerten die Pfade mit niedrigerer Oberflächenenergie im Gefüge, die auf die Separierung der TG-Phase zurückzuführen sind, die Mikromechanik der Rissausbreitung in phasenetrennten Materialien. Die auffallende Verringerung des K_{I0} -Wertes einer Probe, die bei 1200°C pyrolysiert wurde und eine relativ geringe Rauigkeit der Bruchfläche aufwies, zeigte, dass der Einfluss der verringerten Bruchoberflächenenergie in diesem Material größer ist als der Einfluss der Rissablenkung. Dieses Verhalten ist in einem bei 1300°C pyrolysierten Material umgekehrt, in dem eine gut entwickelte TG-Phase und die SiC Ausscheidungen eine Steigerung der Materialzähigkeit durch eine ausgeprägte Rissablenkung fördern, was die Verminderung der Bruchoberflächenenergie überkompensiert. Die Netto-Änderung des Bruchwiderstandes in diesen Materialien erfolgte sowohl

durch die Änderung der durchschnittlichen Bruchoberflächenenergie als auch durch eine Zunahme der Rissablenkung. Der Einfluss der TG-Phase auf die Rissausbreitung und dadurch auf den Bruchwiderstand spiegelt sich also offenbar in den Bruchzähigkeitswerten wider. Ein direkter fraktographischer Nachweis für diesen Effekt durch Rasterkraftmikroskopie-Untersuchungen (AFM) mit Materialkontrastabbildung konnte jedoch nicht erbracht werden. Die Gründe für den Mangel an Kontrast konnten bis jetzt nicht ermittelt werden. Es ist jedoch anzunehmen, dass Oberflächenfeuchtigkeit Artefakte bei der Materialkontrastabbildung verursachen, was zu falschen Interpretationen führen kann.

Um herauszufinden, ob es einen Zusammenhang zwischen dem Rissverlauf und einer Steigerung der Zähigkeit (K_{I0} -Werte) gibt und, um den Schädigungsmechanismus, der an der fortschreitenden Rissspitze stattfindet und sich an der Bruchflächenmorphologie bemerkbar macht, zu ermitteln, wurde die Rauigkeit der Bruchoberflächen analysiert. Die Entwicklung der Oberflächenrauigkeit R_q korrelierte mit dem Auftreten der sub-nanoskaligen Struktur, aufgrund der Bildung von Zweitphasen. Die Fraktalanalyse der Oberflächenrauigkeit ergab eine Korrelationslänge (fractal correlation length ξ) von ca. 50 nm und einen Rauigkeitsexponenten (ζ) von 0.8 ± 0.1 in allen Materialien. Dieser Wert stimmt mit dem Universalrauigkeitsexponent, der, nach Bouchaud *et al.* bei 0.8 liegt, überein. Es wurde jedoch keine Wechselwirkung zwischen den ermittelten Rauigkeitsexponenten und der Bruchzähigkeit der entsprechenden Materialien festgestellt. Die Ergebnisse lassen vermuten, dass jede mögliche Erscheinungsform einer Veränderung von K_{I0} in den hier untersuchten Materialien die Werte von D oder ζ , wenn überhaupt, dann nur marginal beeinflussen. Die Beobachtung, dass die fraktale Korrelationslänge der untersuchten Si-C-N Materialien von derselben Größenordnung ist wie diejenige in Silikatgläsern zeigt jedoch, dass die fraktographische Analyse die Längenskalen der beschädigten Zonen in den entsprechenden Materialien erfasst. Die Prüfung der Rissöffnung in der Nähe der Rissspitze ließ keine

Beschädigungskavitäten entlang des Bruches erkennen. Daraus ist zu schließen, dass der Bruch in den untersuchten Si-C-N-Keramiken soweit mit den gegebenen Abbildungstechniken erkennbar als reiner Sprödbruch verlief.

Das elastische und plastische Verformungsverhalten der untersuchten Si-C-N-Keramiken unter Kontaktbelastungsbedingungen wurde durch Kugeleindruck (stumpf) und Spitzeneindruck (Vickers und Berkovich) untersucht. Die Elastizitätsmodule und Härte, die sich aus der Nanoindentation-Last-Eindrucktiefe (load-displacement oder $P-h$)-Kurven ergaben, stimmten mit dem Materialwiderstand gegen die elastische und plastische Verformung der jeweiligen Materialien überein. Ganz spezifisch korreliert das elastische Verformungsverhalten mit der Brutto-Steifigkeit der Materialstruktur, die sich aus dem Vernetzungsgrad und der strukturellen Dichte der Materialien ergab. Die Werte der elastischen und plastischen Verformungsarbeit, die aus den Belastungs- und Entlastungszyklen der Berkovich-Indentationen ermittelt wurden, ermöglichten eine Unterscheidung der plastischen Verformungseigenschaften amorpher und phasengetrennter Materialien. Die equiproportionale Änderung der Eindrucksarbeit der elastischen und plastischen Verformung in amorphen Materialien zeigte den anomalen Charakter der plastischen Verformung, die bei der Materialverdichtung stattfand. Die entgegengesetzte Entwicklung der Verformungsarbeit in den phasengetrenten Materialien zeigte das Auftreten einer zusätzlichen Form von plastischer Verformung, die durch die Scherverformung der TG-Phase gefördert wurde. Der Effekt der beiden Verformungsmechanismen steuerte die Entwicklung des Materialwiderstandes gegen die plastische Verformung bei zunehmender Spannung in den jeweiligen Materialien. Der Materialverdichtungsmodus der plastischen Verformung führte in den amorphen Materialien zu einer Kaltverfestigung. Das wird in der belastungsabhängigen Zunahme der Härte ersichtlich, die in einem messbaren Umfang im Nanoindentation-Belastungsbereich und in einem beträchtlichen Umfang im Mikroindentation-Belastungsbereich beobachtet wird. Die Analyseverfahren, die

zur Ermittlung der Nanoindentationsdaten eingesetzt wurden, erlaubten eine halb-quantitative Bewertung des Fließ- und Verfestigungsverhaltens der Materialien. Daraus sind jedoch keine quantitativen Aussagen über das wirkliche Materialverhalten abzuleiten, das letztlich aber zwischen den zwei angegebenen Kennwerten liegt. Die erhaltenen Ergebnisse lassen vermuten, dass die Größe der Kaltverfestigung sowohl von der angewandten Belastung als auch von der Belastungsrate abhängt. Die Kapazität der phasengetrenten Materialien für die Verfestigung war niedriger als bei den amorphen Materialien, offenbar wegen der zusätzlichen Scherdeformation, die durch die TG-Phase gefördert wurde. Die beiden Modi der plastischen Verformung beeinflussten auch die Lastabhängigkeit der Härte (indentation size effect, ISE). Das Ausmaß der Lastabhängigkeit der Härte in keramischen Materialien, einschließlich PDC und Silikatgläsern, scheint durch die relative Dominanz der zwei konkurrierenden Faktoren Eindruck-Kriechverformung und Fähigkeit zur Kaltverfestigung bestimmt zu werden. Die Änderung der Dehnratenempfindlichkeit der untersuchten Si-C-N-Materialien stimmte mit dem sogenannten „cluster model“ des Materialflusses überein. Der entgegengesetzte Einfluss der angewandten Belastung auf die Dehnratenempfindlichkeit der amorphen und phasengetrenten Materialien verdeutlicht wiederum die unterschiedlich wirksamen Verformungsmechanismen in den jeweiligen Materialien.

Abschließend ist zu betonen, dass die genauen Kennwerte der in dieser Arbeit ermittelten mechanischen Eigenschaften und ganz besonders die der amorphen Si-C-N-Materialien stark von der PDC-Materialstruktur und der chemischen Zusammensetzung abhängen. Deshalb werden diese insbesondere von der Zusammensetzung des polymeren Ausgangsmaterials (Precursor) und von den Prozessparametern (z. B. Heizrate, Haltezeit etc.) beeinflusst. Die Veränderungen aufgrund des letztgenannten Effektes sind denen der mit der Übergangstemperatur verbundenen Eigenschaftsänderungen der Gläser sehr ähnlich. Die Strukturänderung der amorphen PDC-Materialien ist jedoch nicht reversibel, da diese keine Glasübergangstemperatur besitzen. Es ist jedoch noch

zu prüfen, ob durch Glühen eine teilweise oder gar vollständige Erholung der Verdichtungsverformung, die bei den Eindruckmethoden in amorphen Precursorkeramiken auftritt, möglich ist, was bei Silikatgläsern beobachtet wird, was ein interessanter Aspekt für zukünftige Untersuchungen ist.

Curriculum Vitae

Personal Information:

Name: Narayanan Janakiraman
 Date of birth: April 28, 1971
 Place of birth: Chennai, Tamilnadu, India
 Nationality: Indian
 Marital status: Married

Education:

1976-1986 High school, Chennai, India

1986-1989 Diploma in Mechanical Engineering, Central Polytechnic, Chennai, India

1993-1997 Bachelors degree in Metallurgy and Materials Science, Institution of Engineers(India), Calcutta, India

1998-2000 Master of Technology (M.Tech) in Metallurgical Engineering, Specialization: Materials technology, Indian Institute of Technology Madras, Chennai, India
 Masters thesis: Thermal stability and crystallization behavior of precursor derived covalent ceramics in the Si-B-C-N system
 Thesis work carried out at Max-Planck-Institut für Metallforschung, Stuttgart with financial support from DAAD

2000-2005 Ph.D. work at the Max-Planck-Institut für Metallforschung and Institute für Nichtmetallische Anorganische Materialien der Universität Stuttgart with support from Max-Planck-Gessellschaft.
 Ph.D. thesis: Deformation and fracture mechanical properties of precursor-derived Si-C-N ceramics.

Work experience:

1990-1995 Worked as 'Service Engineer' with Elecon Engineering Co. Limited, Gujarat, India. Area of work: Erection, commissioning, trouble shooting, servicing and failure analysis of worm and helical reduction gearboxes.

2000 2 months 'Industriepraktikum' at CeramTec AG, Marktredwitz, Germany. Theme of the work: Crystallization investigations on alumina - glass ceramic composite materials used in tape casting of electronic substrates.

since 2005 Guest researcher at the department of Inorganic Chemistry, Arrhenius Laboratory, Stockholm University, Sweden